IONIC LIQUID–BASED 3D PRINTED SOFT PRESSURE SENSORS AND THEIR APPLICATIONS

A Dissertation

Presented to

The Graduate Faculty of The University of Akron

In Partial Fulfillment

Of the Requirements for the Degree

Doctor of Philosophy

Md Omar Faruk Emon

August, 2020

IONIC LIQUID–BASED 3D PRINTED SOFT PRESSURE SENSORS AND THEIR APPLICATIONS

Md Omar Faruk Emon

Dissertation

Approved:	Accepted:
Advisor Dr. Jae-Won Choi	Department Chair Dr. Sergio Felicelli
Committee member Dr. Gregory Morscher	Dean of the College Dr. Craig Menzemer
Committee member Dr. Siamak Farhad	Interim Director, Graduate School Dr. Marnie Saunders
Committee member Dr. Kye-Shin Lee	Date
Committee member Dr. Thein Kyu	

ABSTRACT

Soft and stretchable electronics will play an important role in the areas of robotics, prosthetics, wearables, and energy harvesting devices. The emergence of smart technologies is spurring the development of a wider range of applications for stretchable and conformable pressure sensors. Concomitant with the material research on soft sensors, the fabrication method is also gaining major progress. The manufacturing and design flexibility offered by additive manufacturing (AM) may enable the fabrication of sensors that are superior to those fabricated by conventional manufacturing techniques. AM could realize applications of the sensors which are difficult to achieve via a conventional method.

In this work, a flexible and stretchable pressure sensor has been proposed. A pressure-sensitive membrane was fabricated through the polymerization of an ionic liquid (IL)-prepolymer blend. Stretchable conductive strips or electrodes were fabricated using a carbon nanotube (CNT)/polymer composite. The IL-based pressure-sensitive layer was sandwiched between CNT–based stretchable electrodes and encapsulated within stretchable top and bottom insulating layers.

The multi-layer multi-material sensor was first fabricated through a screen-printing and molding process for evaluation and characterization purposes. Sensor performance was investigated for different degrees of crosslinking and polymerization, concentrations of IL, and thicknesses of the IL/polymer layer. The experimental results showed that these variables affect the sensitivity of the sensor. Next, various forces were applied to a screen-printed sensor to determine the reliability, sensitivity, and dynamic range. The proposed

IL-based sensor displayed superior performance with high sensitivity and reliability. The sensor was also investigated for temperature dependence and shelf life. Different applications of the screen-printed sensor were explored such as sensor embedded tire and sensor embedded insole. While the sensors for these experiments were manufactured using screen printing and molding processes, the materials used for sensor fabrication are 3D printable, as 3D printing is the target manufacturing technique.

A multi-material 3D printing system with three extrusion heads was developed to fabricate the soft pressure sensor. The system employs an extrusion-based direct-print (DP) process. The capability of the system was demonstrated by printing structures made from three materials. The sensor materials were modified for the extrusion-based printing and printing parameters were identified for different materials of the sensor. Next, a flat sensor was 3D printed via a planar 3D printing technique. The 3D printed sensor was evaluated for different loading conditions. Finally, a sensor was conformally 3D printed on a free-form fingertip. The non-flat sensor model was conformally sliced to generate the curvilinear toolpath for conformal printing. Sensors fabricated via molding/screen-printing, planar 3D printing, and conformal 3D printing were compared for their responses. A 3D printed sensor application was explored by developing a grasping aid for neuropathy patients.

Introducing IL to fabricate a soft pressure sensor opens newer possibilities for research and applications in the area of stretchable electronics. AM provides a unique freedom for design customization. Soft sensor produced via AM is believed to usher numerous novel studies in the future.

ACKNOWLEDGMENTS

I could not have completed this study without the support of my mentors, peers, friends, and family members. I would like to express my gratitude to all who assisted me and supported me through this journey.

First of all, I cannot thank my advisor, Dr. Jae-Won Choi, enough for the support he provided for the last five and a half years. Dr. Choi was my mentor for all the difficulties and challenges that I had during this process. He guided and inspired me with patience through all the ups-and-downs of my doctoral research. He positively influenced my approach to scientific exploration in many ways. He was always there with not only his intellect but also the kindness to support me in my research and personal life. I am beholden to him for all his contribution in my life. It was a true honor to work with him.

I would also like to thank my doctoral committee members; Dr. Gregory Morscher, Dr. Siamak Farhad, Dr. Kye-Shin Lee, and Dr. Thein Kyu. I appreciate their guidance, support, and critical input in my work. Their advice encouraged me to explore more on my work.

I would like to acknowledge the members of the Advanced Additive Manufacturing Lab (AAML) at the University of Akron. I neither worked alone nor started from zero. I am grateful to my past and present lab-mates and colleagues for their intellectual contribution to my work.

I would also like to thank my parents and siblings for their endless love and support. Their sacrifice and guidance throughout my life brought me to where I am today. Finally, there are no words to describe the support of my wife Zafar Waziha Sarker in this journey. It would not have been possible without her assistance and backing.

TABLE OF CONTENTS

Page

LIST OF FIGURES

LIST OF TABLES

Table Page

CHAPTER I

INTRODUCTION

1.1 Background

Research and development in the area of flexible and stretchable electronics have significantly accelerated in the last decade. Synchronous progress in functional material research and fabrication method is bridging an important gap in science and technology. Recently, additive manufacturing of stretchable electronics is spurring major innovations in many areas such as robotics [1], prosthetics [2], [3], wearable electronics [4], [5], and energy harvesting devices [6]. In particular, three dimensional (3D) printing of soft pressure sensors is not only overcoming the limitations of conventional manufacturing methods but also opening avenues for newer applications.

Hard or rigid electronics comes short in integration and evaluation of systems where parts are moveable and subjected to bending and flexing [7], [8]. For example, the robotic hand shown in Figure 1.1, has 24 joints/movements and 20 degrees of freedom. To outfit this robotic hand with tactile sensors for gripping, soft stretchable sensors are needed, as they are conformable and can absorb some impact [9]. Next, 3D printing would provide scopes to fabricate any complex geometry following the free-form surfaces of the fingers where traditional manufacturing techniques could fail to realize the design complexity.

Figure 1.1. Shadow C6M dexterous hand (Shadow Robot Co., Inc., London, U.K.) [10].

Numerous studies on 3D printed stretchable pressure sensors have been conducted in the recent past [10]. Various elastomers are explored to develop soft tactile/pressure sensors. Additive manufacturing methods based on material extrusion [12], [13] and light projection [14] have been implemented for printing soft pressure sensors. With the increasing interest in 3D printed sensors, various newer applications are being suggested. New applications come with opportunities for research in material and fabrication process development. Moreover, there are opportunities to implement novel materials and fabrication processes to go beyond the limitations of existing works. This thesis reports the material development for soft pressure sensors, an additive manufacturing technique for fabrication, and applications of the printed sensors.

1.2 Ionic Liquid-Based Soft Sensor

Soft and stretchable sensors have potential applications in soft robotics and human-machine interfaces [1], [12], [15]. One common strategy to achieve stretchability in sensors is to use a stretchable polymer with conductive fillers. Carbon nanotube (CNT)–based piezoresistive sensors are among the more widely studied ones [13], [16]. In the past few years, various studies have been conducted on CNT-based stretchable pressure sensors to be utilized in the fields of robotics and prosthetics [2], [17]. Despite the significant progress in the development of CNT-based soft sensors, a number of problems remain to be explored, and there is room for improvement in terms of reliability and controllability [18], [19].

The recent introduction of ionic liquids (ILs) to the area of pressure sensors opened a new door to explore the stretchable sensors [20], [21]. ILs, which are composed of liquid salt at ambient temperature and contain ions, have highly sought-after characteristics such as high ionic conductivity, nonvolatility, nonflammability, and most importantly electrochemical stability [22], [23]. The ILs could be mixed with a prepolymer, and subsequently polymerized to create a piezoresistive film. A polymerized IL/polymer network shows strain-dependent resistive property. While ILs have been utilized to fabricate various devices for sensing, those that are in a liquid state have very limited applications [24], [25]. Some studies have been published on solid-state IL-based sensors, but they generally lack manufacturing and design flexibility [21], [26].

In this work, IL was incorporated into a prepolymer matrix to fabricate a solid-state pressure-sensitive film through polymerization to obtain an IL/polymer network with a high electrical resistance that changes under mechanical strain. This system was utilized as the sensing principle in the pressure sensor. The IL/polymer film was placed between a multi-walled carbon nanotube (MWCNT)-based stretchable conductive electrode to fabricate the stretchable pressure sensor. Incorporating ILs into the solid-state pressure sensor not only provides more reliability but also gives more control over the sensing performance.

1.3 3D Printing of Sensor

Along with research on functional materials, the fabrication process for soft sensors has garnered more attention in recent years. The various manufacturing techniques that have been suggested for fabricating soft sensors include injection molding [27], coating [28], the fill and lamination process [29], and screen printing [30]. Although these methods are appropriate for building sensors with simple geometries, they are unsuitable for fabricating sensors with complex geometries or for sensors on free-form surfaces. 3D printing overcomes the limitations of conventional manufacturing processes, offering design flexibility, customizability, and manufacturing scalability [31], [32]. In many cases, especially those where sensors are not required to be mass-produced, 3D printing reduces costs, as the printing of different designs does not involve changing the manufacturing setup for each product. Besides, 3D printing is preferred over traditional methods for the manufacturing of objects/parts that contain internal features or that need to be built using multiple materials. Moreover, for an application that employs tactile sensors on human-machine interfaces and for prosthetics or robotics, free-form surfaces are involved; 3D printing could be a possible solution for fabricating electronics on a free-form, non-flat substrate [33].

In this work, initially, a hybrid manufacturing process combining molding and screen printing was suggested to fabricate relatively simpler sensors for sensor characterization. Once sensing behavior was understood, 3D printing was employed as a manufacturing technique. A multi-material direct-print system has been developed. The system employs an extrusion-based direct printing method using a modified pre-polymer material. Since the sensor primarily consists of three different materials, the printing system was developed to handle three separate materials in a single print.

1.4 Applications

The 3D printed soft pressure sensor could be applied to a wide range of applications. The stretchability of the sensor enables it to employ in devices or parts that go through flexing, bending, and elastic deformation. The 3D printing process gives unparalleled manufacturing and design flexibility. Customization and design modification according to a specific application is possible through 3D printing. Moreover, it provides the scope to use a broad selection of materials. This work explores applications such as smart tires, smart insoles, and sensors on a finger with 3D printed and screen printed sensors.

Tires equipped with different sensors have always been an area of research interest and ongoing progress [34]. Now with the emergence of automation, applications like self-driving cars, mobile robots, and most importantly vehicle active safety systems expect tires to gather as much information as possible [35], [36]. Adverse road conditions and faulty tires are often responsible for traffic accidents [34]. Therefore sensors embedded in tires capable of monitoring real-time road conditions and tire health would be a step ahead in terms of automation and safety measures [37], [38]. Also in the development phase of a new tire, various conditions for tire testing need to be monitored and validated. A current method for developing new tires employs a pressure pad to measure tire mechanics including tire tread (footprint) pressures while the tire rolls through the pad [39]. This method does not provide a real driving experience and also limits dynamic testing. Dynamic testing with different conditions is a major step while developing a new tire [40]. Sensor embedded tires could improve the current tire testing system and provide opportunities for diverse testing conditions. The proposed sensor was embedded in a tire model and evaluated for different conditions.

Another application demonstrated was an insole with sensors. Foot plantar pressure distribution and timing provide vital information about athletic biomechanics which can be used to prevent injury as well as to enhance performance [41]–[43]. Facts obtained could also be valuable in footwear evaluation [44] and clinical gait analysis [45]. There are some indoor laboratory setting of platform-based foot plantar pressure measurement systems [42], which lack real walking/running experience. On the other hand the in-shoe systems can provide real-life conditions and widen the range of experiments [43], [46]. Present in-shoe plantar pressure measurement systems have limitations as they are generally expensive and uncomfortable; additionally, the sensors lack reliability and sensitivity [43], [47]. The discomfort and uneasiness of in-shoe systems come from the imperfect shape of insoles and rigidity of the sensor embedded in the insole. A smart insole with the proposed sensor was used to investigate different walking patterns.

A visual grasp aid for Diabetic Neuropathy patients was also developed using the proposed sensor where a 3D printed sensor was installed on a glove to provide real-time feedback of the grasping force. Diabetes is a disease characterized by high blood sugar (glucose) levels in the body over a prolonged period of time. There are mainly type 1, type 2, and prediabetes, where type 1 is the most severe and prediabetes is the least severe form. Globally, an estimated 422 million adults are living with diabetes, according to the 2016 data from the World Health Organization (WHO) [48]. In addition to high glucose levels, diabetes can cause various damaging consequences to the body such as Peripheral Neuropathy. Peripheral Neuropathy is the result of damage to one's peripheral nervous system. Uncontrolled/unregulated diabetes can cause permanent damage to the nerves. This damage manifest as tingling, numbness, or severe pain in hands and feet. Peripheral Neuropathy can also be caused by major injuries, infections, metabolic problems, HIV/AIDS, and even Chemo–induced diabetes [49]–[51]. More than 50% of the diabetes patients have neuropathy [52]. Being diagnosed with neuropathy can be devastating because once the nerves reach a certain amount of damage, it cannot return to normal. This leaves many people with limbs that are numb, or severely painful. Generally, patients with extreme pain get their limb amputated. However, there is a vast percentage of patients with numbness who are left with a functional limb that has no grip or grasping feedback [52]. These patients are the focus of this study. A wearable device with visual assistance to indicate grasp force would be immensely helpful for them.

1.5 Thesis organization

This report is based on a few published articles and some unpublished works to cover material and system development, fabrication methods, sensor characterization, and evaluation. Chapter two presents literature review, contemporary researches, and background of the work. Chapter three presents the sensor principle, characterization, fabrication via screen printing and molding, evaluation, and applications of screen-printed sensors. Chapter four presents 3D printed sensor, material and system development, 3D printed sensor evaluation, and applications. Finally, conclusions and future works are in chapter five.

CHAPTER II

LITERATURE REVIEW

2.1 Additive manufacturing

The ASTM international defines the terminology Additive Manufacturing (AM) as the “process of joining materials to make objects from three-dimensional (3D) model data, usually layer by layer, as opposed to subtractive manufacturing methodologies” [53]. Many traditional manufacturing processes involve machining or material removal which makes them subtractive methods. Although *3D printing* is a specific type of AM where objects are fabricated through material deposition, the term *3D Printing* is being more popular and widely used to denote AM in general. In this thesis, the term *3D Printing* was used to indicate the AM process. AM supports a variety of materials such as metal, plastic, ceramic, composite, and bio. The prime benefit of the additive method over the subtractive method is its ability to fabricate a 3D object easily from a computer-aided design (CAD) model without any special tooling, irrespective of the geometric complexity. Other advantages of AM include the scope for on-demand customization and modification, reducing material waste, reduced time and cost for small-quantity productions, ability to fabricate novel components with heterogeneous compositions [54]. Again, in the beginning, AM technology was used primarily for prototype fabrication. Therefore, another synonym for AM is rapid prototyping. However, AM has developed and evolved with time. Now, it is being employed for functional part fabrication for numerous applications [55].

There are various processes within additive manufacturing or 3D printing technology. The ASTM F42 Committee has divided them into seven categories as shown in Table 2.1 [53]. Generally, AM uses liquid photopolymer, solid filament or foil, or powder to fabricate a 3D object. Different commercial and proprietary terms got popular to represent various AM process. The type of manufacturing process also depends on the material for printing. Figure 2.1 shows a few of the AM processes [56].

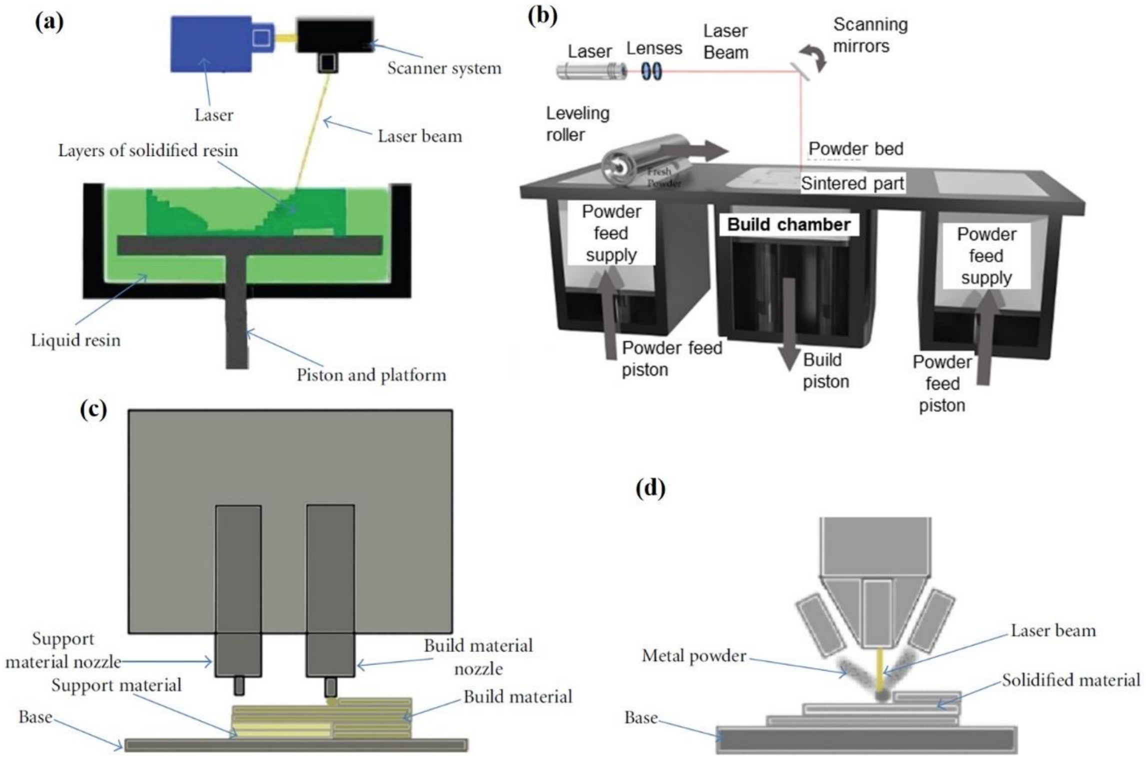

Figure 2.1. Different AM processes: (a) stereolithography apparatus (SLA); (b) powder bed fusion; (c) fused deposition modeling (FDM); and (d) laser metal deposition (LMD) [56].

Table 2.1. Different additive manufacturing processes and common materials

AM Process	**Technology Example**	**Material**
Binder jetting	3D printing (3DP)	Powdered plastic, metal, ceramics, glass, sand
	Voxeljet	
Directed energy deposition	Laser metal deposition (LMD)	Metal wire or powder, ceramics
	Direct metal deposition (DMD)	
Material extrusion	Fused deposition modeling (FDM)	Thermoplastic filaments and pellets, pastes, slurries
	Direct print photopolymerization (DPP)	
Material jetting	Multi-jet modeling (MJM)	Photopolymers, polymers, waxes
	Inkjet Printing (IP)	
Powder bed fusion	Selective laser sintering (SLS)	Plastics, metal and ceramic powders, sand
	Selective laser melting (SLM)	
Sheet lamination	Laminated object manufacture (LOM)	Paper or plastic Sheets, and Metal foils
	Ultrasonic additive manufacturing (UAM)	
Vat photopolymerization	Stereolithography apparatus (SLA)	UV-curable photopolymer resins
	Digital light processing (DLP)	

Material extrusion is one of the most common AM processes. Among the material extrusion methods, fused deposition modeling (FDM) is widely applied for low-cost 3D printing. Generally, it uses a thermoplastic solid filament for printing. In FDM, a heating system melts and extrudes the filament through a nozzle. The extruded filament solidifies at room temperature right after deposition. Another material extrusion process is direct-print with thermoset material. Generally, a photocurable prepolymer is developed with proper rheological property and extruded through a nozzle in the direct-print process. Next, the extruded filament is polymerized using ultraviolet (UV) light. This process is called direct-print photopolymerization (DPP) [57]. DPP is an effective technique to 3D print functional polymers. Especially, 3D printing of soft polymer-based electronics could greatly benefit by implementing this process. DPP is a very effective method for printing elastomeric electronics. In this work, the DPP process was implemented to 3D print the soft polymeric pressure sensors.

2.2 Soft pressure sensor

Soft pressure/tactile sensors are gaining significant interest and a major area of soft electronics. Smart technologies are now on the rise, and many smart devices require flexibility and stretchability [58]–[60]. Robotics [1], prosthetics [2], [3], wearable electronics [4], [5], and energy harvesting devices [6] are examples of technologies where soft and stretchable electronics would play an important role. In particular, flexible and stretchable sensors are gaining more attention because of their applications in shape-conforming systems or systems that have moveable parts [61], [62]. For example, wearable electronics for recreational use [63], medical/healthcare devices [64], and personal protection [65], [66] could be areas of application for such sensors. Along with mechanical flexibility, wearable devices that are in contact with the human body must also be designed to minimize discomfort and absorb some impact [67]. In addition to wearable devices, stretchable sensors might be used in other soft smart systems whose concepts are being explored such as tires [68], mattresses [69], packaging [70], automobile accessories [71], and non-wearable medical devices [72]. In many cases, rigid sensors are incompatible with deformable and free-form objects, generating the interest for sensors that are mechanically pliable.

Numerous studies on flexible and stretchable sensors have been conducted in the past decade. Sensors were proposed based on different working principles such as resistance [73], [74], capacitance (Figure 2.2) [75], piezoelectricity [76], optics [77], or electromagnetics [78]. These studies have generated significant progress in the area of flexible sensing and have shown potential for various applications. However, bridging the gap between advanced manufacturing and sensing approaches is still a field that requires improvement. Moreover, these sensors may lack reliability, cost-effectiveness, and conformability and stretchability of the conductive path [18], [79]. Limitations of the current solutions is the motivation of this work.

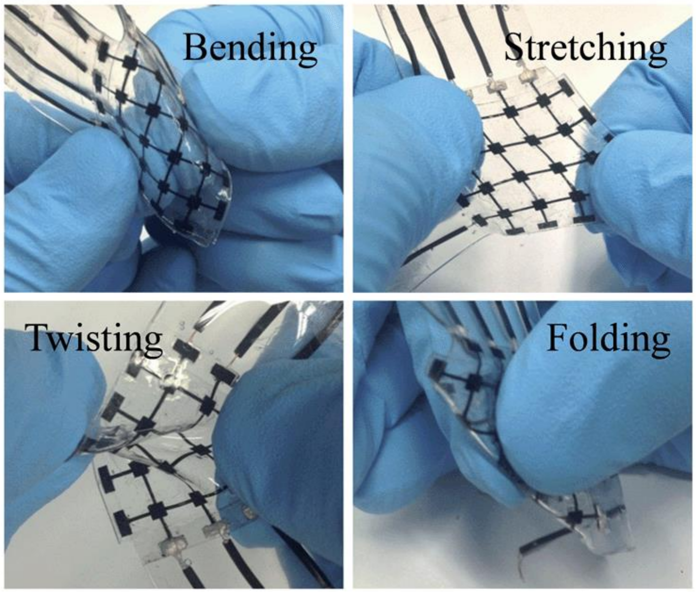

Figure 2.2. Capacitance-based flexible pressure sensor [75]. Copyright © 2014, Royal Society of Chemistry

2.3 Ionic liquid

An ionic liquid (IL) is a salt in the liquid state at below 100℃, or even at the room temperature. Ions are poorly coordinated in IL which results in a low melting point of it. Because of these floating ions, IL shows ionic conductivity. Ohno and Ito (1998) were among the first researches to report polymerized ILs. In that report, they proposed polycation with good ionic conductivity [80]. Noda and Watanabe also reported IL to prepare highly conductive polymer electrolytes [81]. Gradually, researchers used Ionic Liquids (ILs) in various applications [82]. ILs have been used for preparing polymer electrolyte [83], [84], sensors (Figure 2.3) [85], [86], and actuators [87], [88].

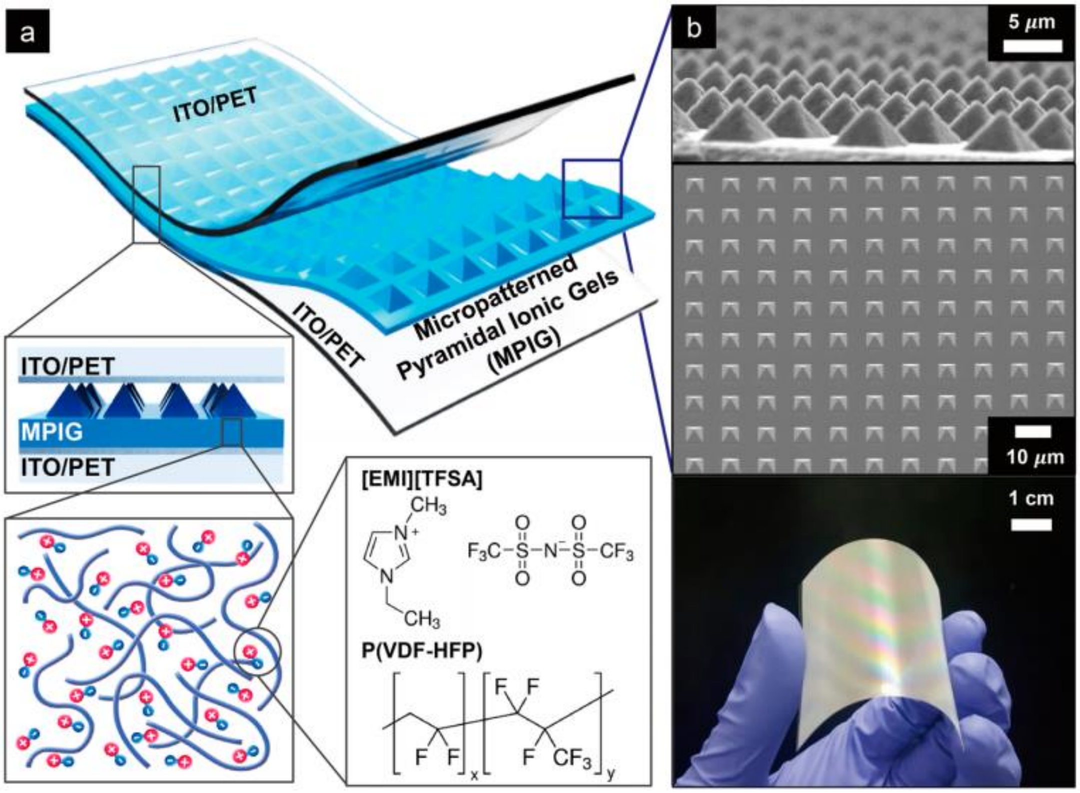

Figure 2.3. Micropatterned pyramidal ionic gels for capacitance-based pressure sensing [79]. Copyright © 2017, American Chemical Society

ILs have been subject of research interest because of their high ionic conductivity, negligible vapor pressure, low flammability, and electrochemical stability [22], [23]. The recent introduction of ionic liquids (ILs) to the area of soft pressure sensors has opened a new avenue of exploration for stretchable sensors. The unique feature of this IL-based stretchable sensor is that it provides a few degrees of freedom on controllable parameters such as IL concentration, sensor geometry, degree of polymerization, etc. which can be chosen according to applications. While ILs have been utilized to fabricate various devices for sensing but they generally lack manufacturing and design flexibility [21], [26]. 3D printed IL-based soft pressure sensor can provide not only reliable sensitivity but also manufacturing flexibility.

2.4 CNT/polymer composite for stretchable electrodes

The goal of this work is to develop a stretchable sensor. In addition to developing an IL-based piezoresistive polymeric membrane, stretchable conductive ink was also developed in this work. CNT/polymer composites have been proposed for stretchable conductors in several studies [89]–[91]. Incorporating CNTs into a non-conductive polymer matrix induces electrical conductivity in the CNT/polymer composite. With the CNT ratio beyond the percolation threshold, the composite shows high electrical conductivity and desired mechanical pliability [92]. Uniform dispersion of CNTs in a prepolymer is important to ensure reliable mechanical and electrical properties. However, uniform dispersion is challenging to achieve [93], [94]. Han et al. showed the effect of poor dispersion on electrical, morphological, and rheological properties of the composite [93]. Figure 2.4(a) illustrates untreated CNT dispersed in polypropylene, where it shows agglomerated and entangled CNT in the scanning electron microscopic (SEM) image [95]. This results in poor electrical conductivity and unstable mechanical behavior. CNTs can be treated in the presence of proper solvent and surfactant for detangling and obtaining better dispersion. Figure 2.4(b) shows treated CNT dispersed uniformly in polypropylene.

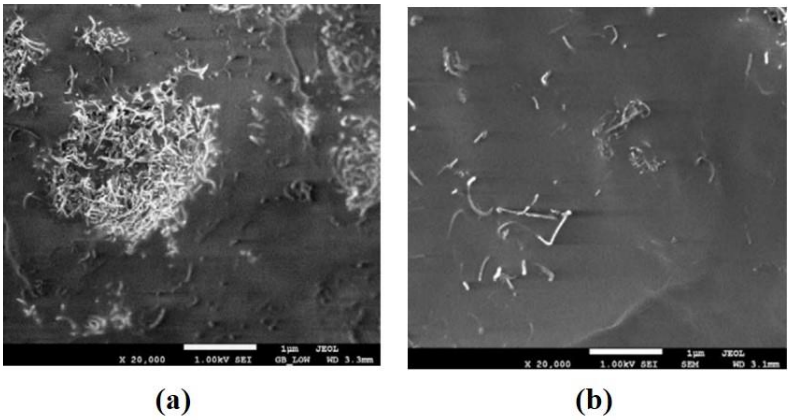

(a) (b)

Figure 2.4. Dispersion of MWCNTs in polypropylene: (a) 5 wt.% of non-treated MWCNTs were dispersed into the polypropylene; (b) treated MWCNTs were dispersed into the polypropylene. Printed with permission [95]. Copyright © 2020, SAGE Publications.

Noncovalent functionalization of CNTs using a surfactant showed promises for better dispersion while maintaining the intrinsic properties of the CNTs. Several studies applied Triton X-100 as a surfactant for better dispersion [95], [96]. Geng et al. achieved better electrical and mechanical properties by functionalizing MWNTs using Triton X-100 as a surfactant in an ethanol solution. As shown in Figure 2.5(b), Triton has a hydrophobic and a hydrophilic end. In the presence of proper solvent and ultrasonication, the hydrophobic end of Triton goes to CNTs and hydrophilic end goes towards the solvent. Through an unzipping mechanism, the surfactant isolates the nanotubes [97]. Ham et al. showed that the amide-based solvents work best for improved CNT dispersion [98]. Among the solvents investigated, N, N-dimethylformamide (DMF) and N-methyl pyrrolidone (NMP) provided the most power for the dispersion of CNTs. Although, NMP was proved to be more powerful in the dispersion of MWCNTs it has a higher boiling point (202°C). Therefore, DMF was more suitable as a candidate for the solvent. Also, ultrasonication is an effective technique for dispersion and stabilization of CNTs in the solvent [99]. Horn-type sonication generates high power to induce cavitation [100]. The strong shear force which exfoliates bundles and break up CNT agglomerates throughout sonication originates from the implosion of the cavitation bubbles.

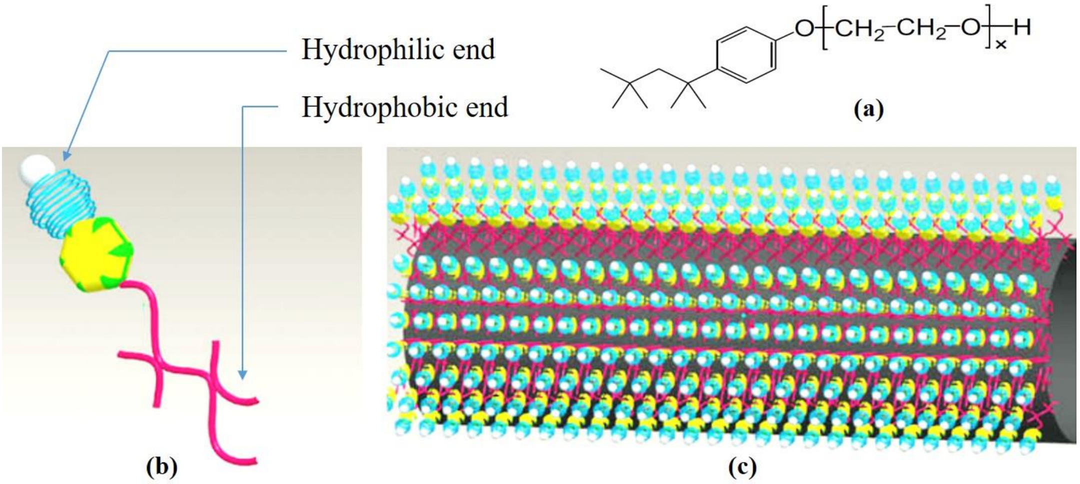

Figure 2.5. Triton X-100 as a surfactant for CNT dispersion: (a) chemical structure of Triton X-100; (b) schematic of a single Triton X-100 molecule; (c) hydrophobic end of surfactant goes to CNT that helps detangling. Reprinted with permission from [96]. Copyright © 2008, Elsevier Ltd.

CHAPTER III

IONIC LIQUID-BASED SOFT PRESSURE SENSOR AND FABRICATION VIA SCREEN PRINTING AND MOLDING

3.1 Introduction

An ionic liquid (IL)-based flexible and stretchable pressure sensor was developed. The sensor is a multi-layer soft sensor where the intermediate layer is a pressure-sensitive IL/polymer network and sandwiched between stretchable electrodes. It should be noted that several manufacturing processes can be followed to fabricate IL-based sensors depending on the shape and complexity requirements. A manufacturing technique that combines molding and screen printing processes is suitable for simple and flat sensors. However, when there is a need to fabricate a complex sensor or a sensor on a freeform surface and on-demand customization, 3D printing is believed to be the best manufacturing process for this purpose. The objective of this chapter is to evaluate the sensor to validate the proof of concept and to characterize the sensor in terms of geometry and material composition. To do that, a relatively simple sensor could be used as a representative. Therefore, the sensors for the preliminary evaluation were fabricated by screen printing and molding methods. Also, this hybrid manufacturing process provides an opportunity to fabricate the sensor fairly easily and implement it in various applications. A photocurable prepolymer was used as the base material which has been used for commercial 3D printers. Different applications of screen-printed sensors were also explored in this chapter.

3.2 Sensor design

The proposed soft pressure sensor includes five different stretchable layers. The intermediate layer (shown in blue in Figure 3.1(c)) is an IL/polymer network film with pressure-sensitive characteristics. When force is applied to the sensor, it is this layer that provides sensitivity. As shown in Figure 3.1(a) and (c), the intermediate pressure-sensitive layer is sandwiched between two MWCNT-based stripes. These two stripes of MWCNT/polymer composite work like stretchable conductive electrodes. Finally, there are top and bottom compliant layers that act as skin-like insulating films. The overlapping area where electrodes cross each other is the pressure-sensitive zone and is referred to as a *taxel.* Force is applied on the taxel to measure the sensor response. Sensors can be multi-taxel with an array of electrodes and can have complex shapes according to their application.

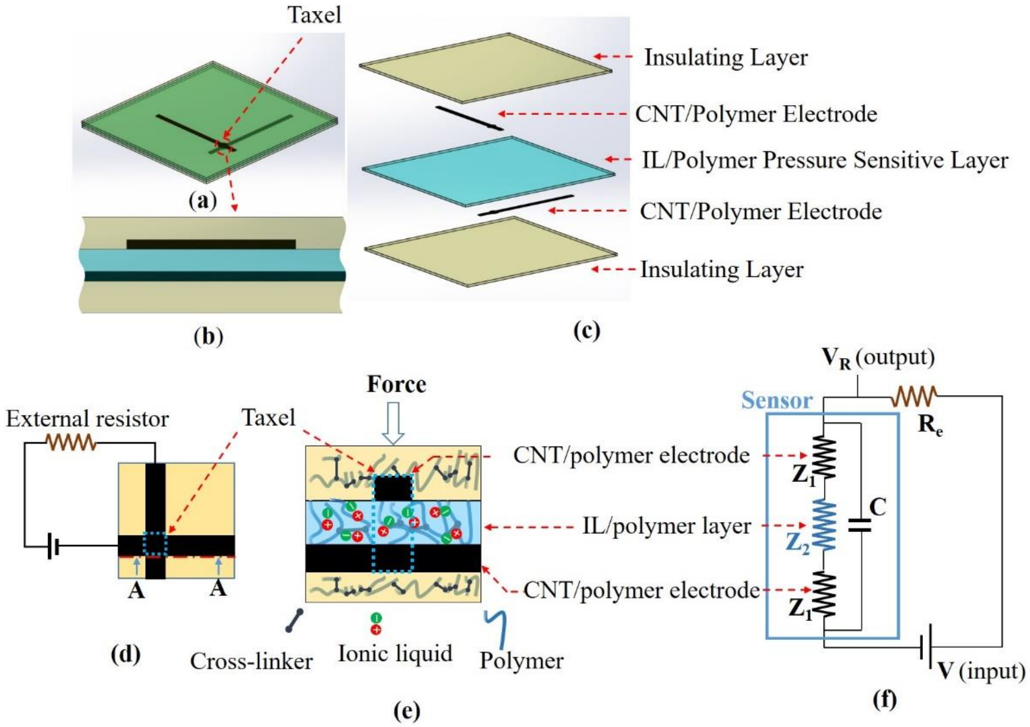

Figure 3.1. Schematic of the proposed sensor: (a) a simple single-taxel stretchable pressure sensor; (b) cross-section of a single taxel; (c) exploded view of the sensor with different layers; (d) simplified equivalent circuit while the sensor is connected to an external power supply; (e) cross-section of a single taxel with polymer chain and IL; (f) simplified wiring diagram with sensor resistance break-down [10], [68].

3.3 Sensor Mechanism

The electrical resistance of the intermediate layer of the sensor changes under force or deformation. To quantify the resistance change and evaluate the sensor, each taxel of the sensor is connected to a potential divider circuit, and the voltage across an external resistor (resistance, R_e) is measured. Figure 3.1(d) illustrates how a sensor is connected to the circuit. Because of the incorporation of IL, ionic conductivity appears in the intermediate layer of the sensor. The potential difference, which is provided between two MWCNT-based electrodes via an external power supply, creates activation energy for the ions in the intermediate layer to migrate between coordinate sites of a polymer chain and eventually results in ionic conductivity [20]. When compressive normal force is applied on a taxel, the sensor deforms and the distance between electrodes reduces. Also, an excitation in the IL/polymer layer takes place. Resulting from these factors, the electrical resistance of the intermediate layer decreases. Because of the conductance gain in the sensor system, the output voltage across the external resistor increases. The voltage across the external resistor (V_R in Figure 3.1(f)) is taken as a signal output of the sensor system. The MWCNT/polymer-based electrode could also be sensitive to force and might generate crosstalk under deformation. To nullify the piezoresistive effect of the electrodes, a high loading ratio of MWCNT (5% by weight) was used to fabricate the electrode material, which is higher than the electrical percolation threshold of MWCNT/polymer composites, as shown in Figure 3.2 [92], [101], [102]. The electrical resistance of the MWCNT electrode was measured as 20 to 30 KΩ, whereas the IL-based intermediate layer (when connected to the circuit) has a resistance of a few hundred MΩ (200 to 300 MΩ). Thus, by maintaining the electrical resistance Z_1 at a very low level compared to Z_2 (as shown in Figure 3.1(f)), the strain-sensitive effect of the intermediate layer remains dominant. Also, the sensor might have some capacitance effect due to charge polarization between the electrodes, which is shown as C in Figure 3.1(f)). However, for a sensor going through deformation or strain, the resistive effect is significantly dominant compared to the capacitance effect. Therefore, ignoring the capacitance effect, the sensor is considered as a resistive sensor in this study.

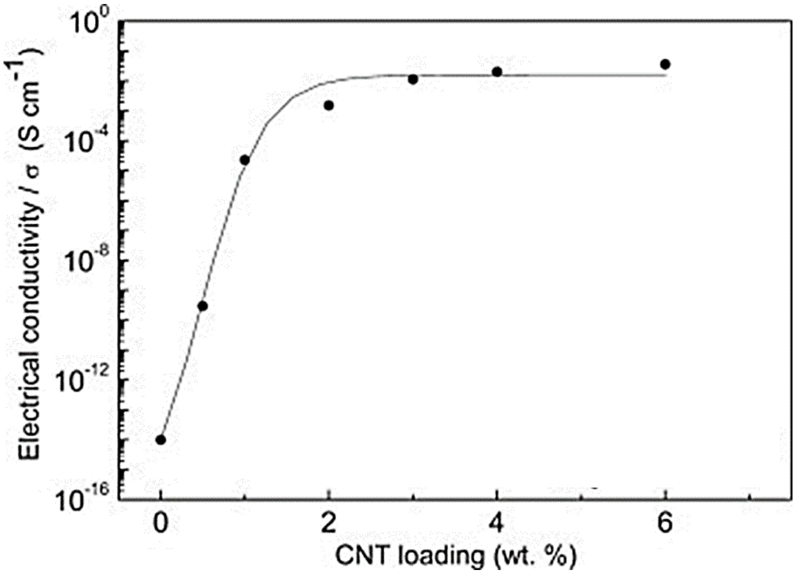

Figure 3.2. The electrical conductivity of CNT/polymer composite with increasing CNT loading ratio. Reproduced with permission from [92]. Copyright © 2010, Elsevier Ltd.

3.4 Material

The two outermost compliant layers were fabricated using a commercially available photopolymer (TangoPlus® FLX930, Stratasys, Eden Prairie, MN). TangoPlus is used for commercial 3D printers and produces a stretchable film after polymerization. TangoPlus was also used as the base polymer matrix for the IL-based intermediate layer and CNT/polymer composite. The ingredient information for TangoPlus is given in Table 3.1. TangoPlus was used for sensor fabrication because it is being used successfully for photopolymerization-based 3D printing. The ionic liquid used for the intermediate layer was 1-ethyl-3-methyl-imidazolium tetrafluoroborate ($EMIMBF_4$, ≥99.0%). The IL was purchased from Sigma-Aldrich Co. and used as received without further purification.

Table 3.1. Composition of TangoPlus

Component	**Percent**
2-Propenoic acid, 2-[[(butylamino)carbonyl]oxy]ethyl ester	<70
Isobornyl acrylate	<25
Phosphine oxide, phenylbis(2,4,6-trimethylbenzoyl)-	<2
Benzyl alcohol	<0.5
Acrylic acid ester	<0.3
Dipentene	<0.1
Isoamyl acetate	<0.1
Citral	<0.1
Geraniol	<0.01
2,6-Di-tert-butyl-p-cresol	<0.01

3.4.1 Pressure-sensitive intermediate layer

The intermediate layer is an IL-polymer blend. In general, the IL, $EMIMBF_4$ was mixed with TangoPlus at different ratios for different experiments. However, TangoPlus contains photo initiating and crosslinking agent. Therefore, to check the effect of degree of crosslinking and polymerization, IL was mixed with the base monomers of TangoPlus, a photoinitiator, and a crosslinker. For all other instances, IL was directly mixed with TangoPlus to fabricate the pressure-sensitive intermediate layer.

To investigate the effect of degree of crosslinking and polymerization on sensing performance, 2-[[(Butylamino)carbonyl]oxy]ethyl acrylate (BACOEA) was used as a base monomer in the intermediate layer. Glycerol propoxylate (1PO/OH) triacrylate (GPTA) and 2,2-dimethoxy-2-phenylacetophenone (DMPA, 99.0%) were used as crosslinking agent and photoinitiator, respectively. They were all purchased from Sigma-Aldrich Co. and used as received without further purification. First, 6 g of BACOEA was poured into a mixing container. Next, various amounts of GPTA (0.5 to 2 wt% to monomer (BACOEA)), 0.06 g of DMPA (1 wt% to BACOEA), and 0.06 g of $EMIMBF_4$ (1 wt% to BACOEA) were mixed with it. The solution of BACOEA, GPTA, DMPA, and $EMIMBF_4$ was mixed by the SpeedMixer™ (DAC 150.1 FVZ-K, FlackTek Inc.) at 2500 rpm for 5 min and poured into a PTFE Petri dish (79 mm in diameter). BACOEA polymerization was induced by UV (7.6 W or 1.25 W, OmniCure® S2000, Excelitas Technologies Co.) exposure for various time (30, 50, 60, 70, 80, 90 or 110 sec). The thickness of the produced BACOEA/$EMIMBF_4$ film was approximately 1 mm.

To investigate the effect of IL concentration and the thickness of the intermediate layer on the sensing performance, IL was mixed with TangoPlus using the high-speed mixer. IL concentration and intermediate layer thickness were varied for different experiments. Also, for general sensor evaluation and various applications of the sensor, IL was mixed with TangoPlus directly to prepare intermediate layer material.

3.4.2 MWCNT/polymer composite for stretchable electrodes

The material for stretchable electrodes of the sensor was prepared by dispersing and functionalizing MWCNT into a prepolymer. MWCNTs (Nano Lab Inc., Waltham, MA) with a length of 5–20 μm, a diameter of 10–30 nm, and purity over 85% were used. In the beginning, Triton X100 surfactant (Sigma-Aldrich, Milwaukee, WI) was dissolved into dimethylformamide (DMF; Sigma-Aldrich) before adding MWCNTs to the solution; a ratio of 1.0:3.5 MWCNTs to Triton X100 was used. The solution was sonicated using a Q700 sonicator (Qsonica, Newtown, CT) to realize global dispersion with a power of 700 W, a frequency of 20 kHz, and an amplitude of 50% for 20 minutes in the pulse mode (60 sec on, 10 sec off). The mechanism of nanotube exfoliation from bundles with the aid of a surfactant and ultrasonication provides high local sheer [97]. As shown in Figure 3.3, the high energy from ultrasonication swings the ends in the nanotube agglomerates that become adsorption sites for the surfactants. The surfactant continuously progresses along the nanotube length to isolate the individual tubes.

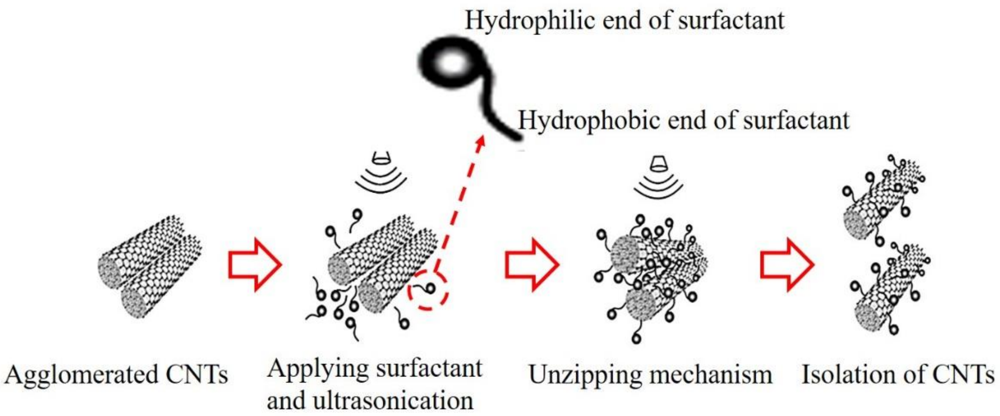

Figure 3.3. Detangling CNTs for uniform dispersion in the presence of surfactant and ultrasonication [97].

Figure 3.4(b) shows the ultrasonication process using a horn-type sonicator in the presence of solvent and surfactant. Following sonication, TangoPlus was added to the DMF/MWCNT solution and mixed using a magnetic stirrer. The MWCNT/prepolymer mixture was maintained on a VWR 1010 ALU hot plate magnetic stirrer (VWR, Chicago, IL) at 80℃ and 400 RPM for 48 hr to fully evaporate the DMF solvent. Finally, the paste was mixed again using a DAC 150.1 FVZ-K high-speed mixer (FlackTek, Inc., Landrum, SC) at 2500 rpm for one hour. To make it thermally curable, 5 wt.% of a thermal initiator (TRIGONOX 125C75, Akzo Nobel Functional Chemicals LLC, Chicago, IL) was added to the paste and mixed using the high-speed mixer for 5 min. Figure 3.4(c) shows the CNT/prepolymer after the dispersion and mixing process.

Figure 3.4. CNT dispersion into prepolymer; (a) MWCNTs; (b) ultrasonication in the presence of solvent and surfactant; and (c) CNT/prepolymer.

3.5 Sensor Fabrication

To characterize the sensor, simple single-taxel sensors are required. The sensors for these experiments were fabricated via a hybrid manufacturing process that included screen printing and molding. Figure 3.5 illustrates each step of the layer-by-layer fabrication process of the sensor. A square mold (50 mm × 50 mm) was used to make the stretchable sensor. TangoPlus was first poured into the mold (Figure 3.5(a)) and then photocured (Figure 3.5(b)) using ultraviolet (UV) light with a wavelength of 365 nm (OmniCure® S2000, Excelitas Technologies Co., Wheeling, IL) to create a bottom insulation layer with a thickness of 0.9 mm. Next, the first electrode was screen printed (Figure 3.5(c)) onto the bottom substrate with MWCNT-based paste using a mask. To prepare masks for screen printing, sheets of 200-μm-thick photo paper (Eastman Kodak, Rochester, NY) and a Silhouette Cameo cutting machine (Silhouette America Inc., Lindon, UT) were utilized. The printed CNT-based electrodes had a length of 40 mm, a width of 2 mm, and a thickness of 200 μm. After thermal curing of the electrode was performed (Figure 3.5(d)) at 80 ºC for 5 min, the IL/prepolymer mixture was cast in a mold (Figure 3.5(e)) and polymerized by UV light to create the intermediate layer (Figure 3.5(f)). A second electrode of the same dimension was printed (Figure 3.5(g)) on the intermediate layer and cured in the same manner as the first electrode (Figure 3.5(h)). Finally, a top insulation layer of 0.9 mm thick TangoPlus was cast (Figure 3.5(i)) and cured (Figure 3.5(j)). The overlapping area of these two electrodes works as a sensing unit (taxel). Figure 3.5(k-l) show the flexibility and stretchability of the fabricated sensor.

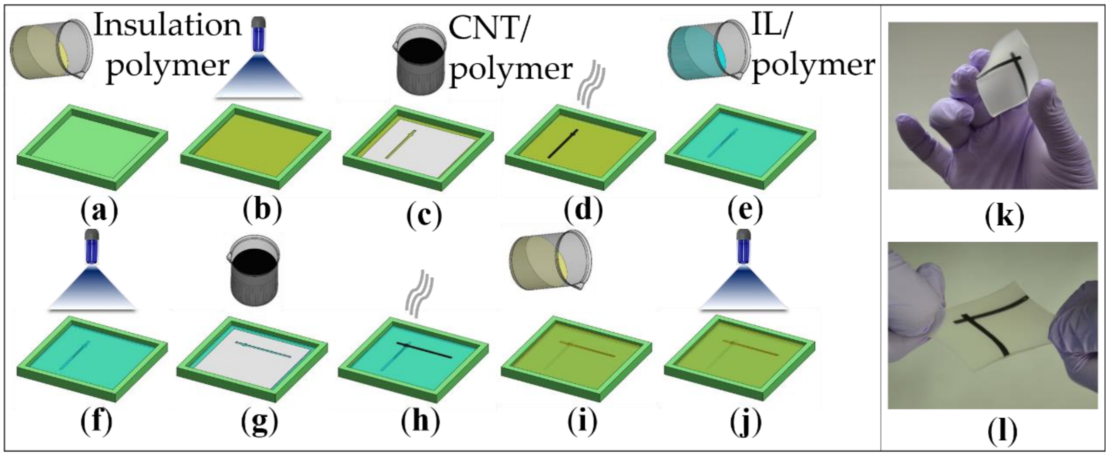

Figure 3.5. Sensor fabrication steps: (a) TangoPlus cast into a mold to create bottom insulation layer; (b) UV curing process for bottom layer; (c) screen printing of MWCNT/polymer paste for the first electrode; (d) thermal curing of MWCNT/polymer electrode; (e) IL/prepolymer mixture poured into the mold to create intermediate layer; (f) UV curing of IL/polymer layer; (g) screen printing of MWCNT/polymer to create a second electrode; (h) thermal curing of the second electrode; (i) TangoPlus poured to create a top insulation layer; (j) UV curing of the top layer; (k-l) flexible and stretchable sensor [10].

3.6 Experimental setup

The experimental setup consisted of a GTX250 Plus force gauge (Dillon, Fairmont, MN) with a resolution of 0.1 N, a BNC-2090A data acquisition system (DAQ) from

National Instruments (Austin, TX), an E3630A external power supply (Keysight Technologies, Santa Rosa, CA), and an A-LSQ075A-E01 motorized linear stage (Zaber Technologies, Vancouver, BC) with a resolution of 0.1 µm. The force gauge was mounted on the linear stage and was used to apply a compressive force on the taxel of the sensor. The whole system was interfaced with MATLAB to control the movement of the linear stage as well as to collect data from the DAQ and the force gauge. The sensor was connected to a potential divider circuit, and the voltage output across the external resistor (20 MΩ) was measured via the DAQ to quantify sensor response under force. The direct current (DC) voltage for the circuit was 24 Volts. The electrical resistance of the sensor was calculated using the following equation:

$$R_s = \frac{V_{in}}{V_{out}} R_e - R_e, \tag{1}$$

where V_{in}, V_{out}, R_s, and R_e represent the voltage supplied by the external power source (24 V), the voltage measured across the external resistor, the sensor resistance, and the external resistance (20 MΩ), respectively. The compressive strain given on the taxel was measured from the position data of the stage obtained via MATLAB. Next, a graph was plotted to show the relative change in resistance versus strain, which is indicative of the sensitivity. The sensor's response under compressive force was also investigated with respect to time. Figure 3.6 shows the wiring diagram and experimental setup used in this study, where the characterization experiments were conducted with a single-taxel sensor. The wiring diagram for multi-taxel sensors would be different which is explained in section 3.9.3.

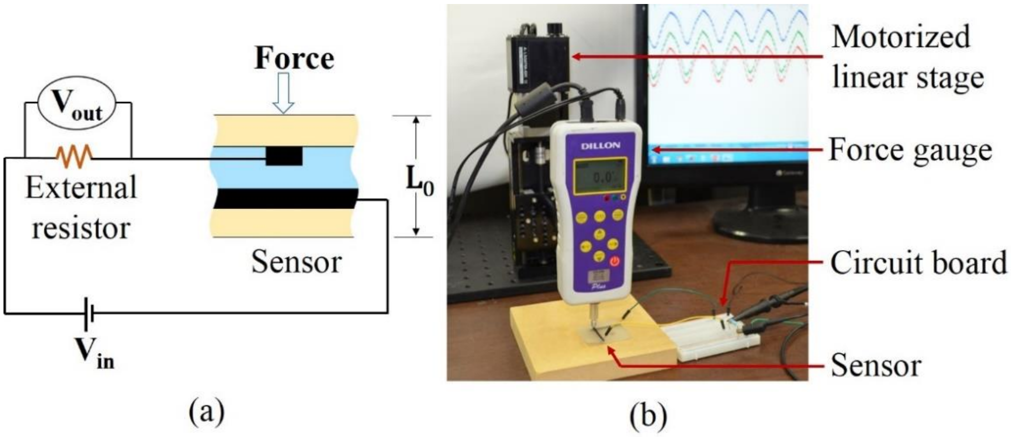

Figure 3.6. Sensor connected to circuit: (a) wiring diagram; (b) experimental setup [10].

3.7 Characterization

The soft pressure sensor was characterized for different variables. Experiments were conducted to investigate the effect of the degree of crosslinking, degree of polymerization, IL concentration, and intermediate layer thickness on sensing performance. The experimental results show a relationship between these parameters and sensitivity. The value of these parameters can be chosen from these experimental results according to the sensing applications.

3.7.1 Degree of crosslinking

To investigate the effect of the degree of crosslinking intermediate layer was fabricated using BACOEA as a base monomer, DMPA as a photoinitiator (1 wt.% of BACOEA), and $EMIMBF_4$ as IL (1 wt.% of BACOEA). Crosslinking agent GPTA was varied from 0.5 to 2 wt.% of BACOEA.

Swelling tests have been conducted to confirm the crosslink density of elastomers, and the degree of swelling is known to be dependent upon the crosslink density of elastomer networks [103]. To confirm the changes in crosslink density, the swelling behavior of the BACOEA/EMIMBF$_4$ blend is investigated. 5 specimens (~0.3 g each) were cut from each of the BACOEA/EMIMBF$_4$ composite samples, and the exact weight (W_0) was measured on a precision balance. Each specimen was put into a vial containing 30 ml of toluene and kept at room temperature for 2 h. Then, the specimens were removed from the toluene, and a small amount of toluene remaining on the surface of specimens was removed by short contact with a filter paper. The weight of swollen specimens (W_1) was determined immediately. Percentage swelling of the specimens is determined by using the following formula [104].

$$Weight\ gain\ (\%) = \left(\frac{W_1}{W_0} - 1\right) \times 100, \tag{2}$$

The result has relevance to the relative weight gain due to the incorporation of toluene molecules into the BACOEA/EMIMBF$_4$ composites matrices [104]. It is expected that the swelling ratio of a specimen decreases as the crosslinking density of the specimen increases. Figure 3.7 shows the swelling ratio of the BACOEA/EMIMBF$_4$ composite samples prepared using various concentrations of a crosslinking agent, GPTA (0, 0.5, 1.0, 1.5 and 2.0 wt% relative to BACOEA), and the percentage swelling decreases from 326.2% to 139.4% as a function of the amount of GPTA. It follows the tendency that the swelling ratios decrease as the concentration of a crosslinking agent increased [105].

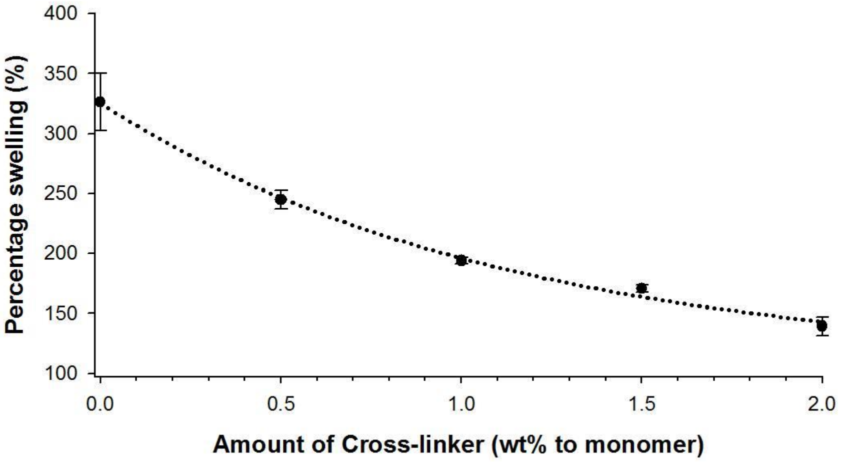

Figure 3.7. Effect of GPTA concentration on the percentage swelling of BACOEA/EMIMBF$_4$ blends [106].

The crosslinking density affects the degree of deformation of the BACOEA/EMIMBF$_4$ film induced by external stress. Owing to the external stress and material deformation, there is a change in electrical resistance of the material, and the performance of the sensors can be described by the resistance change. The relative deformation and resistivity variation with the amount of a crosslinking agent are investigated and presented in Figure 3.8(a) and (b) to confirm the effect of crosslink density. The electrical resistivity of the pressure sensors possessing a layer of BACOEA/EMIMBF$_4$ network was calculated using equation (1).

Figure 3.8(a) shows the change in strain ($\Delta L/L_0$, compressive deformation) versus the crosslink density for BACOEA/EMIMBF$_4$ blend samples with different applied forces, where ΔL is the difference between the current compressed thickness (L) and initial thickness (L_0) of sensors. The compressive deformation of intermediate layers cannot be separately measured without skin layers, since the intermediate layers are sticky and even the layers with less crosslinker (<1.0 wt% of GPTA) are easily broken. Therefore, in this study, the change in strain means the compressive deformation of all layers (skin and intermediate layers). For 5 N, the strain is not much changed even with the increase of crosslink density because the applied force is not enough to compress the composite sensor. On the contrary, the composite sensors with over 1.0 wt% of GPTA show that the compressive deformation decreases under 10 and 15 N due to the increase of mechanical properties of the intermediate layer (BACOEA/$EMIMBF_4$) induced by higher crosslink density. In Figure 3.8(b), the results indicate that the relative resistance of the composite sensors decreases with the crosslink density of the intermediate layer, and the change in the relative resistance ($\Delta R/R_0$) from 0 to 2 wt% of GPTA is approximately -50% under all forces. This reduction in relative resistance of the sensor is believed to be due to the formation of the conductive network induced by movements of polymer chains and ionic liquid domains during compression. At a lower content of GPTA, the relative resistance of the sensor has a greater variation with the pressure because the high crosslink density severely restricts the mobility of the polymer chains between the crosslink points, which induces the restricted mobility of the ionic liquid domains [107].

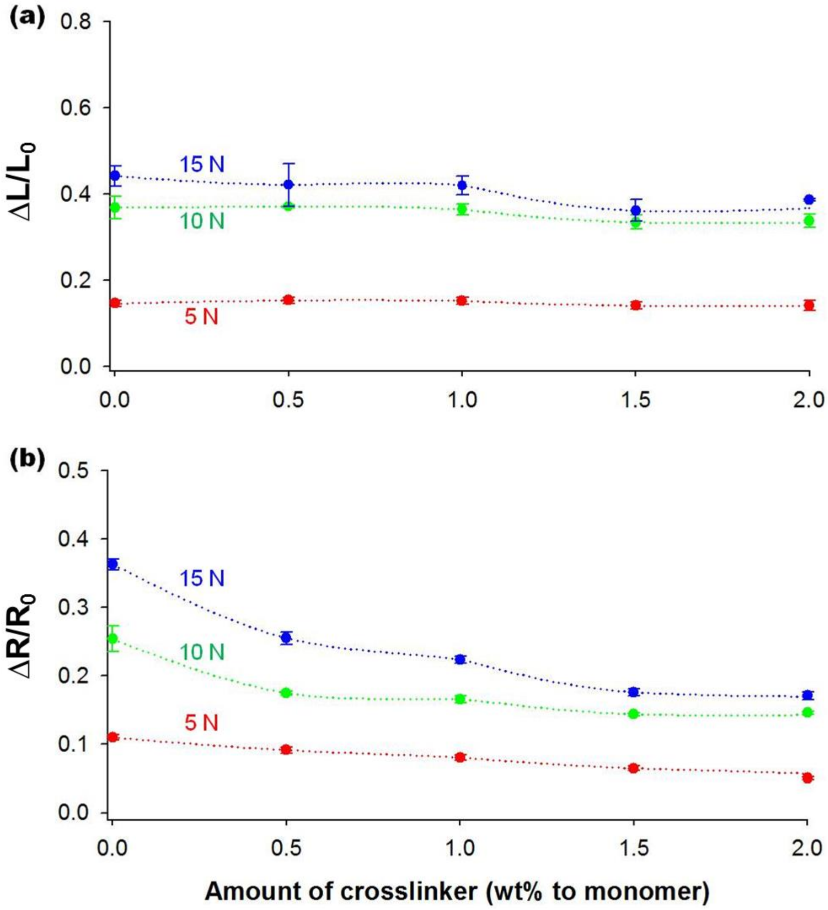

Figure 3.8. Effect of crosslinking density on (a) the compressive deformation and (b) relative resistance of BACOEA/EMIMBF$_4$ sensors [106].

Figure 3.9 represents the effect of crosslink density on the sensitivity of sensors. The sensitivity of the sensor was defined by the relative change in resistance per unit strain, $(\frac{\Delta R/R0}{\Delta L/L0})$. The idea for using the term $(\frac{\Delta R/R_0}{\Delta L/L_0})$ was taken from the gauge factor (*GF*) of strain sensors. The *GF* of a strain gauge is the ratio of relative change in electrical resistance *R* to the mechanical strain ε as shown in Eq. 3:

$$GF\ (strain\ sensors) = \frac{\Delta R/R_0}{\varepsilon} = \frac{\Delta R/R_0}{\Delta L/L_0}, \tag{3}$$

$$Sensitivity\ of\ the\ proposed\ sensor = \frac{\Delta R/R_0}{\Delta L/L_0}, \tag{4}$$

where R_0 and L_0 are stable (initial) resistance and initial length, respectively, and *GF* indicates the sensitivity of the strain gauge. Similarly, in the proposed sensor this term, ($\frac{\Delta R/R_0}{\Delta L/L_0}$) indicates responsiveness or sensitivity; the higher the value of this term, the more sensitive the sensor will be. Therefore, the sensitivity of the sensor is evaluated using Equation 4.

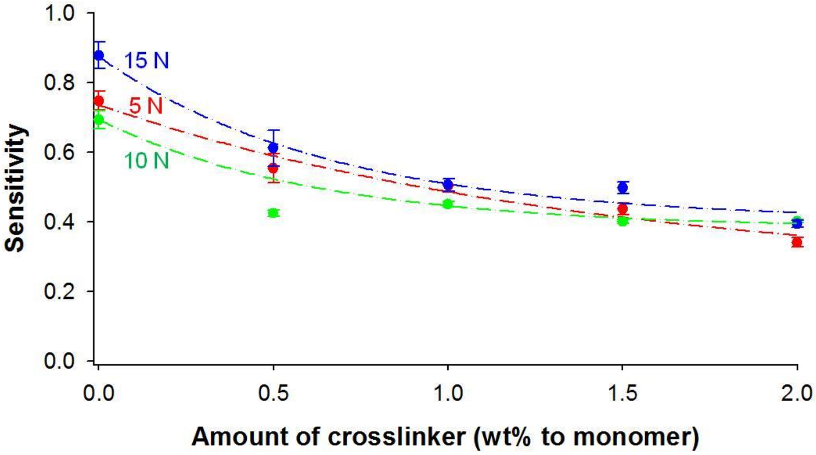

Figure 3.9. Effect of crosslinking density on the sensitivity of BACOEA/EMIMBF$_4$ sensors [106].

Ideally strain in the intermediate layer should be measured to calculate the GF. However, in these sensor characterization experiments, the strain was measured for the whole sensor, and thus the term ‘sensitivity’ for a sensor is used instead of ‘gauge factor’ for a sensing material even though the same equation is used. In Figure 3.9, the sensitivity in compressive strains decreases as the crosslinking density increases, and the values seem to converge to ~0.45 after 1 wt.% of GPTA. Although the highest sensitivity shows at 0 wt.% of GPTA, mechanical properties of the intermediate layer should be considered to fabricate the sensors. The output voltage of the sample with 0 wt.% GPTA fluctuates compared to other samples, which is induced by a lack of crosslinking. In this study, the values of sensitivity are far beyond compared with other researches; ~20 for carbon black/thermoplastic elastomer composites [108] and ~100 for ZnO nanowire/polystyrene films [109]. These low values of sensitivity are attributed to the skin layers, which affect the total deformation (compressive strain) of sensors, but not on the relative resistance.

3.7.2 Degree of polymerization

As the proper amount of GPTA is found as 1 wt.% relative to monomer (BACOEA), the crosslinking density appears to be the controlling factor for determining the sensor performance, and thus the GPTA content in the composite is fixed as 1.0 wt. % relative to monomer (BACOEA) for examining the effect of degree of polymerization on the sensor performance. The degree of photopolymerization can be easily controlled by different UV exposure times. The photopolymerization result of BACOEA/EMIMBF$_4$ blends is depicted in Figure 3.10. As the UV exposure time increases from 30 to 110 sec, the final conversion steadily increases from 82.1 to 87.5%. It has been known that free-radical photopolymerizations are generally very fast (cure achieved < 10 seconds) and reach very high conversions (conversion > 70-90% depending on the system).[30]

Therefore, Figure 3.10 indicates that the conversion already achieves over 80 % before 30 sec of UV exposure time and converges to ~86 % after 70 sec of UV exposure time.

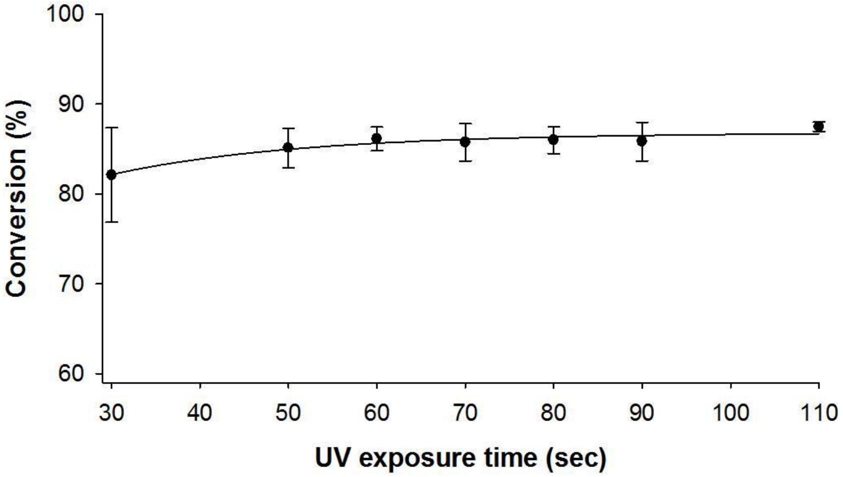

Figure 3.10. Reaction conversion of BACOEA/EMIMBF$_4$ blends at room temperature and constant UV intensity (1.52 W) for different exposure times [106].

As shown in Figure 3.11(a) and (b), the changes of relative deformation and resistivity are measured with the degree of polymerization controlled by reaction time. Figure 3.11(a) shows the change in compressive deformation with the degree of polymerization for BACOEA/EMIMBF$_4$ blend samples under different applied forces (5, 10, and 15 N). There is not much change in the compressive deformation for all sensors possessing various BACOEA/EMIMBF$_4$ films with the different degree of polymerization under each applied force. However, the compressive deformation increases slightly at 70 sec of UV exposure time, and then slightly decrease with UV exposure time at over 80 sec. In common with the compressive deformation, as shown in Figure 3.11(b), the relative resistance of the composite sensors increases at 70 sec of UV exposure time and then decreases with the UV exposure time at over 80 sec. The change in the relative resistance

($\Delta R/R_0$) from 70 to 110 sec of the UV exposure time is approximately -30% under all forces. These behaviors of the compressive deformation and relative resistance can be explained using the molecular weight of polymer chains. The molecular weight relies on the degree of polymerization and influences the melt viscosity [110]. Increasing molecular weight leads to a decrease of chain mobility and an increase of strength and toughness, as well as the glass transition temperature (T_g) [111], [112]. In addition, the physical and mechanical properties of polymers markedly depend upon the length of polymer chains (molecular weight) [113]. These are derived from the increase in chain interactions such as Van der Waals attractions and entanglements, which come with increased molecular weight [114]. In this experiment, BACOEA/EMIMBF$_4$ network have long enough chain length (molecular weight) to exhibit their polymeric properties at over 70 sec of UV exposure time. Therefore, the compressive deformation and relative resistance increase by 70 sec, whereas they decrease after 70 sec with increasing the UV exposure time. After 70 sec, high molecular weight brings high viscosity and thus induces the restricted mobility of polymer chains and ionic liquid domains. In other words, the resistance changes depend on the reduction of the ion mobility of ionic liquid, which is related to the increase of the molecular weight of BACOEA and the growth of a three-dimensional network that strongly limits the ion mobility of ionic liquid [115].

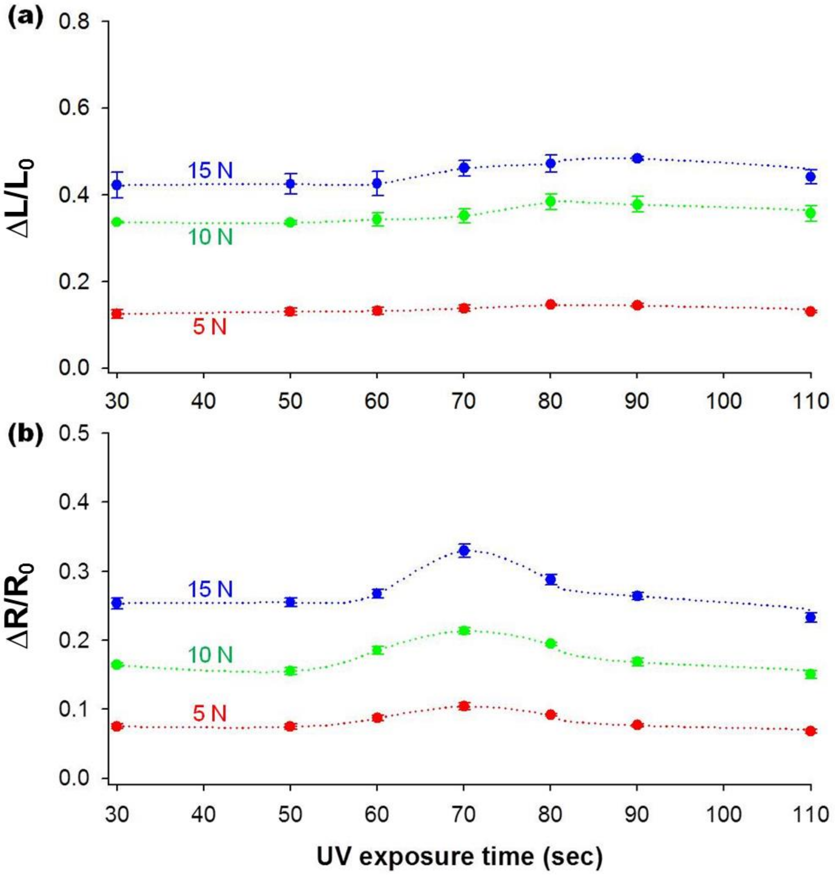

Figure 3.11. Effect of degree of polymerization on (a) the compressive deformation and (b) relative resistance of BACOEA/EMIMBF$_4$ sensors [106].

Figure 3.12 represents the effect of the degree of polymerization on the sensitivity of sensors. It is figured out that the limited mobility of polymer chains and ion liquid domains has a decisive effect on the sensitivity of sensors. The gauge factors in compressive strains increase to 25.8% (5 N), 24.2% (10 N), and 18.5% (15 N) with elevating UV exposure time by 70 sec. As discussed above, the BACOEA/EMIMBF$_4$ blends need 70 sec of UV exposure time at least in order to reach enough chain length (molecular weight), which exhibits the physical and mechanical properties as a polymer composite. However, the gauge factors decrease to 29.4% (5 N), 26.5% (10 N), and 23.9

(15 N) between 70 sec and 90 sec of UV exposure time due to the limited mobility of polymer chains and ion liquid domains induced by the higher molecular weight and three-dimensional network of BACOEA/EMIMBF$_4$ network, and then the gauge factors approach steady values.

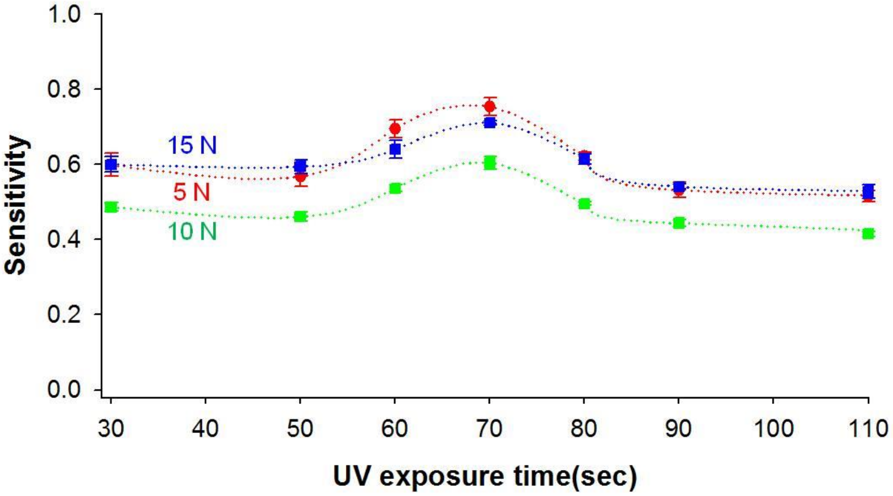

Figure 3.12. Effect of degree of polymerization on (a) the compressive deformation and (b) relative resistance of BACOEA/EMIMBF$_4$ sensors [106].

These results illustrate the interplay between the crosslinking density and degree of polymerization on determining the performance of the BACOEA/EMIMBF$_4$ blend sensing materials for stretchable tactile sensors. These factors impact the mobility of polymer chains and ionic liquid domains. Higher crosslink density and molecular weight of the BACOEA/EMIMBF$_4$ blend leads to the increase of mechanical properties and the growth of a three-dimensional network.

3.7.3 Ionic liquid concentration

To investigate the effect of IL concentration on sensing performance, the intermediate layer was fabricated by mixing IL into TangoPlus. So, for these set of experiments, different pressure sensitive TangoPlus/$EMIMBF_4$ films were created by varying the concentration of IL ($EMIMBF_4$) in the prepolymer blend from 0.5 wt.% to 10 wt.%.

To determine the effect of IL concentration, performance was evaluated for sensors with IL concentrations of 0.5 wt.%, 1.0 wt.%, 3.0 wt.%, 5.0 wt.%, and 10.0 wt.% in the IL/polymer intermediate layer, while all other features were kept constant. The compressive force was applied on a taxel (2 mm × 2 mm) at a probe speed of 0.023 mm/s, where the probe diameter was 4.0 mm, and the time, force, deformation, and voltage output were measured. The electrical resistance R_s of the sensor connected in the potential divider is calculated using Eq. 1.

Figure 3.13(a) shows the relative changes in resistance versus the compressive strain curve for sensors with different IL concentrations, where ΔL is the change of the thickness and L is the original thickness of the sensor. The full sensor, which consisted of five layers, was studied as a unit, and the compressive strain mentioned here is the strain for the five layers combined. The sensor thickness L_0 was maintained at 2.75 mm with approximately 0.9 mm thickness for the top, bottom, and intermediate layers. While the sensor goes through a deformation under force, the voltage output across the external resistor increases due to the decrease in sensor resistance, represented by ΔR. Figure 3.13(a) shows that, with the increase in the IL concentration, there is a larger change in relative resistance for the same amount of strain. However, it is evident from the graph that once a certain limit is reached, there is no change in relative resistance for the sensors with higher IL concentrations. In Figure 3.13(a), the curves for sensors with 3.0 wt.%, 5.0 wt.%, and 10.0 wt.% overlap, but there is a noticeable difference from 1.0 wt.% to 3.0 wt.% of IL concentration.

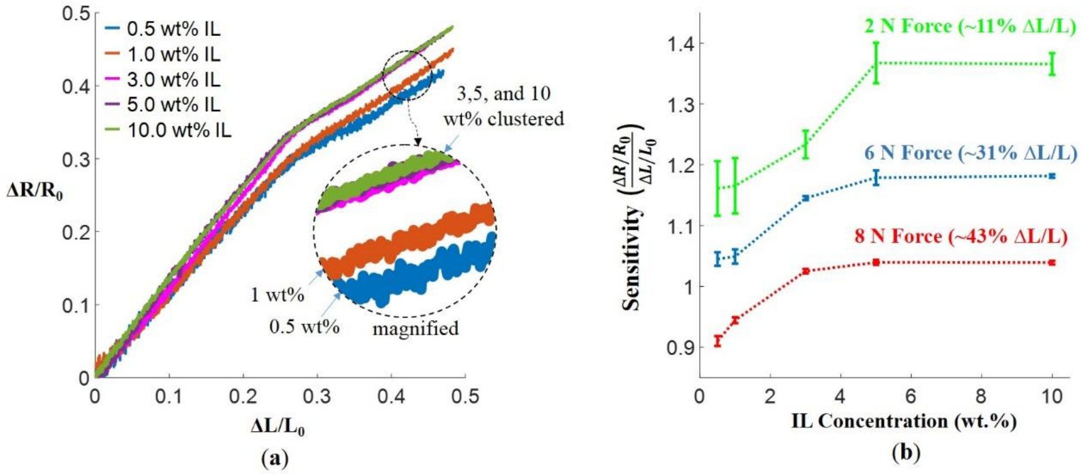

(a)

(b)

Figure 3.13. Effect of IL concentration in the IL/polymer layer on the sensor performance: (a) relative change in resistance vs. compressive strain curve for different IL concentrations in intermediate layer material; (b) sensitivity vs. IL concentration in IL/polymer blend for different forces [10].

Another obvious trend is that once 25% of the compressive strain (which equates to almost 5 N compressive force) has been reached, the slopes of all the curves decrease considerably. This indicates that beyond 25% strain or 5 N force, the sensitivity of the sensor will be a little less than that at the initial 25% strain. Such a nonlinear response to various strains has been also observed in other piezoresistive sensors [116]–[118]. Figure 3.13(b) illustrates relative changes in resistance per unit compressive strain $(\frac{\Delta R/R_0}{\Delta L/L_0})$ for different forces versus IL concentration in the IL/polymer network of the sensor. Figure

3.13(b) shows sensitivity vs. IL concentration curves for compressive forces of 2 N, 6 N, and 8 N. Voltage output for these forces was obtained from the experimental results shown in Figure 3.13(a). Resistance and deformation were calculated from the voltage and stage position data respectively.

Results shown in Figure 3.13(a) and (b) demonstrate that with the increase of IL concentration in the IL/polymer layer, the sensitivity of the sensor increases up to a limit and then becomes stagnant. From Figure 3.13(b), it can be seen that there is a significant increase in sensitivity from 0.5 wt.% to 5.0 wt.% of IL concentration. This is to be expected, as higher IL concentrations are known to increase the ionic conductivity (σ) of an IL-containing polymer [82], [119]. The increase in sensitivity, when the ionic liquid concentration increases from 0.5 to 5.0 wt.%, might result from the increased number density of charge carriers that are imidazolium (EMI^+) cations and tetrafluoroborate (BF_4^-) anions due to the higher ion concentration (p), leading to an increase in the ionic conductivity ($\sigma = ep\mu$, where e is the elementary charge and μ is ion mobility) [120]. This is why the higher IL concentration significantly reduces the resistance ($R \sim 1/\sigma$). However, the experimental results indicate that there is a saturation in conductivity after 5.0 wt.% of IL, which does not increase sensitivity beyond this concentration. This is presumably because, at higher IL content, all the ions may not participate in ion conduction, but some of the diffusive species can form ion clusters or aggregates which are neutral and do not carry electric charge [121]. Therefore, the ionic clusters due to the strong binding energy of the ion pairs in a low dielectric elastomer medium lead to a nonmonotonic IL concentration dependence of the sensitivity.

It can also be noticed from Figure 3.13 that the sensor is more sensitive at a lower range of force. Figure 3.13(a) shows a steeper slope and higher sensitivity up to 25% strain (~5 N force), which may be due to the initial ion excitement in the intermediate layer at the beginning of deformation. Also, as the sensor is multilayered and made of multiple materials, strain may not be uniform throughout the sensor under compression. While the strain shown in Figure 3.13(a) is for the entire sensor, the sensor response is primarily controlled by the strain in the intermediate layer. It is likely that at the beginning of deformation, strain in the intermediate layer is significant; but as the force increases, strain in the bottom layer becomes higher. Changes of strain in the intermediate layer may become smaller over time. It is also possible that in the higher deformation the viscoelastic effect of the TangoPlus elastomer as a polymer matrix of the intermediate layer also contribute to the resistance response; i.e., the ion-conducting networks are affected by the stress relaxation caused by the viscoelasticity of the elastomer [21], [106]. These factors are may be the causes of the initial higher sensitivity.

In Figure 3.13(b), it can be noticed that the error bars at lower levels of force are larger than those at higher forces. It happens since at the beginning of deformation, the resistance change data is a bit scattered; this may result from ion mobility occurring due to the initial excitement. However, this does not affect the sensor performance, as the resistance change under force is high enough to neglect the scatterings. To plot the 2 N sensitivity line in Figure 3.13(b), the average of several data points at 2 N was considered, and hence the error bar was shown. To reach 50% strain, the force was gradually increased on the sensor from 0 to almost 9 N. As the resolution of the force gauge was low (0.1 N), several data points at each force point were recorded instead of using only one data point for each force (e.g., when force increases from 1.9 to 2.0 N, there were no force data for 1.91 N, 1.92 N and so on). Although the probe was continuously moving towards the sensor and the actual force was continuously increasing, finer force data were not recorded. This is the reason why with a sampling rate of 22 Hz, several data points were seen either at 2.0 N or 1.9 N force. Multiple voltage and stage position data obtained at a force of 2.0 N could actually be data from 1.95 N to 2.05 N.

3.7.4 Intermediate layer thickness

To study the effect of the thickness of the pressure-sensitive intermediate layer on the sensor performance, tests were conducted using sensors with intermediate layer thicknesses of 0.5 mm, 1.0 mm, 2.0 mm, and 3.0 mm, while all other parameters remained fixed. The intermediate layer was fabricated with a TangoPlus/EMIMBF$_4$ blend. The IL concentration used for the IL/polymer layer was 1.0 wt.%. A compressive force was applied on a 1.5 mm × 1.5 mm taxel at a probe speed of 0.012 mm/s, voltage measurements across the sensor were collected, and the sensor resistance under force was calculated using Eq. 1.

Figure 3.14(a) shows the relative change in resistance versus the compressive strain for different intermediate layer thicknesses of the sensor. From Figure 3.14(a), it is clear that with the increase of the intermediate layer thickness, the relative change in electrical resistance decreases for the same amount of strain. The sensor with a 0.5-mm intermediate layer thickness shows the maximum change in relative resistance for a constant strain. In other words, the thinner the IL/polymer layer, the more sensitive the sensor. It can also be noticed that there is a change in the slope of the curve after 25% strain, indicating a slight drop of sensitivity after that point. Figure 3.14(b) shows the relative change in resistance per unit compressive strain ($\frac{\Delta R/R_0}{\Delta L/L_0}$) versus IL/polymer layer thickness for a force of 3 N, 5 N, and 7 N, where the term ($\frac{\Delta R/R_0}{\Delta L/L_0}$) denotes the sensitivity of the sensor. Taken together, these graphs indicate that using a 0.5 mm or 1.0 mm thickness for the intermediate layer provides a more stable and sensitive response in the sensor.

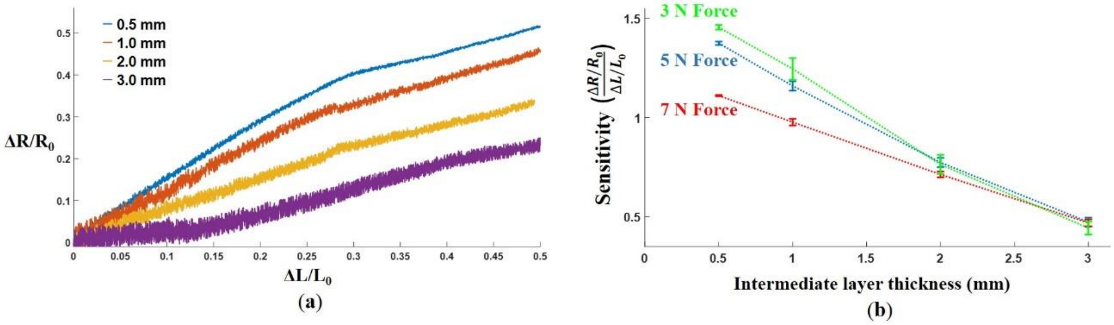

Figure 3.14. Effect of intermediate layer thickness on the sensor performance: (a) relative change in resistance vs. compressive strain curve for different intermediate layer thicknesses; (b) sensitivity vs. intermediate layer thickness of the multilayer sensor [10].

The plots in Figure 3.14(a) and (b) illustrate that with an increase in sensor thickness, the sensitivity of the sensor decreases. The thicker sensors in this study (2 mm and 3 mm) are not sensitive; and they do not show much variance in sensitivity with force, as electrical resistance is proportional to the length of the conductive path. The IL/polymer layer has a very high electrical resistance, and it almost loses conductivity with increased thickness. Hence, the relative change in resistance is also very low, and sensitivity goes down for thicker sensors. Figure 3.14(b) also denotes that for the thin IL/polymer layers (0.5 mm and 1 mm), sensors are more responsive at lower force ranges, since the curve for a 3-N force is above the curve for a 7-N force. This is similar to the phenomenon shown in

Figure 3.13. However, an interesting difference is noticed for the sensor with the thickest IL/polymer layer (3 mm), where sensitivity is a little higher at higher forces. The thickest intermediate layer has the highest electrical resistance; when force is applied, the resistance change created by a small deformation is lower as compared to the initial higher resistance. Only when the deformation or force is very high, there is a significant difference in the signal output. Therefore, a sensor with a thicker intermediate layer could be applied in applications with larger force.

3.8 Sensor evaluation

Sensors fabricated via molding and screen printing processes were evaluated for different conditions. Reasonable values of manufacturing variables were chosen based on the characterization experiments conducted in section 3.7. The intermediate layer was fabricated using TangoPlus/EMIMBF$_4$ blend. Fabricated sensor was also compared with a commercial flexible force sensor.

3.8.1 Sensitivity and dynamic range

As described earlier, sensitivity in this report was denoted by the relative change in resistance per unit strain, ($\frac{\Delta R/R_0}{\Delta L/L_0}$). The dynamic range (DR) of a pressure sensor indicates the working range of the sensor which is determined from the lowest and highest pressure measured by the sensor. In this work DR was calculated in decibel (dB) using the following equation:

$$DR = 20 \times log_{10}\left(\frac{P_{max}}{P_{min}}\right), \quad (5)$$

where P_{max} and P_{min} are the maximum and minimum pressures that can be measured by the sensor. The results reported in the previous sections imply that an IL concentration in the range of 1 to 5 wt.% and an intermediate layer thickness in the range of 0.5 to 1 mm are suitable to use in fabricating a sensor that is sensitive and performs well for a reasonable dynamic range (0–15 N). While sensors could be more sensitive if an intermediate layer thickness of 0.5 mm or smaller is used, some manufacturing difficulties may be encountered when fabricating a very thin layer. Sensors outside the dynamic range stated above can be explored and fabricated by varying the studied parameters. For instance, sensors can be constructed with a thicker intermediate layer or a lower IL concentration to employ in higher force applications.

In this experiment, a sensor was fabricated with 3 wt.% IL concentration and 0.9-mm intermediate layer thickness to test the sensor response and reliability. A four-step force loop (3, 6, 8, and 10 N) was created, where force was applied on the sensor for 10 seconds and where the sensor went through multiple loops, and the signal output was recorded. Figure 3.15(a) shows results obtained over time to demonstrate the reliability of the sensor. The actual force was measured using a force gauge, and voltage output data were collected to study the sensor response under force; both sets of data are presented in Figure 3.15(a). It can be noticed from this figure that the output signal from the sensor is consistent with a time delay of less than ten milliseconds between the applied force and the output signal (V_{out}), that are found to be reliable over a long period.

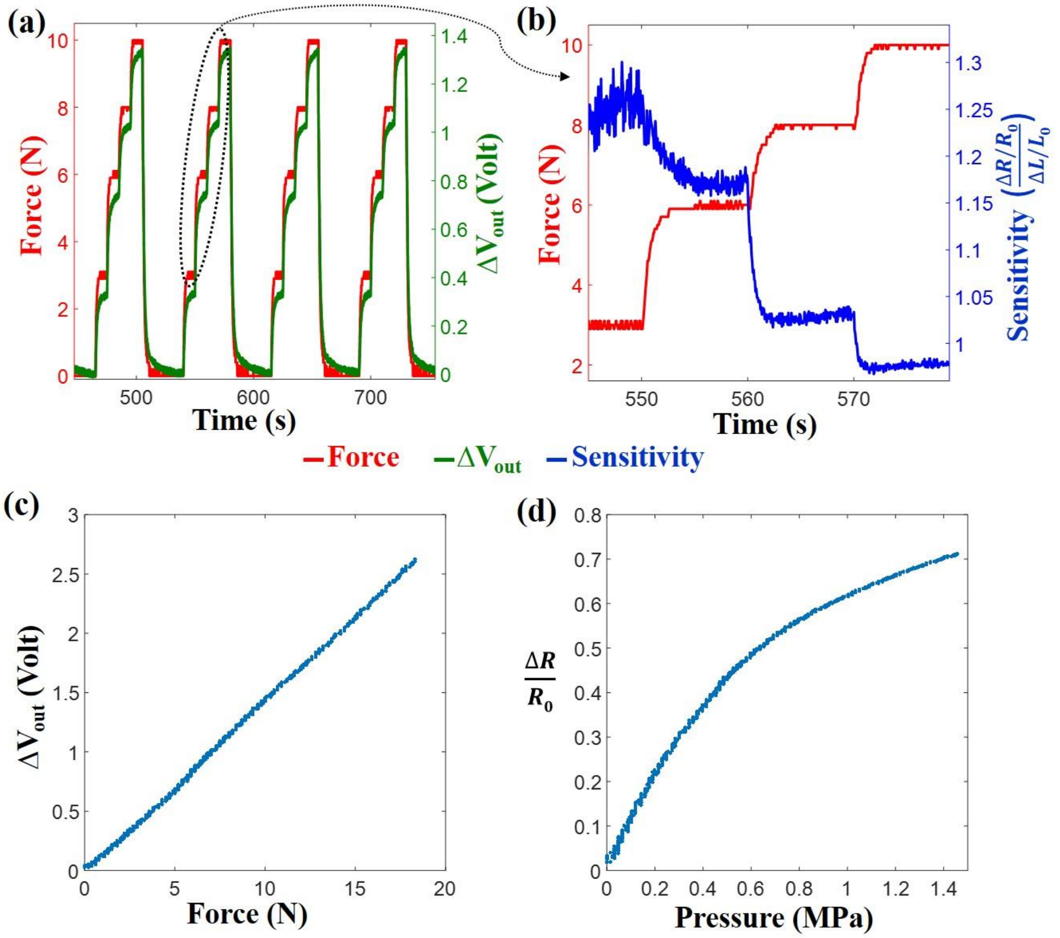

Figure 3.15. The sensor response was studied from voltage output across the external resistor: (a). force (red) and voltage (green) output with respect to time when compressive forces of 3 N, 6 N, and 10 N were applied on the sensor taxel; (b) sensitivity is shown for different force levels; (c) change in voltage output vs. compressive force; (d) relative change in resistance vs. pressure [10].

Figure 3.15(b) presents the results for one of the loops to show the sensitivity under different forces. As noticed earlier, the sensor showed higher sensitivity at a lower force with a bit scattered sensitivity. Another experiment was performed to determine the dynamic range and the trend of the sensor response with respect to force. Figure 3.15(c) and (d) show changes in voltage output across the external resistor and the relative resistance change in the sensor with increasing force, where force was applied up to nearly

20 N. A linear relation between the voltage change and force was noticed as illustrated in Figure 3.15(c). Relative change in electrical resistance of the sensor under increasing pressure converges to a steady value, which is evident from Figure 3.15(d). The sensor was found to be sensitive in the range of 50 kPa to 1.5 MPa. The DR was calculated to be around 30 dB. Various DR bound can be achieved by varying the IL concentration or intermediate layer thickness. The signal-to-noise ratio (SNR) for the output voltage was calculated around 40 dB.

3.8.2 Comparison with commercial sensor

The sensor was also evaluated in comparison with a commercial piezoresistive sensor. Soft, stretchable pressure sensors are not generally commercially available. There are some flexible piezoresistive force sensors commercially accessible. FlexiForce A201 (Tekscan, Inc., Boston, MA) is one of the common force-sensing resistors, which has a pressure-sensitive film between conductive electrodes. A FlexiForce A201 for lower force range (0–4 N) was tested. Figure 3.16(a) shows the resistance vs. force curve for the FlexiForce sensor and Figure 3.16(b) shows the result for a similar experiment on the proposed IL-based sensor. The proposed sensor shows linear behavior with force when FlexiForce exhibits a drastic shift in resistance at the beginning and slow variation after 0.5 N force. Figure 3.16(c) and (d) show sensor responses for a 4-N force loop on FlexiForce and proposed IL-based sensor, respectively. The proposed sensor showed better similarity to the force curve than FlexiForce at the lower force level.

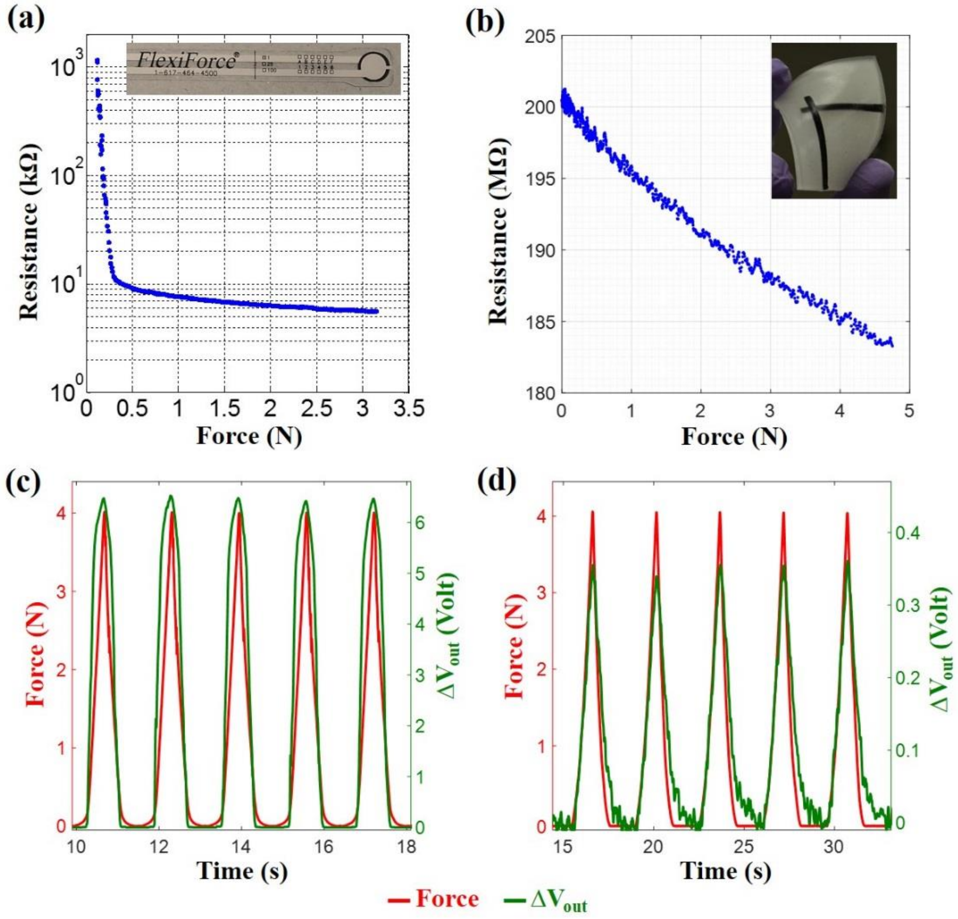

Figure 3.16. Comparison between FlexiForce A201 and proposed IL-based sensor: (a) resistance vs. force for FlexiForce; (b) resistance vs. force for IL-based sensor; (c) applied force (red) and sensor output (green) for a 4-N multi-loop force on FlexiForce; (d) applied force and sensor output for IL-based sensor [10].

3.8.3 Temperature dependence

The IL/polymer membrane shows a temperature-dependent electrical conductivity. Due to that, the sensor response also changes with temperature. To investigate the glass transition temperature of the IL/polymer membrane, differential scanning calorimetry (DSC) test was conducted using a Q2000 scanning calorimeter (TA Instruments, New Castle, DE). The IL/polymer membrane was fabricated using 1 wt.% IL with TangoPLus and through subsequent polymerization. Figure 3.17(a) shows the DSC test result. The glass transition temperature was measured around -10℃. Next, the sensor was tested with varying temperature but without any applied force. A sensor with 1 wt.% IL was fabricated and placed on a hot-plate to increase the temperature from room temperature to 65℃. A thermocouple thermometer was used to measure the sensor surface temperature. As shown in Figure 3.17(b), the output voltage and temperature curves followed a similar trend. Increased voltage output indicates an increase in the electrical conductivity of the IL/polymer layer. So, Figure 3.17(b) demonstrates an increase in conductivity with increased temperature and a decrease in conductivity with reduced temperature.

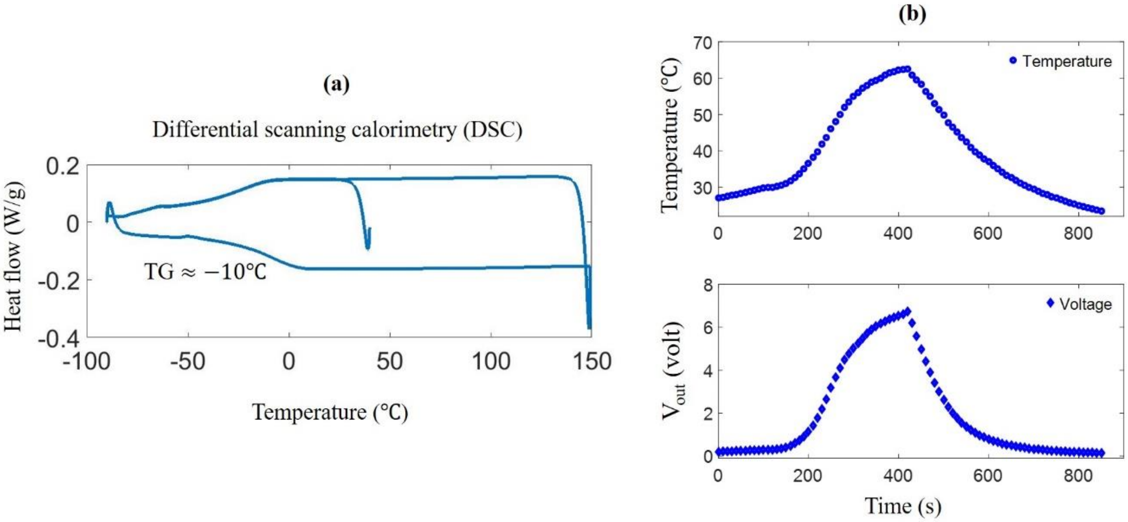

Figure 3.17. Temperature sensitivity: (a) differential scanning calorimetry (DSC) test of IL/polymer showing glass transition temperature at around -10℃; (b) sensor output with the varying temperature at the same timestamp.

At higher temperature, the ion mobility increases in the IL/polymer network [122]. That may contribute to the rise in the electrical conductivity with an increase in temperature. Equation 6 shows how the ionic conductivity, σ, depends on the ion mobility (μ), ion concentration (p), and elementary charge (e) [120], [123]. With the electrical field charged, ions get accelerated and jump from one stable site to another while the movement occurs along the direction of the electrical field [20]. The mobility, μ, is defined as the velocity when the magnitude of the electrical field is unity. Equation 7 shows the Arrhenius-type relation between temperature and ion-mobility [123].

$$\sigma = ep\mu\,, \tag{6}$$

$$\mu = \frac{vea^2}{k_B T}\left[exp\left(-\frac{E_a}{k_B T}\right)\right], \tag{7}$$

where v is the vibration frequency of the solid, a is the distance between two adjacent sites where ions jump between them, E_a is the activation energy of diffusion, k_B is the Boltzmann constant, and T is the temperature.

The sensor was also tested under force at different temperatures. Figure 3.18(a) shows the sensor output at different temperatures when it went through five 9-N force cycles at 10℃, 25℃, 40℃, 60℃, 80℃, and 100℃. The sensor was connected to a potential divider and supplied with 10 V input voltage. Voltage output was measured across the external resistor of 20 MΩ. As illustrated in the figure, with the increase in temperature voltage output increases. It is observed that at around 100℃, IL/polymer conductivity increased so significantly that 9 V out of the supplied 10 V was consumed by the external resistor. Also, voltage output under force showed greater deviation at higher temperature. However, at 100℃, the sensor becomes very conductive and loses the ability for increasing the conductivity any further. It was also observed that the IL/polymer conductivity decreases significantly under 15℃ and the sensor loses sensitivity. Figure 3.18(b) shows the deviation in voltage output with increasing force at different temperatures. It is evident from this figure that the sensitivity of the sensor is very low at 10℃ and 100℃. A good working range for this specific sensor was 20℃ to 80℃. However, this range can be easily maneuvered by varying the insulation layer thickness or IL concentration.

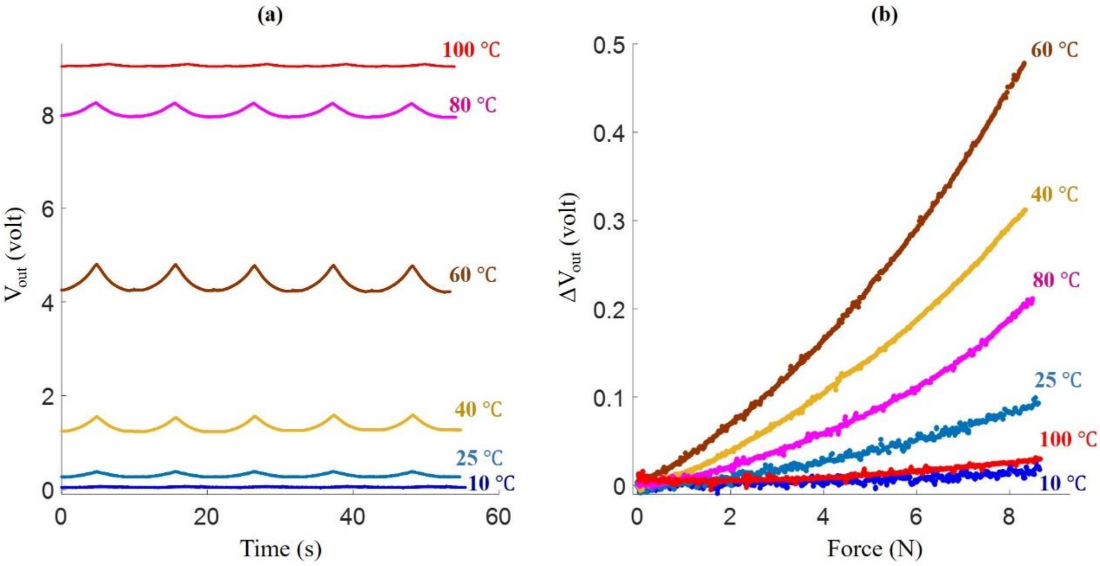

Figure 3.18. Temperature-dependent force response: (a) 9 N force was applied for 5 cycles at different temperatures; (b) voltage deviation with force at different temperatures.

3.8.4 Shelf life

A sensor was investigated for its shelf life. The sensor was fabricated with 1 wt.% IL and maintained at room temperature. Figure 3.19 shows the sensor response at different life stages. Two strain rates or probe speeds were examined. Figure 3.19(a) shows experimental results where force was applied at a probe speed of 0.1 mm/s and Figure 3.19(b) shows results for probe speed 0.5 mm/s. sensor response was recorded up to day

45 of the sensor life. As shown in the figure, the relative change in voltage for the same force went down as the sensor aged. This phenomenon was observed for both the probe speeds. However, the responses on day 30 and day 45 have very little difference between them. So, there could be a saturation of the change with age. It needs more investigation for a longer time. On the 45th day, the sensor continued to provide reliable responses.

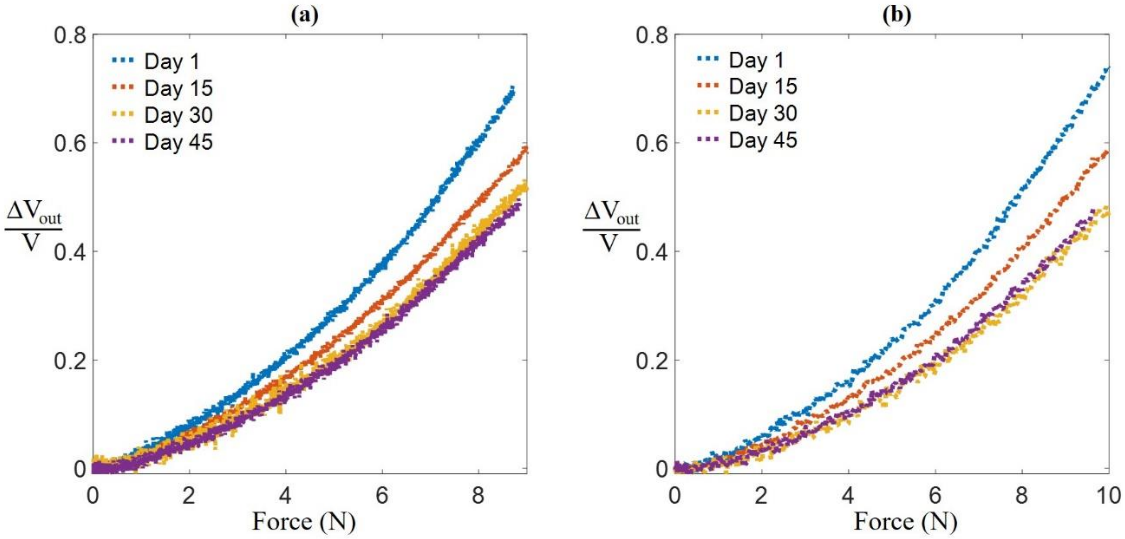

Figure 3.19. Sensor shelf life: (a) relative change in voltage output at different life stages when force was applied with 0.1 mm/s probe speed; and (b) 0.5 mm/s probe speed.

3.9 Sensor application in tire

In this work, a 3D printed tire assembly with prepared pressure sensors was demonstrated. Hybrid manufacturing techniques combining a molding and screen printing process have been used for simple and flat sensors for this work, although when the need is to fabricate a complex sensor or to have a sensor on conformal surface 3D printing is believed to be the best manufacturing process. Tires and wheels were 3D printed for the experiment. Fabricated sensors in this work were highly sensitive and when embedded in tires they give a scope to collect various information such as load, speed, force location, etc. Sensor response obtained can lead to several practical applications like road condition and tire health monitoring, movement control, obstacle avoidance, etc.

3.9.1 Tire, wheel, and chassis design and 3D printing

A tire model was designed for 3D printing having a slot in the inner surface to attach the sensor as shown in Figure 3.20(a). The outer diameter of the tire is 120 mm and the width is 62 mm. The dimension of the slot to secure the sensors was 80×50×4 mm^3. The wheel was designed accordingly. Some holes were kept on the wheel for wiring of the sensor as illustrated in Figure 3.20(b). Finally a chassis was designed having 220 mm length and 120 mm width. A shaft was designed on the chassis to attach it with the motorized linear stage. Assembly of all these models is shown in Figure 3.20. The shaft diameter was 12.7 mm. These models were fabricated in commercial 3D printers.

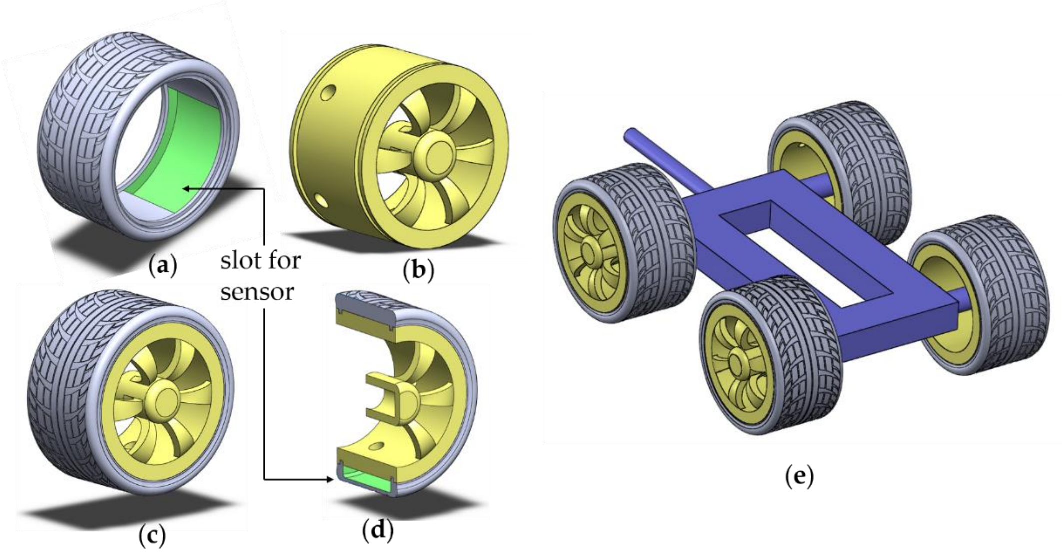

Figure 3.20. Tire assembly 3D model: (a) tire with a slot for sensor; (b) wheel with hole for wiring; (c) tire-wheel assembly; (d) sectional view of the assembly; (e) tire, wheel, and chassis assembled [68].

Four tires were 3D printed using a flexible material, TangoBlack through a polyjet printer (Objet, Eden 260 V, Stratasys). The wheels were 3D printed using a rigid material, ABSplus thermoplastic with an FDM 3D printer (uPrint SE Plus, Stratasys). The chassis was also printed using an FDM 3D printer (MakerBot Replicator). The total weight of the car assembly was 1,630 gm (four tires, four wheels, chassis, and the sensor). Figure 3.21 shows the 3D printed parts for the car.

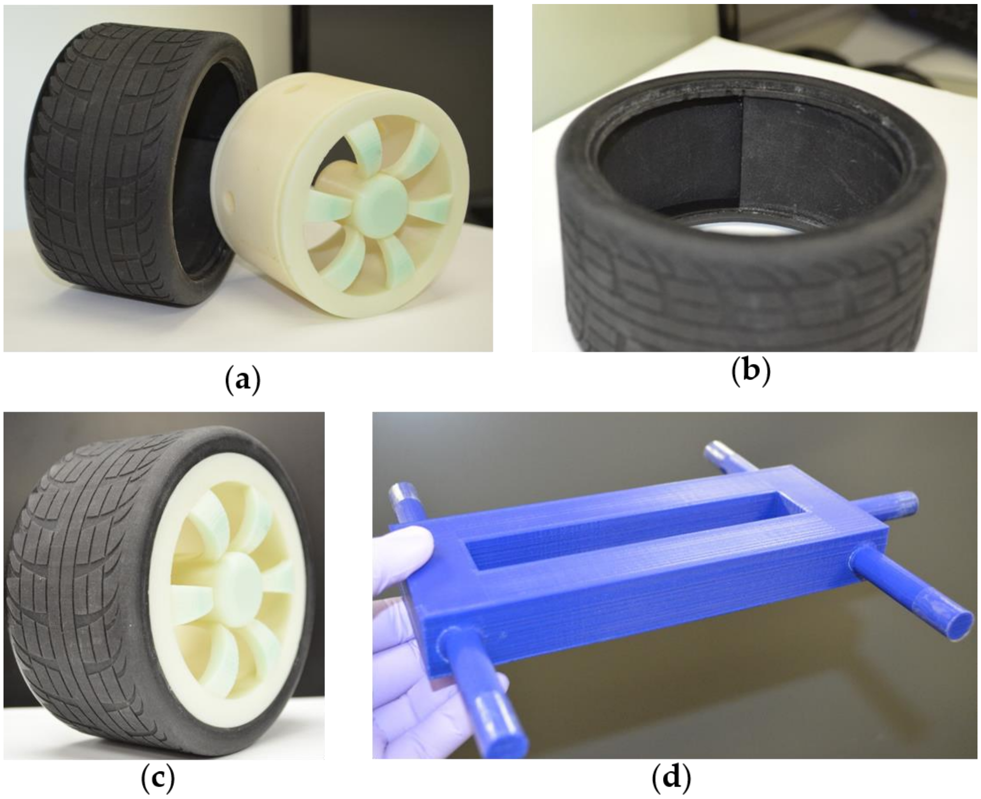
(a) (b) (c) (d)

Figure 3.21. 3D printed tire assembly: (a) 3D printed tire and wheel; (b) slot for sensor inside tire; (c) assembled tire on wheel; (d) 3D printed chassis [68].

3.9.2 Sensor fabrication and assembly

Two sensors were fabricated with six (1× 6) taxels and twelve (2× 6) taxels via molding and screen printing process as shown in section 3.5. To fabricate the IL/polymer layer 30 wt.% diluent, a photocurable monofunctional monomer (SR 278, Sartomer America, Exton, PA) was mixed with TangoPlus. Next, 3 wt.% ionic liquid ($EMIMBF_4$) was added to the mixture and blended using the high-speed mixer. Electrode material was prepared as described in section 3.4.2. The 6-taxel sensor has six electrodes in one layer and one electrode in another layer. Dome-shaped small beads were attached on the taxel. To attach the beads, TangoPlus was brushed on the sensor, then the beads were put on taxels. Finally, TangoPlus was cured by UV light. Beads were used on taxel to make the taxel more reachable and sensitive. Having the sensor inside the tire, a force from outside distributes to a larger area which makes the sensor less sensitive. This is the reason why the beads were attached to get higher pressure. Figure 3.22 shows the sensors with and without beads. Similarly, beads were added to the 12-taxel sensor, too. The thickness of the fabricated sensor was around 3 mm. Sensors can be made thinner or thicker according to applications.

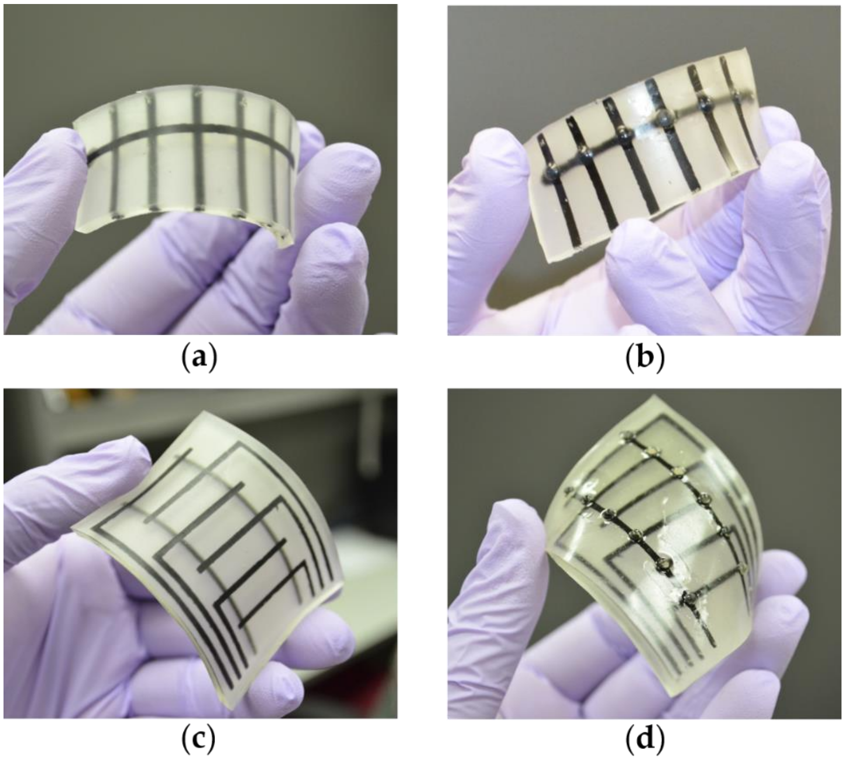

Figure 3.22. Fabricated sensors: (a) 6-taxel (1× 6) sensor; (b) 6-taxel sensor with bead; (c) 12-taxel (2× 6) sensor; (d) bead attached on each taxel [68].

Figure 3.23 illustrates the assembly for the 12-taxel sensor experiments. The sensor was wired and securely mounted on the wheel while wires from the sensor come through the hole in the wheel. Common solid core electrical wire (copper) was pierced into the sensor to connect with MWNT based electrodes. The tire was assembled with the wheel carefully so that the sensor goes to the slot inside the tire. Only one tire was equipped with the sensor. The whole car assembly was firmly connected to a high resolution motorized linear stage to control the speed of the car. Figure 3.23(c) shows the assembly and wiring of the system.

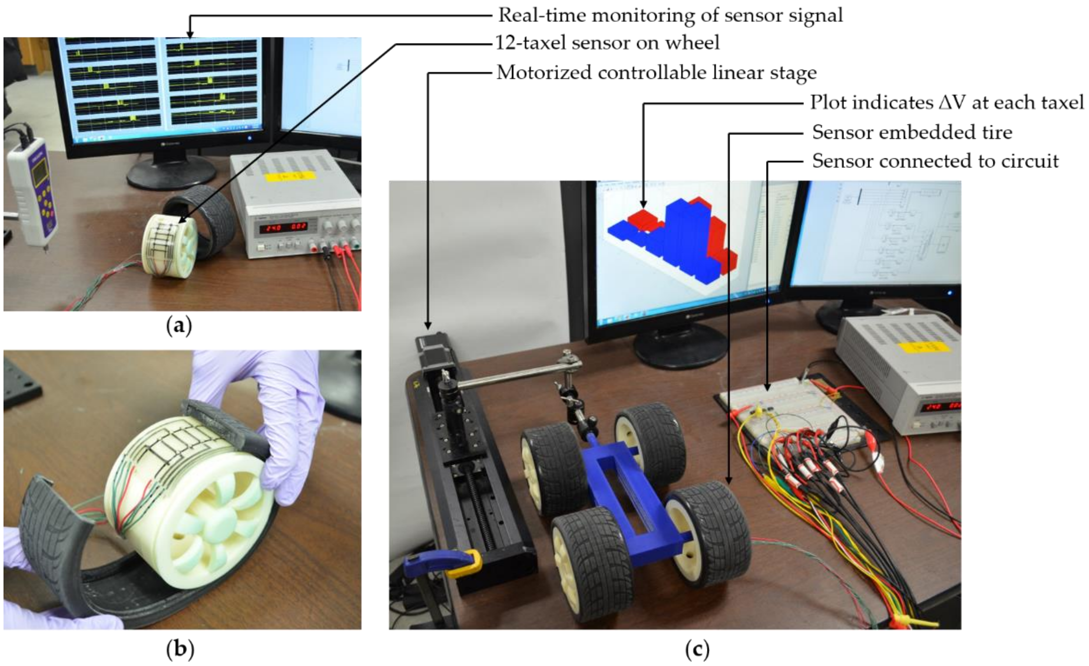

Figure 3.23. a) 12-taxel sensor attached on the wheel; (b) sensor connected and inserted inside tire; (c) fully assembled experimental set-up with motorized linear stage [68].

3.9.3 Experiments

The experimental setup was comprised of a data acquisition device (DAQ, BNC-2090A, National Instruments, Austin, TX), external power supply (E3630A, Keysight Technologies, Santa Rosa, CA), and motorized linear stage (A-LST250B-E01, Zaber Technologies, Vancouver, BC) with the resolution of 0.1 μm and a maximum travel range of 250 mm. The car chassis was connected to the linear stage firmly and the stage movement was controlled by ‘Zaber Console’ software provided by the manufacturer of the stage. The DAQ was interfaced with MATLAB/Simulink and was used to measure voltage output across the external resistor (20 MΩ) of the half Wheatstone bridge circuit. Two sensors were fabricated for this study: one with six taxels (1× 6) and the other with twelve taxels (2× 6). The 6-taxel sensor was used for different load condition experiments and a 12-taxel sensor was used for different speed condition experiments. During experiments with a sensor each taxel was connected to the half Wheatstone bridge circuit. An op-amp (OPA551PA, Burr-Brown product from Texas Instruments) was used with the DC supply voltage of 24 V for each of the input electrodes of the sensor. The wiring diagram of the twelve-taxel (2× 6) sensor is shown in Figure 3.24. The input voltage in each electrode was controlled through DAQ. A low pass Butterworth filter was used for the data received to reduce noise.

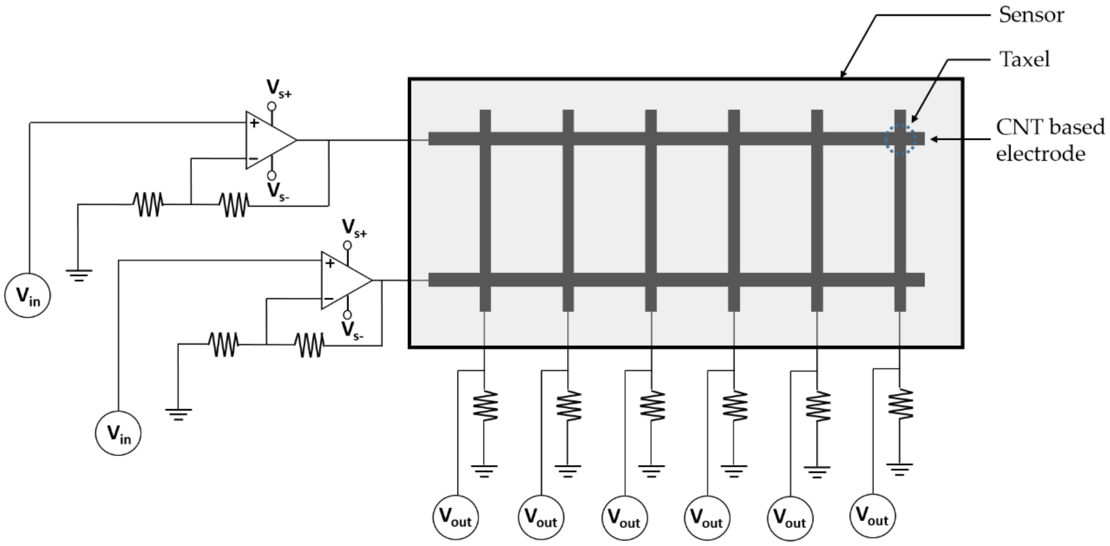

Figure 3.24. Wiring diagram of a twelve (2× 6) taxel sensor where each taxel is connected to a half Wheatstone bridge circuit. For operational amplifier (OPA551PA), supply voltage range was (+24 to -24 V), input voltage range was (+10 to -10 V) [68].

Experiments were done in two phases with two different sensors. For the first set of experiments, the 6-taxel sensor was inserted inside the tire slot and connected to the circuit. The car was driven at 5 mm/s, 10 mm/s, and 50 mm/s speeds. For each speed car chassis was loaded with 0.38 kg, 1.50 kg, and 5.00 kg weights and sensor responses were recorded. For the second set of experiments, the 12-taxel sensor was embedded in tire and the car was driven at 5 mm/s, 10 mm/s, and 50 mm/s speeds with the weight of 0.38 kg while sensor responses were recorded as voltage. Also locations of applied force were detected.

3.9.4 Different load conditions

The car was driven at 5 mm/s, 10 mm/s, and 50 mm/s speeds for this experiment. For each speed car was mounted with the loads of 0.38 kg, 1.50 kg, and 5.00 kg. Figure 3.25 illustrates a graph indicating the change in voltage output versus time to show the sensor response at different conditions. As the tire rotates, the taxels come in contact with the road one by one. Once a taxel comes down to the road, the weight of the car creates a compressive strain on the taxel which results in a decrease in sensor resistance. Thus, the voltage output increases across the external resistor of the half Wheatstone bridge circuit. Changes in voltage output are indicative of the external force applied on the sensor. As expected, Figure 3.25 shows a higher voltage increase for the higher load. The blue line on top indicates a 5 kg load and the yellow line at the bottom denotes a 0.38 kg weight. Also notable, taxels are showing responses at different times according to speed. Now comparing Figure 3.25(a), (b), and (c), it’s seen that for the same weight, voltage change varies with speed. The difference is not that significant between 5 mm/s and 10 mm/s but it’s clear between 5 mm/s and 50 mm/s or 10 mm/s and 50 mm/s. For the higher speed changes in voltage are comparatively lower which may come from the shorter time for the normal force to act on the taxel.

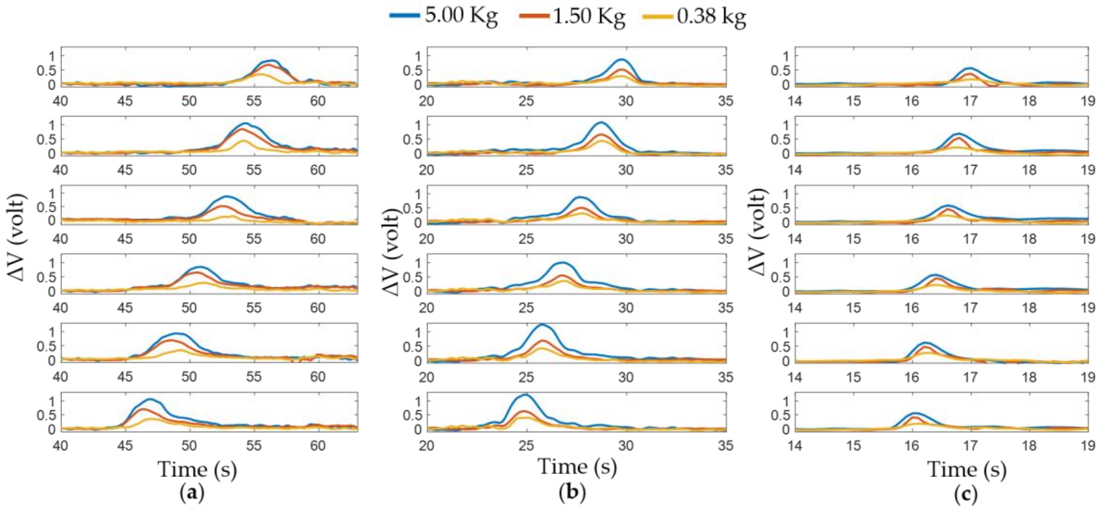

Figure 3.25. Changes in voltage output versus time for different load conditions: Voltage output with the speed of (a) 5 mm/s; (b) 10 mm/s; (c) 50 mm/s [68].

3.9.5 Location and speed

A twelve-taxel sensor was embedded in the tire. Each taxel is attached and corresponds to a unique location in the tire, as shown in Figure 3.26(a). To graphically represent these twelve locations in tire and force on each location, a bar plot was drawn. Each bar in Figure 3.26(c) indicates a certain taxel and a certain place in the tire. Once the tire rotates, the bar plot shows the voltage change in each taxel according to the force upon it. For example, Figure 3.26(c) shows ΔV at a certain time. Bar 7 and 8 show the highest peak which means locations 7 and 8 undergo weight/force at that certain point of time. Figure 3.26(b) is the corresponding tire situation when it rotates forward.

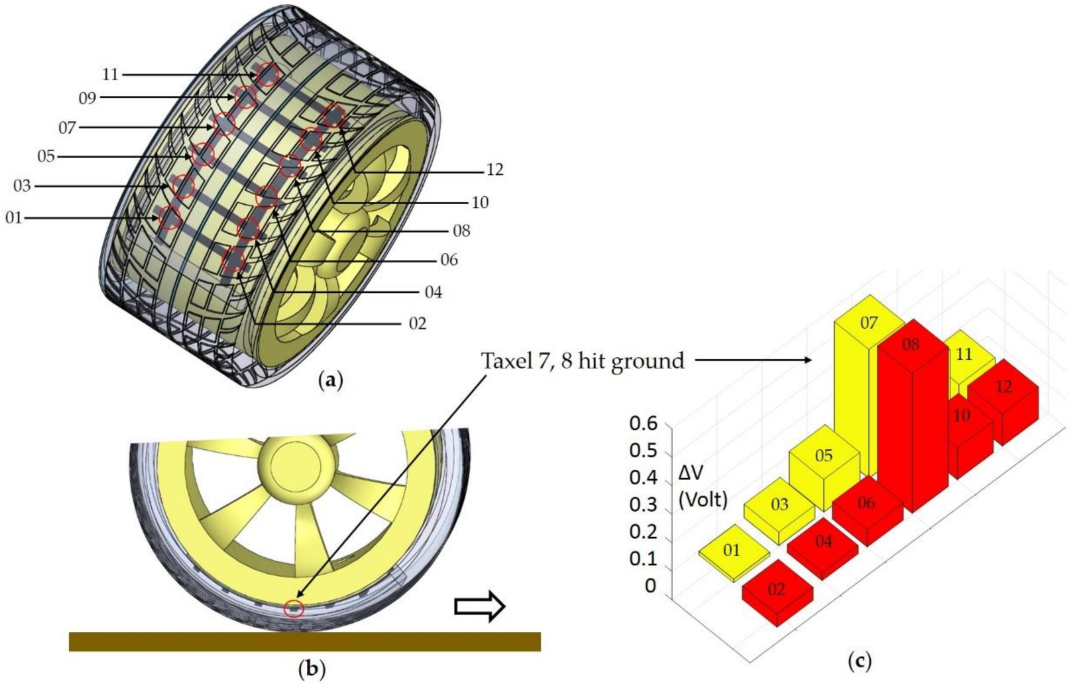

Figure 3.26. Location detection: (a) 12 locations on tire were marked corresponding to 12 taxels; (b) tire rotates while taxel or location 7, 8 hit ground; (c) bar plot indicates ΔV at each taxel when location 7, 8 hit ground [68].

The speed of the car was measured from the sensor data while the car was loaded with 0.38 kg of weight. Taxels are 9 mm away from each other in the longitudinal direction and two farthest taxels have a distance of 45 mm between each other. Figure 3.27 shows experimental results for three different speeds. From the pick of voltage change, time to hit each taxel was measured and using this time and distance between the taxels, speed was calculated. Speed can be measured at each row of taxels, from the second to the last row. With six rows of taxels, speed was calculated five times and compared with the original speed provided in the stage. The calculated speed was close to the original speed. Some deviation can happen due to friction between the chassis shaft and wheel bore. No bearings were used for these experiments and some frictional resistance was noticed between chassis shaft and wheel bore. Locations of force are also shown at a certain time in Figure 3.27(d), (e), and (f).

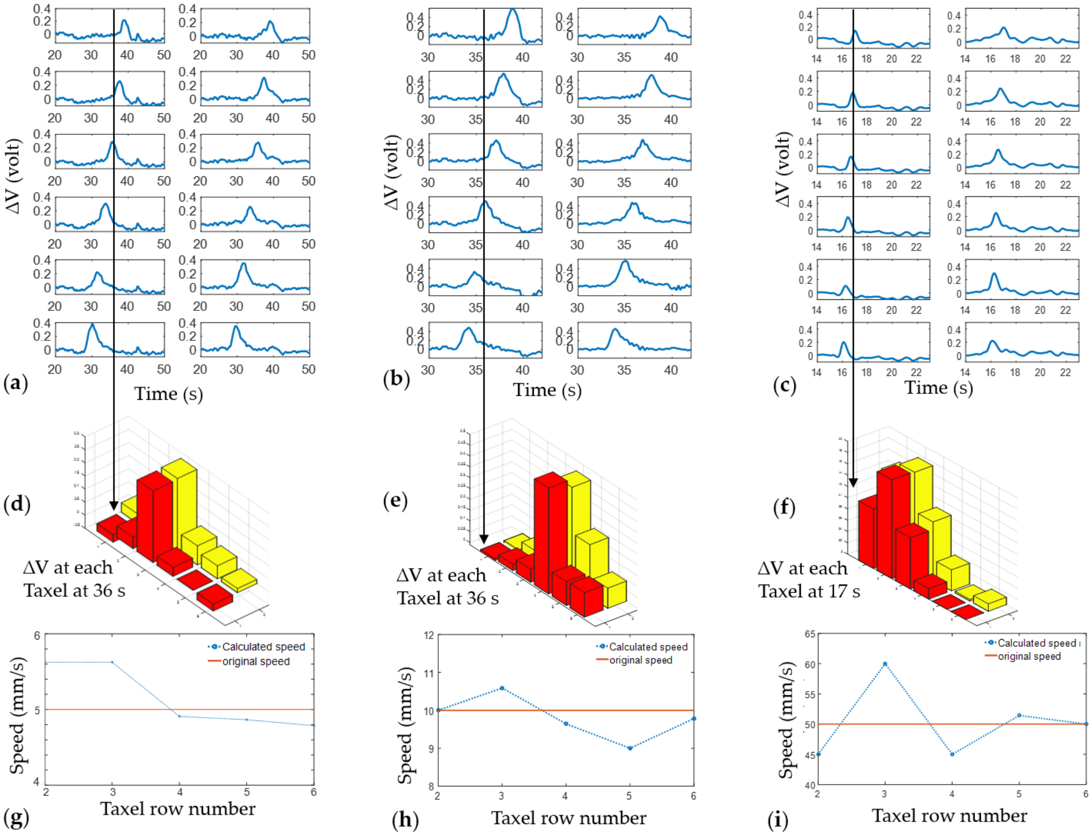

Figure 3.27. Car was loaded with 0.38 kg weight and experimented at different speeds: Change in voltage output versus time for 12-taxel sensor embedded in the tire while car speed was (a) 5 mm/s; (b) 10 mm/s; (c) 50 mm/s; (d) – (f) locations of force shown in the bar plot at a certain time; (g) - (i) speed of the car calculated at each row of taxel and compared with original speed [68].

3.9.6 Discussion

As a whole, the experimental results have shown a trend throughout the work. But there are some cases of inconsistent outcomes. In particular, the speed calculated in Figure 3.27(i) shows a big deviation from the original speed provided to the stage. There could be a few reasons behind this deviation. Because of not using any bearing, there was friction between chassis shaft and wheel bore. There were vibrations while the car was moving and the direction of the movement could also change slightly. And thus, using bearings could improve the experimental setup considerably. The electrical noise in the voltage output signal was at a reasonable level and signal peaks due to force on sensor were distinct from noise. Signal to noise ratio (SNR) of the output voltage was calculated using MATLAB function (SNR), as 37.28 dB. But in some cases, electrical noise has been noticed (such as Figure 3.27(a)). Better filtering could reduce the noise in voltage output data received through DAQ. In upcoming works improved electrical noise reduction system, as well as bearings for the car, will be used for obtaining better data. Different taxel data (voltage output) of the sensor could be a little non-uniform because of manufacturing variables and artifacts. But each taxel can be calibrated separately for a force to keep the results consistent.

To verify the effect of bending curvature on the sensor, it was tested by keeping the sensor on a flat surface and a curved wheel. There was negligible difference in signal output while normal force applied on the sensor is the dominant factor in the change of voltage output. Moreover, the sensor could be calibrated to measure force once it is mounted on the wheel so that there will be no effect of curvature. Another area of limitation was the distance traveled by the car. Because of the short-range of the stage the maximum distance the car could travel was 250 mm. Also wires from the sensor to the circuit board restricted the longer run of the car. As a result of these limitations, the tire could not rotate more than once at a single run.

In this work, flexible multi-taxel IL/polymer sensors have been demonstrated for tire applications. Material preparation and manufacturing techniques of the sensor were reported. The sensor was embedded on the inner surface of the tire for tire condition experiments. Series of experiments were accomplished to test different load and speed conditions. With the increase of weight, change in voltage output (ΔV_{out}) increases which is indicative of higher force on the tire. By analyzing each taxel data separately, the location of forces was detected as well as the speed of the car was calculated. The important information extracted from the sensor response such as load, speed, location, etc. could be valuable for many automation applications. Mobile robots and self-driving cars could be potential fields of sensor embedded tires. In the future, scopes of the experiments will be broadened with more taxels in sensors and different road conditions will be tested. In terms of manufacturing the sensor, 3D printing is the final goal, where all of the materials used for this work are 3D printable. 3D printing of sensors on the free-form tire surface is another research focus for the future. This work is the first step when the final goal includes a fully 3D printed tread sensor combination.

3.10 Sensor application in insole

An insole with the screen-printed sensors was examined for different landing patterns while walking. This is a preliminary study when the goal is to fabricate a 3D printed smart insole. Since simple, flat sensors were needed for initial investigation, they were fabricated through screen printing and molding processes. However, 3D Printing could be the most suitable manufacturing process for this stretchable multi-layer and multi-material sensor, especially when the sensor is complex shaped. While traditional manufacturing techniques fail to achieve them, 3D printing can fabricate any complex shape and provide scope for free-form fabrication and customization in design. The future plan includes 3D printing of the whole structure including the sensor. The fabricated sensor embedded in the insole was successfully tested for pressure monitoring. This study is believed to open doors for many future research with potential applications in the field of sports and medical biomechanics.

3.10.1 Sensor and insole fabrication

The sensors for this experiment were fabricated via molding and screen printing process as described in section 3.5. The intermediate layer of the sensor was fabricated using 3 wt.% IL with a prepolymer (dilute TangoPlus). Figure 3.28(a) shows the screen-printed sensor. The insole was designed with three slots open to insert sensors at heel, midfoot, and forefoot. The designed insole was 3D printed using a flexible material, TangoPlus FLX930, through a commercial polyjet 3D printer (Objet, Eden 260 V, Stratasys). Figure 3.28(c) shows a 3D printed insole. Molds for the sensor were also designed and 3D printed according to the slot size using FDM based 3D printers. Three sensors were fabricated with a 15 mm taxel diameter. The sensor thickness was 3 mm with a 1 mm thick intermediate layer. Sensors were attached to the slots using flexible glue. Figure 3.28(d) shows the sensor embedded insole where the whole structure is soft and stretchable.

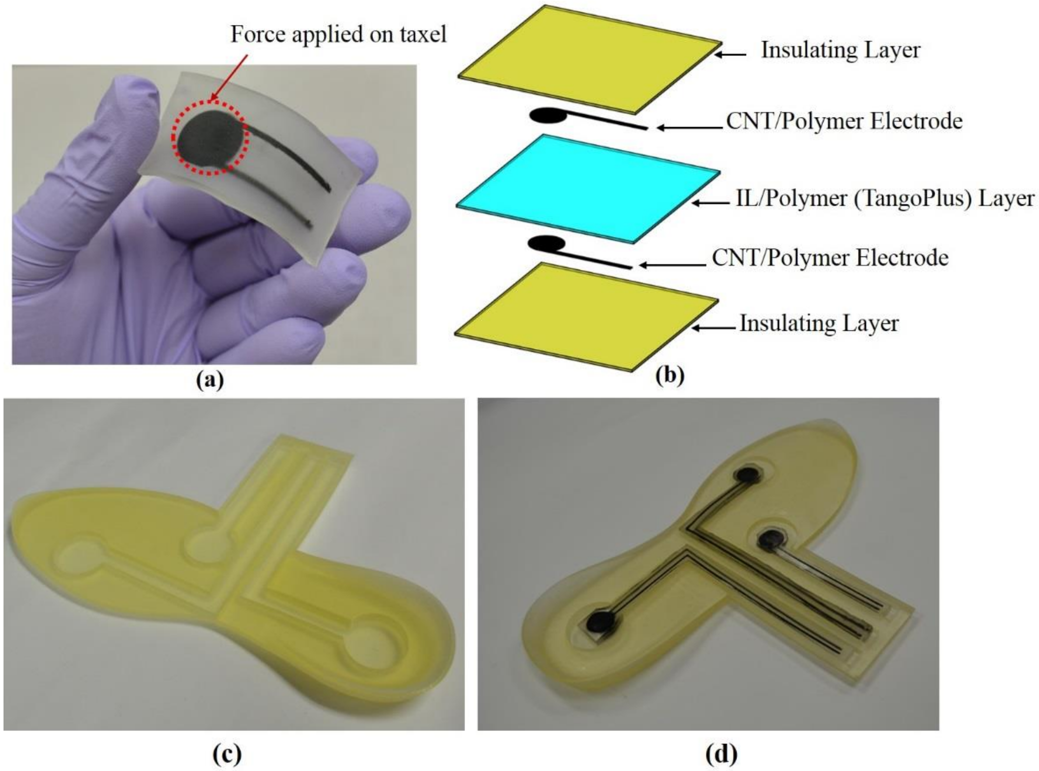

Figure 3.28. Sensor embedded insole: (a) screen printed single taxel sensor; (b) different layers of the sensor; (c) 3D printed soft insoles with slots for sensors at the heel, midfoot, and forefoot; (b) sensor attached to insole [63].

3.10.2 Experiments

The sensor-embedded insole was used with a sandal at this point. The sensors were wired and attached to the insole. Common single core electrical wire was pinned to MWCNT based electrode. Figure 3.29 shows the insole in a sandal. Using the adjustable strap, the insole was fit in the sandal and prepared for comfortable walking.

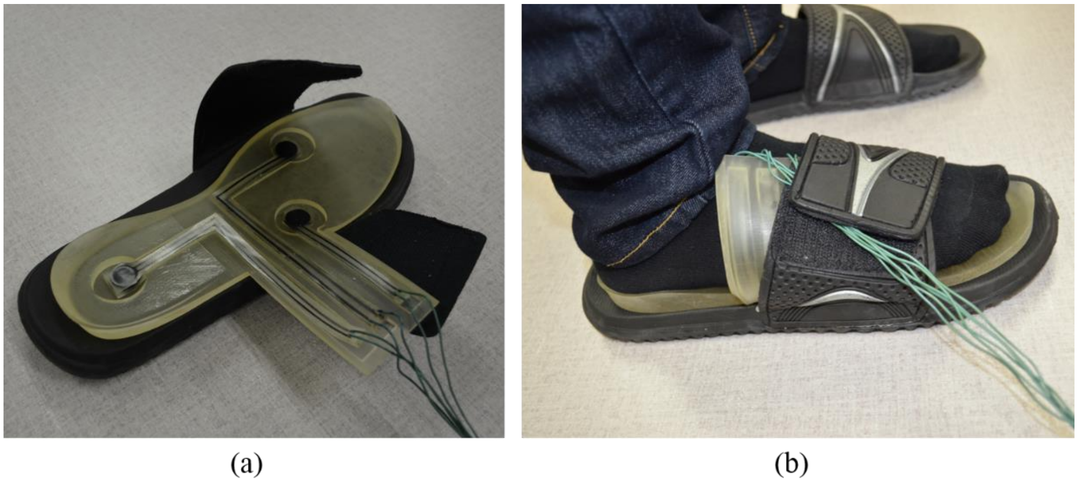

(a) (b)

Figure 3.29. Insole with the wired sensors was put in a sandal: (a) electrical wires were pierced into sensor electrodes; (b) insole in sandal before walking [63].

Each sensor was connected to a potential divider while the voltage output across the external resistor was measured using a data acquisition device (DAQ, BNC-2090A, National Instruments, Austin, TX, USA). The external resistors used have a resistance of 20 MΩ each. An input voltage of 24 Volt was provided by an external power supply (E3630A, Keysight Technologies, Santa Rosa, CA, USA). Figure 3.30(a) shows the wiring diagram of the circuit and Figure 3.30(b) shows the actual experimental set-up with fabricated sensors connected to the circuit. Three output voltage data arrays representing three different sensor responses were recorded through a MATLAB program. Signal outputs went through a low pass filter to reduce electrical noise.

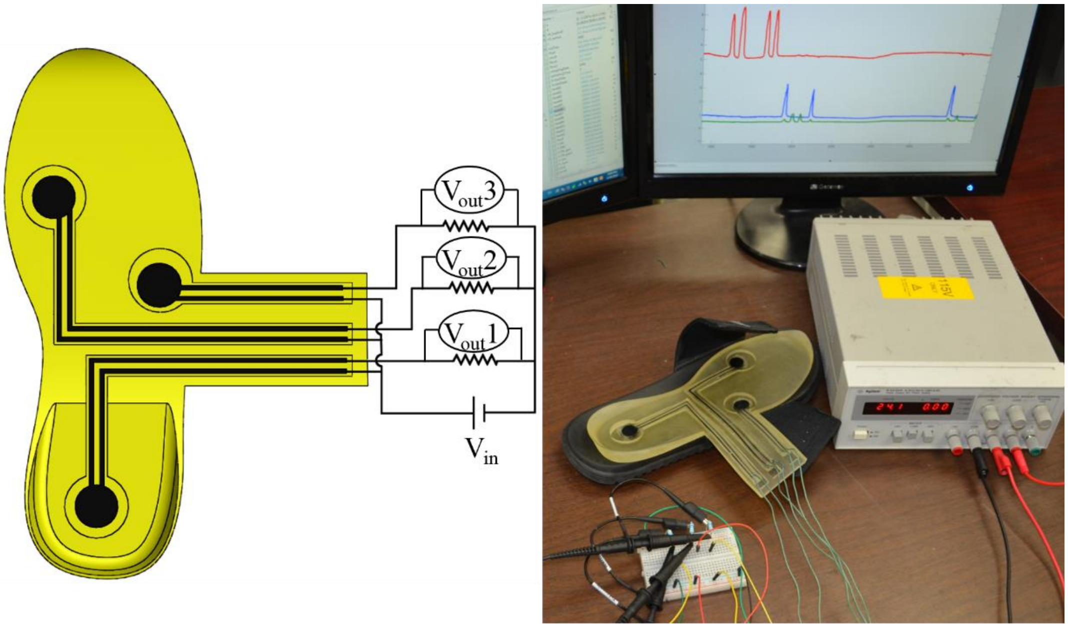

(a) (b)

Figure 3.30. Electrical connection of the sensors: (a) wiring diagram of the sensors; and (b) fabricated sensor connected to circuit [63].

A single sensor was tested first under repeated load where the actual and measured force were compared. Since the sensors in the insole were wired to circuit board and DAQ, long-distance walking or running was not possible at this point. Experiments were done with a back and forth movement. Walking was mimicked by one step forward and one step backward movement. Three different walking patterns were checked. Sensor data are evaluated for walking while heel strikes the ground first, midfoot strikes ground first, and forefoot strikes the ground first. For each experiment, the ΔV versus time curve was plotted.

3.10.3 Result and discussion

Initially, the sensor embedded insole in sandal was tested for one foot-step. A step was taken with forefoot striking the ground first. As force applied on each sensor, voltage output corresponding to that increases. ΔV is a measure of how much force applied on the sensor. Here, sensor data are not calibrated to measure force as comparison among the sensor data at different places is our objective. Figure 3.31 illustrates the result of one foot-step. The vertical line in that figure indicates the sensor signal output at the time of foot grounding. As forefoot strikes the ground first, maximum force works on the forefoot and then the foot is taken off for the second step. Because of that, ΔV at the forefoot sensor is highest, the midfoot sensor also shows a significant ΔV, and the heel sensor shows the least amount of ΔV as minimum force works on the heel. The time of different peaks in Figure 3.31 also indicates how the foot was grounded.

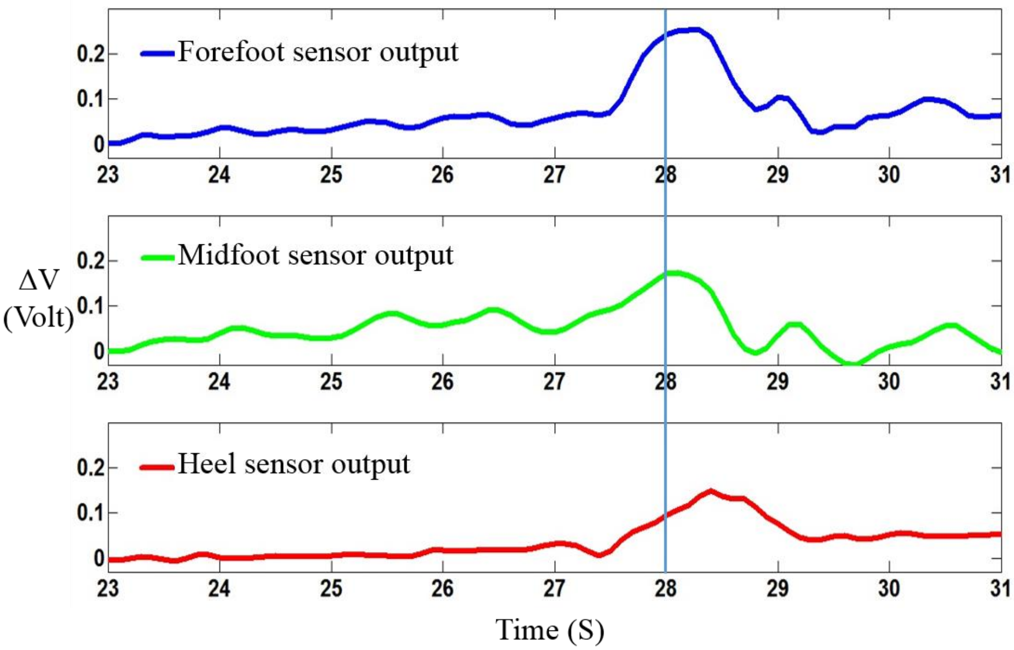

Figure 3.31. The response of sensors at heel, midfoot, and forefoot for one foot-step while forefoot strikes the ground first [63].

The next three sets of experiments were done for walking like movement. Due to wiring constraints one step forward and one step backward movement was done and data for four steps were shown. Figure 3.32(a) illustrates sensor data (ΔV vs. time) while heel strikes the ground first. In all the graphs red line indicates heel sensor response, the green line indicates midfoot sensor response, and the blue line indicates forefoot sensor response. The vertical lines in the graphs in Figure 3.32 denote the pressure situation at the time of foot landing. As the heel strikes the ground first, Figure 3.32(a) shows a clean spike for the heel sensor while other sensors show a significantly lower change in voltage. Figure 3.32(b) shows midfoot striking data. As expected, the midfoot sensor shows the maximum ΔV which means force was largely exerted on the midfoot. Here, the forefoot sensor also shows a significant change in voltage. Because of midfoot and forefoot sensors' positions being close to each other a good amount of force was applied on forefoot too. Also when landing on midfoot, it's difficult to avoid giving force on the forefoot. Figure 3.32(c) is a graph plotted for forefoot striking experience. Forefoot sensor data shows clean peaks when the other two do not show any significant change. For both midfoot and forefoot striking, the heel sensor goes under very little force. So, these figures can clearly differentiate which place the runner is landing on his /her insole as well as the time of striking.

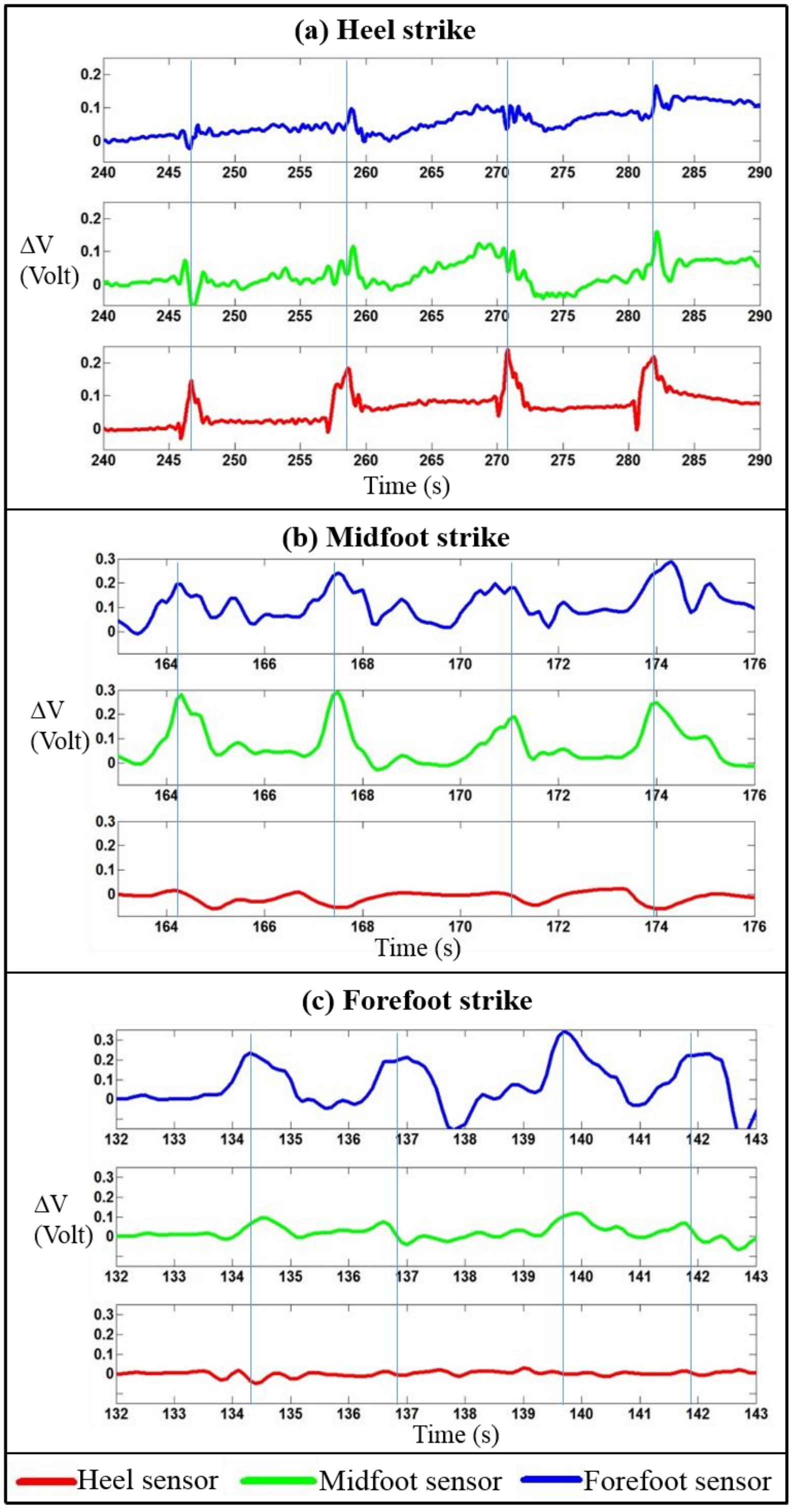

Figure 3.32. Sensor embedded insole: (a) screen printed single taxel sensor; (b) different layers of the sensor; (c) 3D printed soft insoles with slots for sensors at the heel, midfoot, and forefoot [63].

Some of the figures contain electrical noise from signal output data. Figure 3.32(a) carries substantial noise. As the connection between the CNT based electrodes and electrical wires is not well-secured, there is some disturbance at the time of walking. Also while walking all the wires move with foot which also may create noise. ΔV is not equal for all the steps and the shapes of the spikes are also not alike. This is because the landing conditions are not the same all the time. Some of the spikes are two-phased or blunt, especially for midfoot and forefoot sensors. Because of the bigger area, the pressure is low on midfoot. Also, there could be some slip while landing. These may contribute to the bluntness of the peaks. There are some cases of negative ΔV, which may come from tension or pull on the sensor. While landing force on the sensor is compressive. But at takeoff there could also be little pull on the sensor which affects the signal output.

Foot plantar pressure monitoring is very important in athletics/sports biomechanics. Information received real-time from insole can improve performance as well as lower the chance of injury. In this work, an insole was 3D printed and screen printed pressure sensors were attached to the insole at heel, midfoot, and forefoot position. The whole structure was soft rubberlike. Data were analyzed for different foot grounding patterns. The final goal is to develop a fully 3D printed multi-taxel insole-sensor incorporated with a wireless circuit board. This would open avenues for a wide range of applications.

3.11 Limitations of screen printing and molding

The screen printing and molding process is suitable for simple geometry. However, it comes short for complex geometry. Also, it is difficult to customize and modify the design of the sensor in screen printing. In some cases it might not be possible to realize a sensor design through screen printing and molding. For example, a sensor on a free-form surface (as shown in Figure 3.33) is not achievable via this process. The molding process only works for material with low viscosity. Therefore, material for screen printing and molding has a limited selection. 3D printing overcomes the limitations of the screen printing and molding process. Moreover, 3D printing will provide more control over the fabrication process.

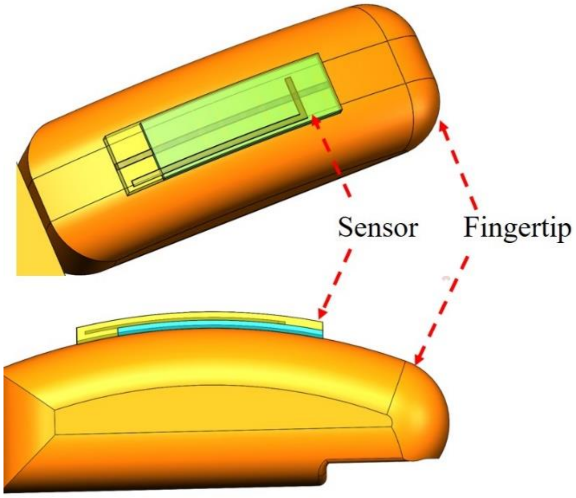

Figure 3.33. Sensor on a free-form surface (fingertip).

CHAPTER IV

3D PRINTING OF SENSORS

4.1 Introduction

3D printing provides superior design and manufacturing freedom. It is easier to realize any customization, modification, and geometric complexity through 3D printing. 3D printing of the soft pressure sensor opens up many new applications involving free-form fabrication. Conventional fabrication processes often fail when the printing substrate includes complex geometry [124]. Moreover, 3D printing provides more control over manufacturing by offering many controllable parameters and a wide selection of materials for fabrication.

Different 3D printing technologies, such as thermoplastic extrusion [125], stereolithography [126], material or binder jetting [127], and powder bed fusion [128] support fabrication using a broad selection of materials. Recent developments in additive manufacturing have enabled the 3D printing of soft electronics with functional materials [129]. Extrusion-based direct-print (also referred to as *direct-write*) is a suitable technique to use for 3D printing functional materials [130], [131]. Thermosetting prepolymers are commonly functionalized and modified for printing in cases where heat or light are used for subsequent polymerization, and viscoelastic elastomers could be used for printing in cases where there is a need to build flexible and stretchable parts. Despite the work conducted in the area of 3D printing of functional materials, there is still a need for additional work in order to achieve a printing process that uses multiple materials in a single print, to facilitate the introduction of ILs for functionalizing, and to optimize soft/stretchable polymers for printing.

The objective is to develop a multi-material direct-print system to 3D print a soft pressure sensor. A prepolymer paste will be used in the system for a layer-by-layer extrusion-based printing. Next, the 3D printed prepolymer part will be polymerized through a combination of photo and thermal curing processes. For the pressure-sensitive layer, ILs are mixed with a prepolymer to induce pressure sensitivity. The inclusion of IL into the sensor gives more flexibility in controlling sensor performance. By varying the IL ratio, the sensitivity of the sensor can be adjusted to achieve different dynamic ranges. The sensor design and geometry can also be varied to modulate the sensing performance. The multi-material direct-print system will provide a solution to tailor material compositions and geometry for the development of a subject/application-specific sensor.

4.2 Multi-material direct printing system

A multi-material extrusion-based direct-print (DP) system was developed to 3D print the soft pressure sensor. Since the sensor is composed of three different materials, a printing system was developed with three extrusion heads capable of printing three different materials in a single print. A high- precision motorized XYZ linear stage system (PRO115, Aerotech Inc., Pittsburgh, Pa., USA) was used for the movement of the axis, as shown in Figure 4.1. Three extruders/syringes with three XR25C/M manual translation stages (Thorlabs Inc., Newton, N.J., USA) were installed on the Z-stage to enable fine adjustment during the extruder calibration. Each extruder was connected to an air-based Ultimus I pressure controller (Nordson EFD, East Providence, R.I., USA); the pressure controllers were interfaced with *LabVIEW*, where the stage movement and material dispensing processes were coordinated using G-code instructions in the Aerotech software environment. Extrusion nozzles with sizes ranging from 50 μm to 1 mm can be attached to the syringe to obtain prints with different resolutions.

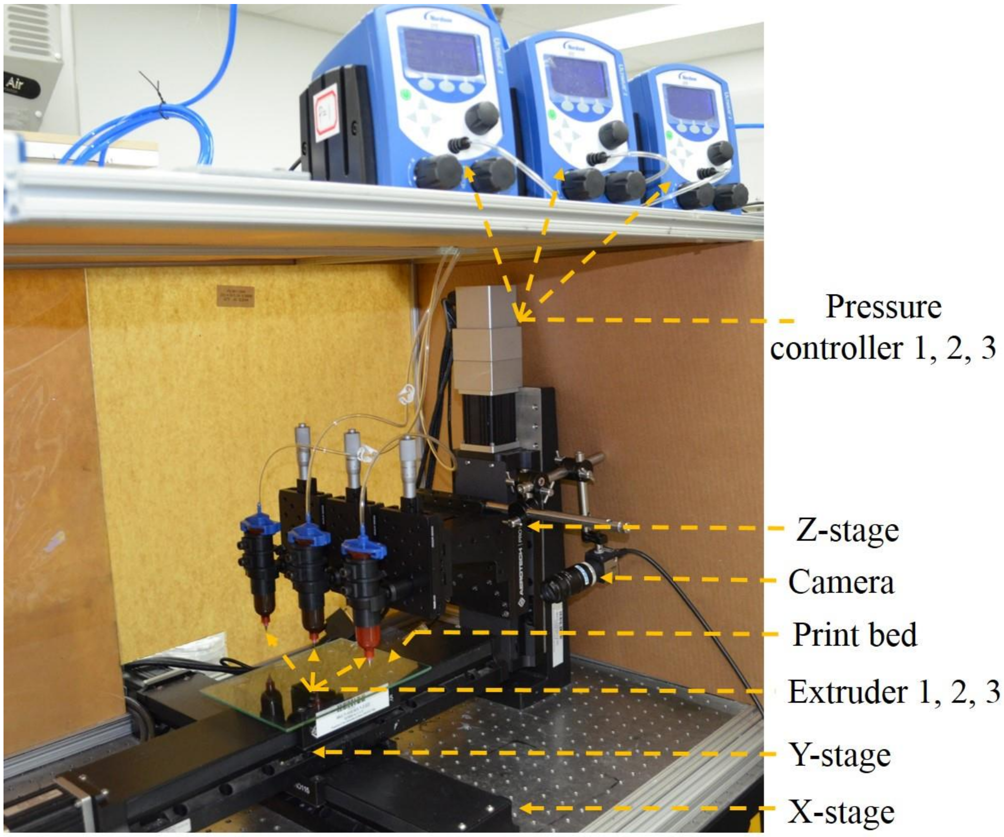

Figure 4.1. Multi-material direct-print (DP) system [132].

4.3 Material modification and printing parameters

The base material used to fabricate the sensor is the photopolymer TangoPlus FLX930 (Stratasys, Eden Prairie, Minn., USA), which has been utilized in commercial multi-jet 3D printers. Once TangoPlus is polymerized through the use of ultra-violet (UV) light, it creates a flexible and stretchable film. However, for the extrusion-based direct-print system proposed in this study, TangoPlus was modified to obtain the desired shear thinning property. Figure 4.2 shows TangoPlus before and after modification with 10 wt.% CAB-O-SIL® M5 fumed silica (Cabot Corporation, Billerica, Mass., USA) that has a higher viscosity [49]. To achieve the modification, fumed silica was mixed with TangoPlus using a DAC 150.1 FVZ-K high-speed mixer (FlackTek, Inc., Landrum, S.C., USA) at 2500 rpm for five minutes. Figure 4.2(c) demonstrates the extrusion of modified TangoPlus through the printing nozzle, where the modified prepolymer has a shear thinning property that enables it to hold the filament shape following extrusion. The modified TangoPlus was used for both the top and bottom insulation layers of the sensor. For the pressure-sensitive intermediate layer, an ionic liquid, 1-ethyl-3-methylimidazolium tetrafluoroborate (EMIBF4; obtained from Sigma-Aldrich) was mixed with TangoPlus in the high-speed mixer, where IL ratio was 4 wt.% [10]. Again, in order to achieve the proper viscosity and shear thinning, 10 wt.% fumed silica was added to the IL/prepolymer blend.

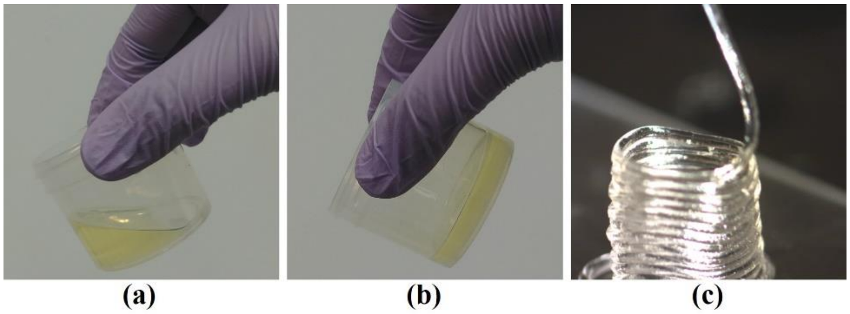
(a) (b) (c)

Figure 4.2. The photopolymer TangoPlus (a) before modification and (b) mixed with 10 wt.% fumed silica; (c) TangoPlus with 10 wt.% fumed silica when extruded through a printer nozzle [132].

The conductive electrode material was prepared by dispersing 5 wt.% MWCNTs (having a length of 5–20 μm, a diameter of 10–30 nm, and a purity greater than 85%) into TangoPlus. This was accomplished by first dissolving Triton X100 surfactant (Sigma-Aldrich, Milwaukee, Wisc., USA) into dimethylformamide (DMF; Sigma-Aldrich) before adding MWCNTs to the solution; a ratio of 1.0:3.5 MWCNTs to Triton X100 was used. The solution was sonicated using a Qsonica Q700 sonicator (Newtown, Ct., USA) to obtain global dispersion. Following sonication, TangoPlus was added to the DMF/MWCNT solution, which was mixed using a VWR 10×10-in. (25.4×25.4-cm) aluminum hot plate magnetic stirrer (VWR, Chicago, Ill., USA). After evaporation of the solvent, the paste was mixed again using a high-speed mixer at 2500 rpm. In order to induce the material to become thermally curable, 2 wt.% of a thermal initiator (Trigonox 125-C75, AkzoNobel Functional Chemicals LLC, Chicago, Ill., USA) was added to the paste to facilitate screen printing of the MWCNT/prepolymer electrode [10]; however, when used for 3D printing/direct-print, the use of this paste resulted in inconsistent printing. The addition of fumed silica to the paste improved its performance for 3D printing. As can be noticed from

Figure 4.3(a), using a CNT/prepolymer without fumed silica for 3D printing results in inconsistent line widths and printed lines that are unable to retain their shape.

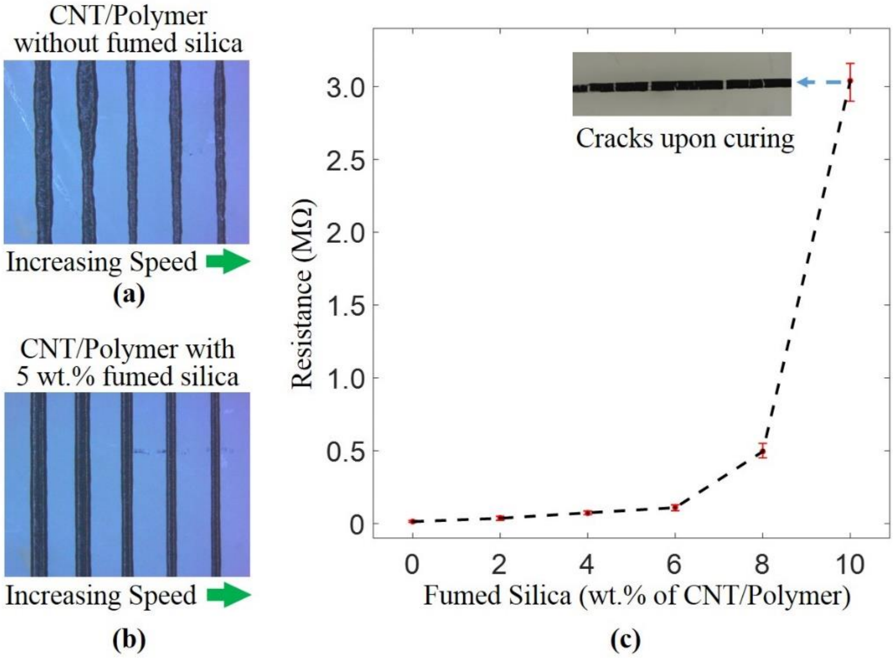

Figure 4.3. Lines that were 3D printed using (a) CNT/prepolymer material without fumed silica for 7, 10, 15, 18, and 20 mm/s travel speeds for the extruder; and (b) CNT/prepolymer material with 5 wt.% fumed silica, printed with similar travel speeds. (c) electrical resistance for CNT/polymer lines vs. wt.% of fumed silica used in the CNT/polymer material [132].

Although the addition of fumed silica improved the printability of the electrode, it degraded the electrical conductivity of the CNT/polymer electrode material. To investigate the effect of fumed silica on electrical conductivity, CNT/polymer lines (1 mm × 40 mm) were screen-printed with different wt.% of fumed silica. From Figure 4.3(c), it can be noticed that the incorporation of fumed silica increased the resistance of the CNT/polymer line, which is an undesirable outcome. Moreover, beyond 8 wt.% of fumed silica, the printed CNT/polymer line was noticed to crack upon curing. The use of 4 to 5 wt.% fumed silica in the CNT/polymer yielded a material with reasonable conductivity that was able to produce a consistent print, as shown in Figure 4.3(b). Thus, 5 wt.% fumed silica was added to the CNT/prepolymer composite used for printing the electrodes in the stretchable sensor developed in this study.

4.4 Planar 3D printing

Generally, 3D printing processes implement a planar printing where each layer is printed in one horizontal plane. In other words, for a single layer, material extrusion or print-head movement is limited to XY (horizontal) plane only. The Z (vertical) movement occurs to go to the next layer. For planar 3D printing, material extrusion or movement does not occur in XYZ direction simultaneously. Planar 3D printing is sufficient for most geometries, especially, when the print substrate is flat. However, when the need is to print on a curved or a free-form substrate, planar 3D printing has some drawbacks that will be discussed in section 4.5. In this section, a planar 3D printing of the sensor is reported. Figure 4.4 shows the schematic of a single taxel sensor. The sensor shown here is a flat. Therefore, planar 3D printing is sufficient to 3D the sensor.

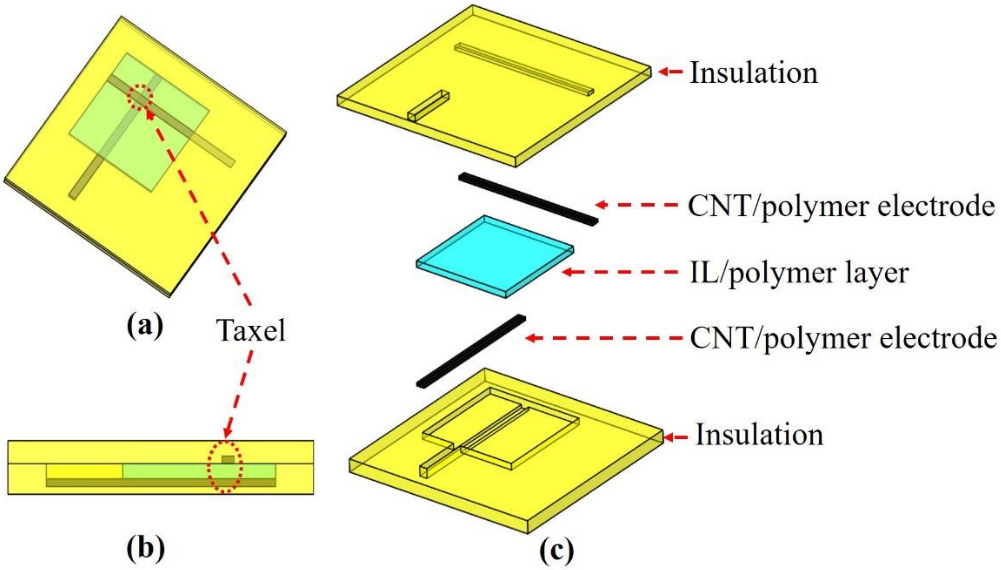

Figure 4.4. Design of a single taxel sensor for planar 3D printing: (a) 3D model of the sensor; (b) schematic diagram showing a side view of the sensor; (c) exploded view of the sensor showing the individual layers.

4.4.1 Printing of multi-material 3D structure

To demonstrate the capability of multi-material printing, several 3D structures were printed that involve the use of three extruders in each print. The 3D models were first designed as separate parts for each material in *SolidWorks*. Next, the 3D models were imported into a G-code generator software (*Repetier-Host* and *Slic3r*) to create the tool movement and extrusion instructions for 3D printing. The printing material used for the 3D structures was TangoPlus photopolymer with 10 wt.% fumed silica, and a different color dye was added to the photopolymer for materials loaded into each extruder to distinguish the output from the three extruders. The nozzles/tips used for all three extruders had an inner diameter of 335 μm, and the layer height was set at 300 μm with 100% infill for printing. The travel speed was set at 15 mm/s with a dispensing pressure of approximately 16 psi. Figure 4.5 shows three 3D parts that were printed with three materials, where each model was built in a single print that involved all three extruders in the printing process.

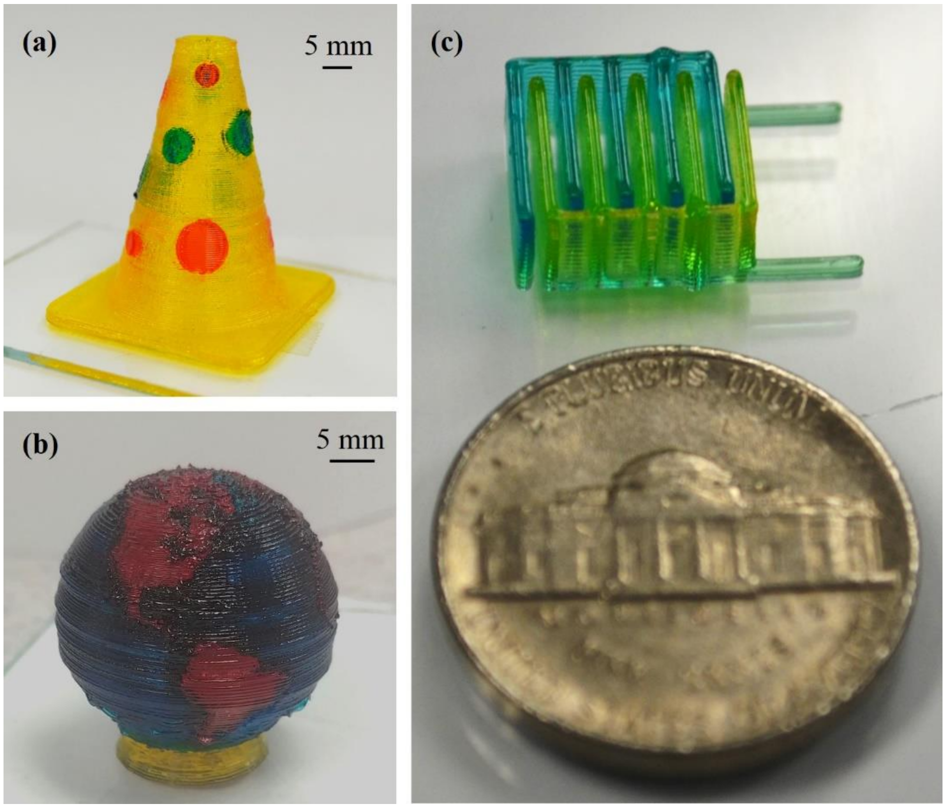

Figure 4.5. Examples of 3D structures printed with three materials using the multi-material direct-print system [132].

4.4.2 Flat sensor printing

For any 3D printing project, several parameters such as nozzle diameter, layer height, travel speed, dispensing pressure, and material composition are involved, and each of these parameters can be varied to adjust the geometry of the printed line. To uniformly print a stretchable sensor, the print parameters must be adjusted for each material used in building the sensor to obtain a constant line width throughout the printing process. In this study, an experiment was conducted to determine the appropriate parameters to use for the three printing materials by varying the dispensing pressure while keeping all other parameters fixed. A nozzle/tip with a 335-μm inner diameter was used, the layer height was set at 335 μm, and the travel speed was set at 15 mm/s. Next, lines were printed using different pressures for each material. The line width of the printed lines increased with the increase of pressure, as evident from the images shown in Figure 4.6(a). The graph in Figure 4.6(b) shows the relationship between line width and pressure for prints made using CNT/prepolymer without fumed silica (FS), CNT/prepolymer with 5wt.% FS, IL/TangoPlus with 10 wt.% FS, and TangoPlus with 10 wt.% FS. In order to obtain line widths of 335 μm for CNT/prepolymer with FS, IL/TangoPlus with FS, and TangoPlus with FS, the pressures were calculated from the graph to obtain values of 9.1 psi, 15.3 psi, and 16.2 psi, respectively. For the 3D printing process used to print the stretchable sensor, the pressures for the three materials were set around these values so that the linewidths for different materials could be maintained fairly close.

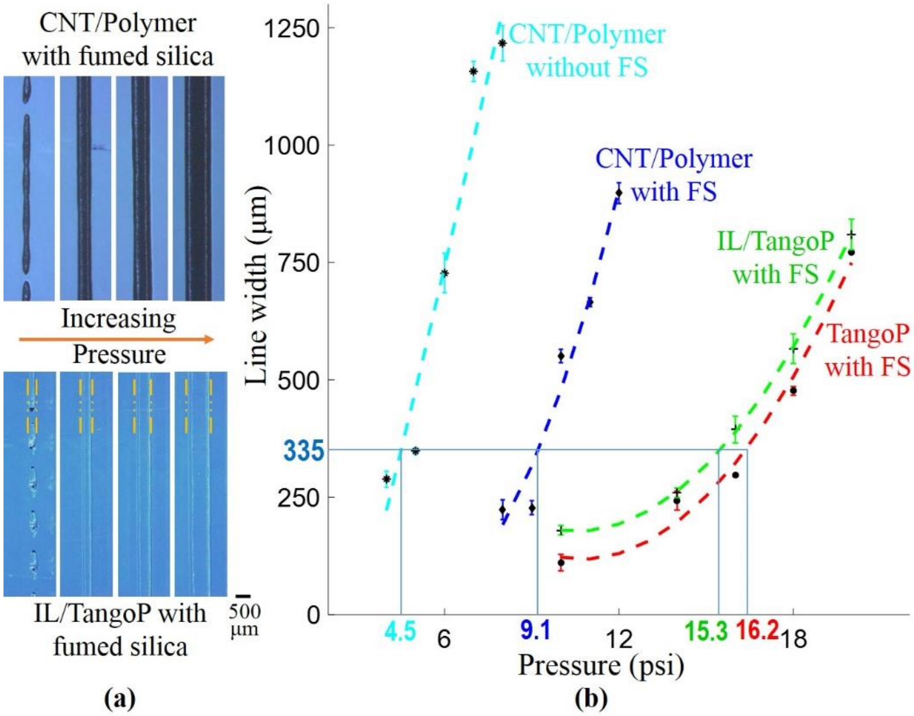

Figure 4.6. (a) Microscope image of lines printed with CNT/prepolymer with fumed silica (FS) and those printed with IL/TangoPlus with FS for increasing pressure; (b) line width vs. pressure for different materials, where all other printing parameters were fixed [132].

Figure 4.7 shows the process for printing the stretchable sensor. Syringes 1, 2, and 3 were loaded with IL/TangoPlus, TangoPlus, and CNT/prepolymer (all modified with FS), respectively. Figure 4.7(a) shows the bottom layer being printed with TangoPlus using Syringe 2, while Figure 4.7(b) and (c) show the intermediate layer and CNT/prepolymer electrode being printed using Syringe 1 and Syringe 3, respectively. A constant tip diameter (335 μm), layer height (335 μm), and travel speed (15 mm/s) were maintained for all three extruders/materials, while the pressure was varied for each material to achieve a constant linewidth. A 30-mm × 30-mm single-taxel sensor was 3D printed with a height of 2.7 mm. The CNT/polymer electrodes were 20 mm × 1.5 mm, which created a 1.5 mm × 1.5 mm taxel. The CNT-based electrodes consisted of one print-layer with a height of 335 μm when the IL-based intermediate layer consisted of three print-layers resulting in a height of around 1 mm. Figure 4.7(d) shows the 3D printed sensor before curing, fabricated using the multi-material direct-print system. The printed prepolymer part was primarily cured using a UV light curing system (OmniCure® S2000, Excelitas Technologies Co., Wheeling, IL). As the CNT/prepolymer is not photocurable because of its black color, the sensor was also maintained at 100℃ for 10 minutes to cure the CNT-based electrodes thermally. Figure 4.7(e) and (f) show the flexible and stretchable sensor after curing. A 4-taxel (2×2) sensor was also 3D printed, as will be described in the following section.

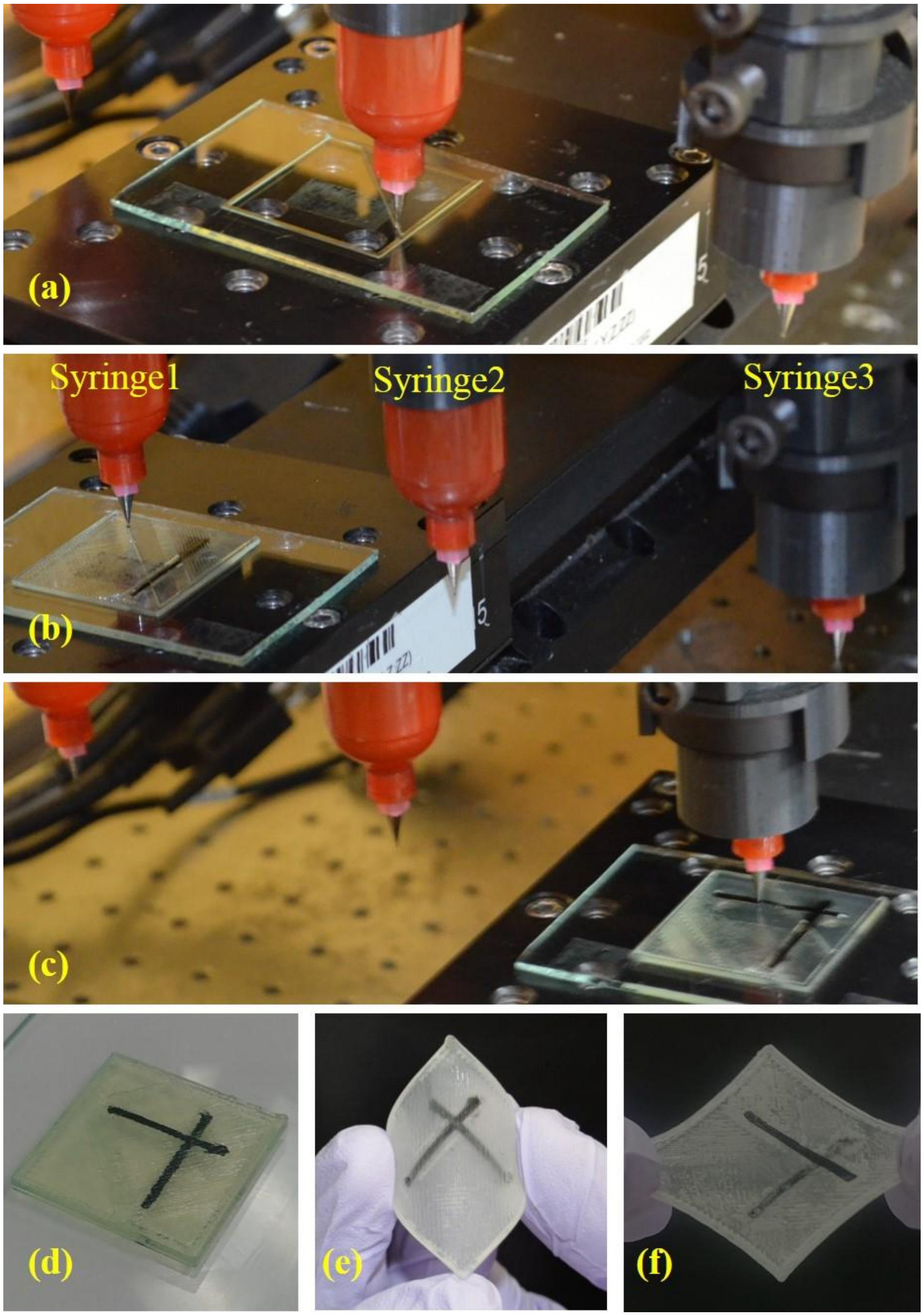

Figure 4.7. Multi-material direct-print process for a single-taxel sensor: (a) bottom layer printed using modified TangoPlus; (b) intermediate layer printed using modified IL/TangoPlus; (c) conductive electrode printing using modified CNT/prepolymer; (d) printed sensor before curing; (e–f) Cured flexible and stretchable sensor [132].

4.4.3 Planar printed sensor evaluation

To verify the mechanical characteristics of the stretchable sensor, a dog bone–shaped sensor was 3D printed according to the dimensions given in ASTM D638 for a Type V tensile test specimen, as shown in Figure 4.8(a). An Instron 5582 (Instron, Norwood, MA) universal testing machine was used for a tension test and a compression test at crosshead speeds of 100 mm/min and 1 mm/min, respectively. Figure 4.8(b) and (c) show the behavior of the sensor under tension and compression, respectively.

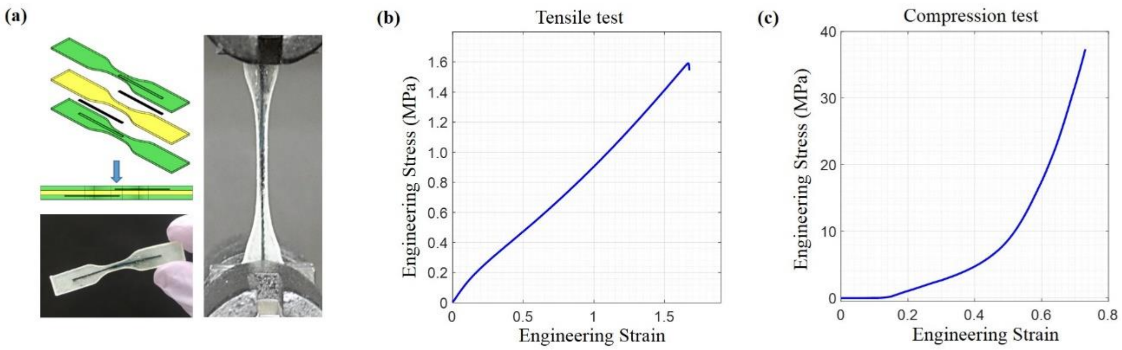

Figure 4.8. Mechanical characteristics of the sensor: (a) dog-bone shaped 3D printed sensor specimen used for the tensile test; (b) tensile test of the printed sensor; (c) compression test with the printed sensor [132].

Next, the printed single-taxel sensor described in section 4.4.2 was evaluated under different compressive forces. A probe having a diameter of 3 mm was attached to the force gauge to apply force on the taxel. First, the sensor was subjected to a fixed strain of 38% for multiple cycles at a probe speed of 0.5 mm/s. Figure 4.9(a) shows the applied force and the change in voltage output (ΔV_{out}) of the sensor system that were recorded at the same timestamp. As can be noticed from this figure, while the loading curves for force and ΔV_{out} are similar, a difference in the unloading curve can be observed. This difference in unloading may occur due to the viscoelastic properties of the soft sensor, which will be discussed in section 4.7 (Discussion). Also, the time delay between the applied force and ΔV_{out} is less than ten milliseconds.

Figure 4.9(b) shows the result from an additional experiment, where a strain at a certain level was maintained on the sensor over some time. In the top graph of Figure 4.9(b), ΔL indicates the probe/stage displacement from the point of contact with the sensor. This figure shows multiple loops where a 1-mm probe displacement was applied on the sensor for 20 s, and the applied force and ΔV_{out} are also shown for the same timestamp. The force does not remain constant over time because of the stress relaxation in the viscoelastic TangoPlus elastomer, where the sensor output ΔV_{out} is driven by the strain in the sensor.

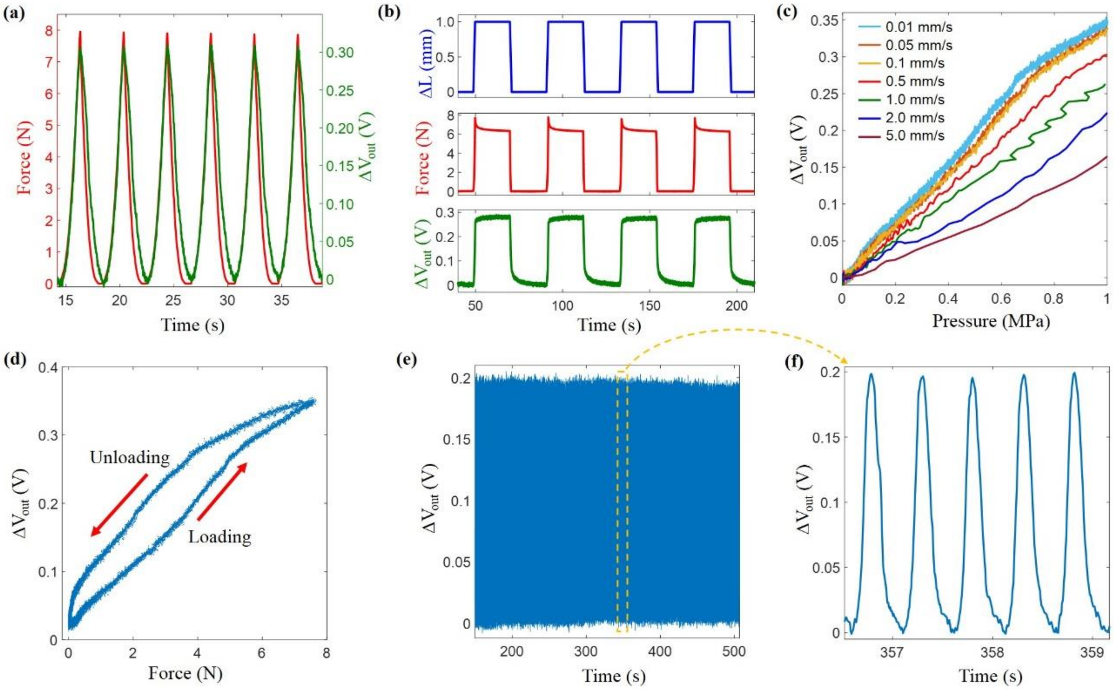

Figure 4.9. Flat sensor evaluation: (a) applied force and sensor output (ΔVout) for a fixed strain loop; (b) probe displacement (ΔL) from the point of contact (in blue), force (in red), and ΔVout (in green) at the same timestamp; (c) ΔVout vs. pressure for different probe speeds, showing the strain rate dependence; and (d) hysteresis curve for 10 loops. (e) Sensor subjected to 1,000 pressing cycles of a constant strain and (f) a subset of (e) that shows several cycles with a consistent output [132].

The strain rate/deformation rate–dependence of the sensor response is shown in Figure 4.9(c). Compressive forces were applied on the sensor at different probe speeds, and ΔV_{out} vs. pressure curves were constructed. The viscoelastic polymers show a strain rate–dependent stress-strain characteristics [133]. For the same stress, a lower deformation rate requires a higher strain. As a result, a lower probe speed results in a higher ΔV_{out}, as illustrated in Figure 4.9(c). The difference between loading and unloading behavior can be seen in Figure 4.9(d), which presents a hysteresis curve for 10 loops. A 35% strain was applied on the sensor at a probe speed of 0.1 mm/s. The sensor also exhibited consistent responses when it was subjected to more than 1,000 pressing cycles. Figure 4.9(e) shows a segment of the sensor response when the sensor was under a 38% strain cycle at a probe speed of 5 mm/s for more than 1,000 cycles. Figure 4.9(f) shows a portion of the response in Figure 4.9(e) and illustrates the consistency of the sensor output over time.

When there is a need for pressure profiling of a larger area and/or a need to locate the point of pressure application, a multi-taxel sensor could be employed, and the configuration of the electrode arrays in the sensor could be customized in order to generate a different number and density of taxels. To verify that the proposed sensor could also be 3D printed with multiple taxels, a 4-taxel (2×2) sensor was 3D printed via the multi-material direct-print system, as shown in Figure 4.10(a). The sensor was connected to external circuitry so that data could be collected from all four taxels simultaneously. Force was applied manually on one taxel, as shown in Figure 4.10(b), and the resulting sensor response in all the taxels in terms of ΔV_{out} is shown in Figure 4.10(c). The taxel that underwent deformation showed a peak in ΔV_{out} at the time of force application.

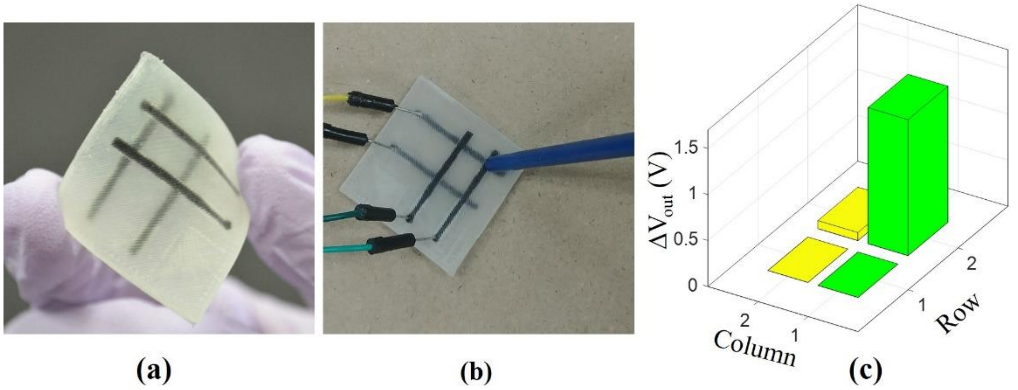

Figure 4.10. The 4-taxel sensor: (a) finished sensor that was 3D printed using the direct-print system. (b) pressure applied on one of the taxels; and (c) output data showing ΔV_{out} on that taxel [132].

4.5 Conformal 3D printing

Planar 3D printing comes short in the printing of a free-form or a curved feature [134]. There could be applications of the sensor where it needs to be printed on a curved, non-flat substrate [135]. Planar 3D printing of a curved feature will leave a stair-step effect as shown in Figure 4.11 [136]. Curvilinear toolpath that involves the XYZ movement simultaneously will result in a conformal 3D printing of a feature [137]. That will provide better printing resolution and better strength. Most importantly, the planar printing of conductive material may create a discontinuation due to the smaller area of surface contact. Conformal 3D printing reduces that chance for functional material printing. An application such as printing on tire surface or fingertip would require conformal 3D printing.

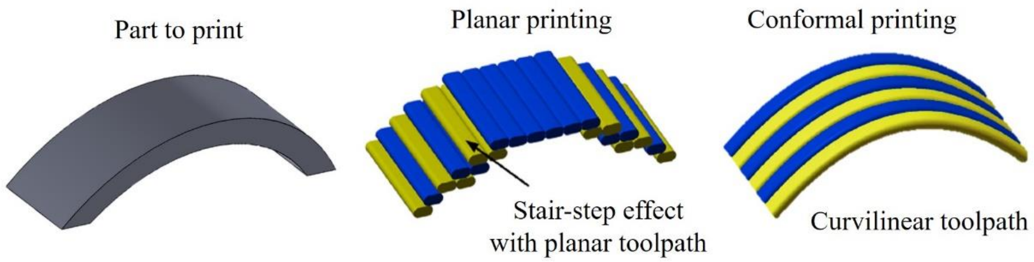

Figure 4.11. Difference between planar 3D printing and conformal 3D printing [136].

Figure 4.12 shows the schematic of a single-taxel sensor on a fingertip. This is a sensor on a curved surface that requires curvilinear toolpath. This is a good example to show the application of conformal 3D printing. Planar 3D printing will leave a stair-step effect with lower resolution for this sensor. A curvilinear toolpath will implement extrusion of material with simultaneous print-head movement in XYZ direction. The multi-material direct-print system was employed to print the sensor conformally on a fingertip with the modified prepolymer.

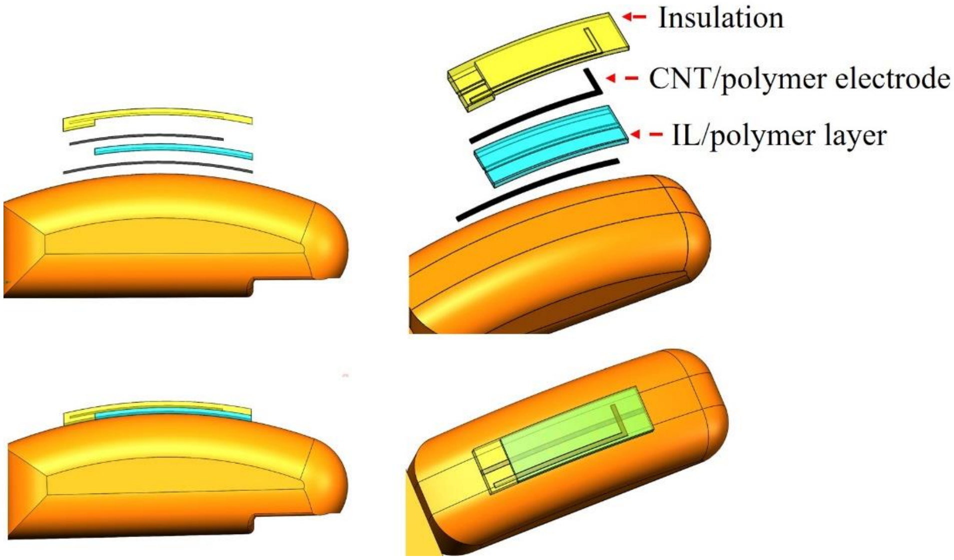

Figure 4.12. Schematic of a single-taxel sensor on a fingertip.

4.5.1 Curvilinear G-code generation

Alkadi et al. have developed an algorithm that conformally slices a 3D model to generate the curvilinear G-code or toolpath for printing [137]. A slicing surface was created to slice the 3D model by offsetting the surface of a freeform print-substrate. The perimeters of each layer were generated based on the intersections between the slicing surface and the 3D model of the part to be printed. The curvilinear infill toolpaths were created by projecting a 2D pattern (data points) onto the slicing surface to create a 3D pattern (data points). In this work, a sensor was conformally 3D printed on a fingertip that has a curved surface. As shown in Figure 4.13(a-b), the slicer surface was obtained from the curved face of the fingertip. This slicer was used to slice the sensor model to generate the curvilinear toolpath for 6 different layers of the sensor (Figure 4.13(c-i)). These toolpaths were used to develop the G-code for motion and extrusion control in the DP system.

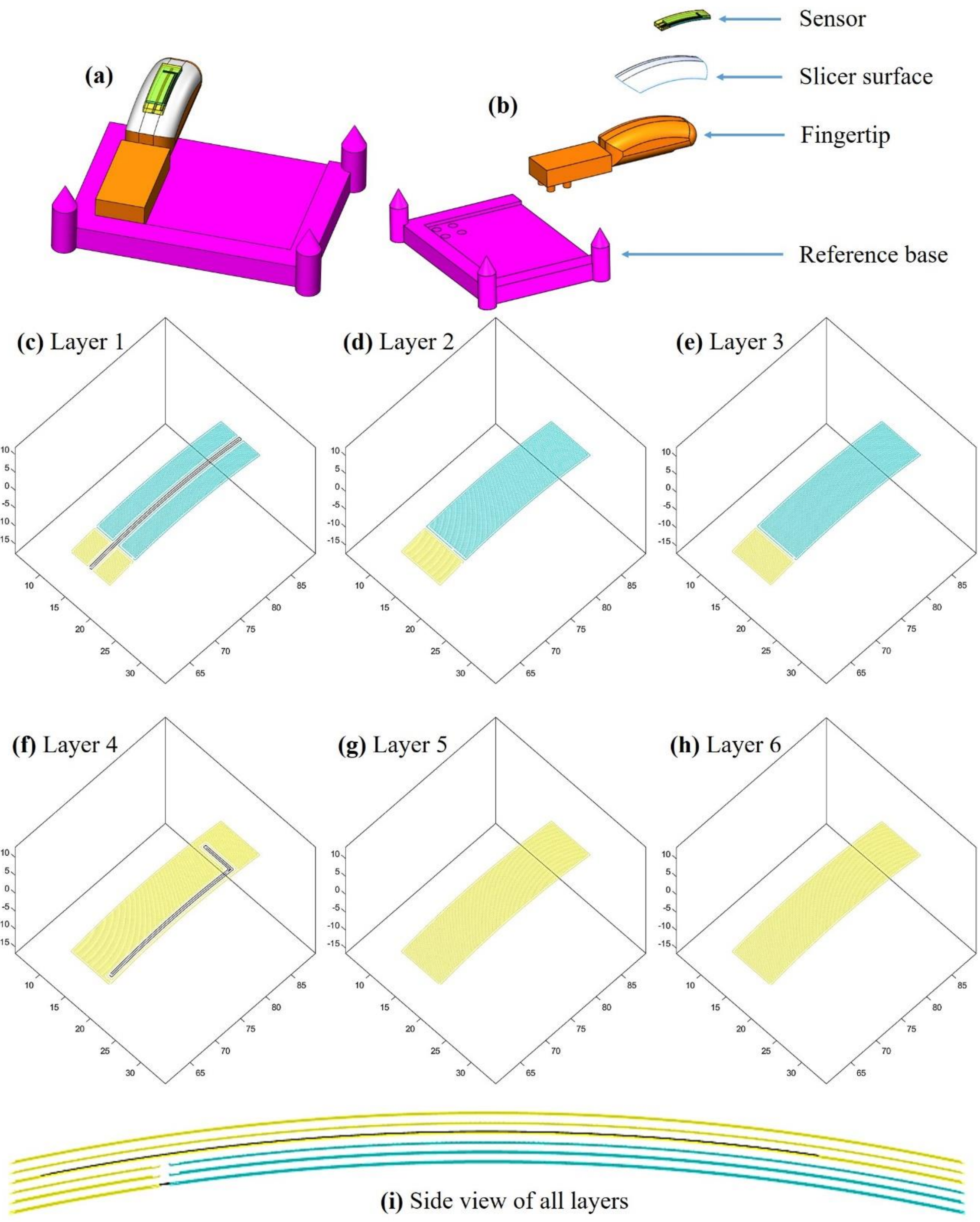

Figure 4.13. Conformal slicing: (a-b) slicer surface obtained from fingertip 3D model; (c-h) curvilinear toolpath for 6 layers of the sensor through conformal slicing; and (i) side view of curvilinear toolpath for all layers.

4.5.2 Non-flat sensor printing

As shown in Figure 4.14(a), a reference base was 3d printed using a commercial 3D printer (Objet, Eden 260V) for homing the DP system. A fingertip was also 3D printed using a commercial 3D printer that includes a curved top surface as shown in Figure 4.14(b). The fingertip was placed in the slots of the base for printing the sensor using the multi-material direct-print system. The sensor was conformally 3D printed on the curved surface of the fingertip using the DP system. Three extruders of the DP system was filled with three different materials: TangoPlus, IL/prepolymer, and CNT/prepolymer. For the IL/prepolymer layer, 1.0 wt.% IL was used with TangoPlus. All the materials for sensor printing were modified using fumed silica as described in section 4.3. The nozzle/tip inner diameter was 335 μm for all three extruders. The layer height was set at 300 μm, and the travel speed was set at 15 mm/s. Figure 4.14(g) shows the conformally printed sensor after curing.

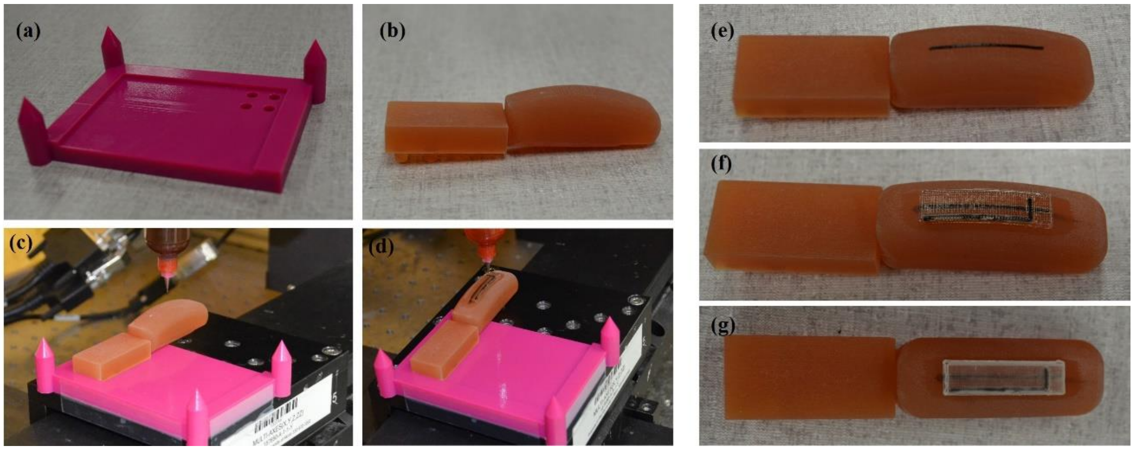

Figure 4.14. Conformal 3D printing of sensor: (a) 3D printed reference base using a commercial printer; (b) 3D printed fingertip using a commercial printer; (c-d) conformal sensor printing using the DP system; (e) conformally printed first CNT-based electrode; (f) conformally printed sensor before curing; and (g) after curing.

4.5.3 Conformally printed sensor evaluation

The conformally printed sensor was evaluated for different test conditions. The taxel on the printed sensor has an inclination angle with respect to the horizontal plane. To apply a normal compressive force on the taxel, the fingertip was rotated so that the inclination gets canceled out. From the CAD model, the inclination angle with the horizontal plane at the taxel was measured as 8.04°. The fingertip was placed on a rotation stage, and it was rotated 8°, as shown in Figure 4.15(a-b). The sensor was connected in an electrical circuit to create a potential divider. The external resistor and supplied voltage was 20 MΩ and 24 V, respectively. The voltage output across the external resistor was measured as the sensor output. Figure 4.15(c) shows the experimental setup for sensor testing where a force gauge was mounted on a motorized stage to apply a normal compressive force on the taxel. Sensor output and force data were collected through Matlab when the stage was controlled to apply force at different speeds. A probe with a diameter of 3 mm was attached to the force gauge to apply force on the taxel.

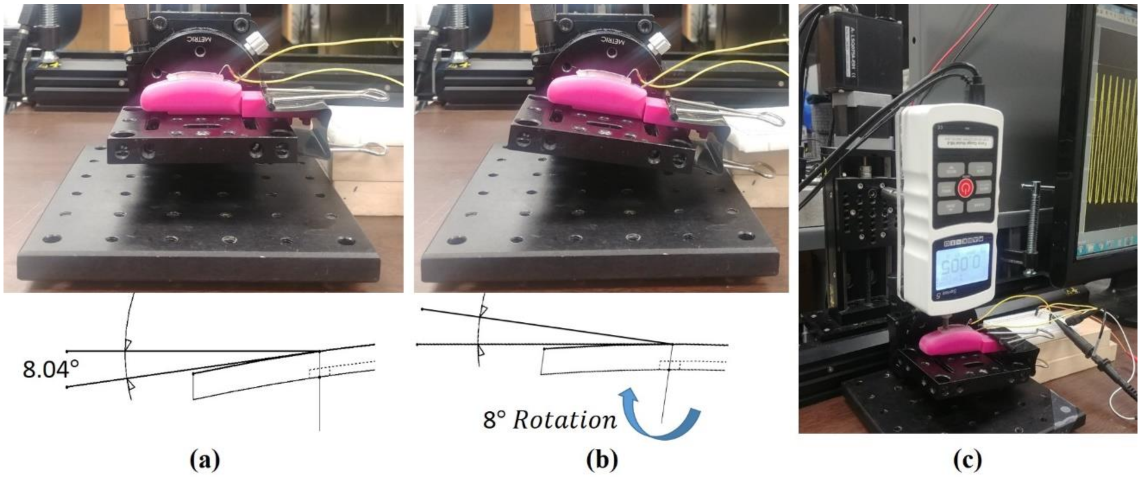

Figure 4.15. Conformally printed sensor test setup: (a) fingertip with the sensor mounted on rotation stage; (b) stage rotated 8° to apply force normally on the taxel; and (c) experimental setup with a force gauge and motorized stage.

Figure 4.16 shows the results for different sensor tests. First, the sensor was subjected to a fixed strain of 60% for multiple cycles at a probe speed of 0.1 mm/s. Figure 4.16(a) shows the applied force and relative change in voltage output from the sensor system in color red and green, respectively. Similar to flat sensors, there is a slight delay in the unloading curve, while the loading curves for force and sensor output are almost simultaneous. Again, this may occur due to the viscoelastic properties of the soft elastomer. The difference between loading and unloading was shown the hysteresis curve in Figure 4.16(b). The sensor was also tested for different probe speeds or strain rates. Figure 4.16(c) shows sensor output with increased force for probe speeds. As shown in the figure, the sensor shows a higher sensitivity at a lower strain rate. Figure 4.16(d) shows a portion of the result when the sensor underwent for few hundred force cycles at a probe speed of 1 mm/s.

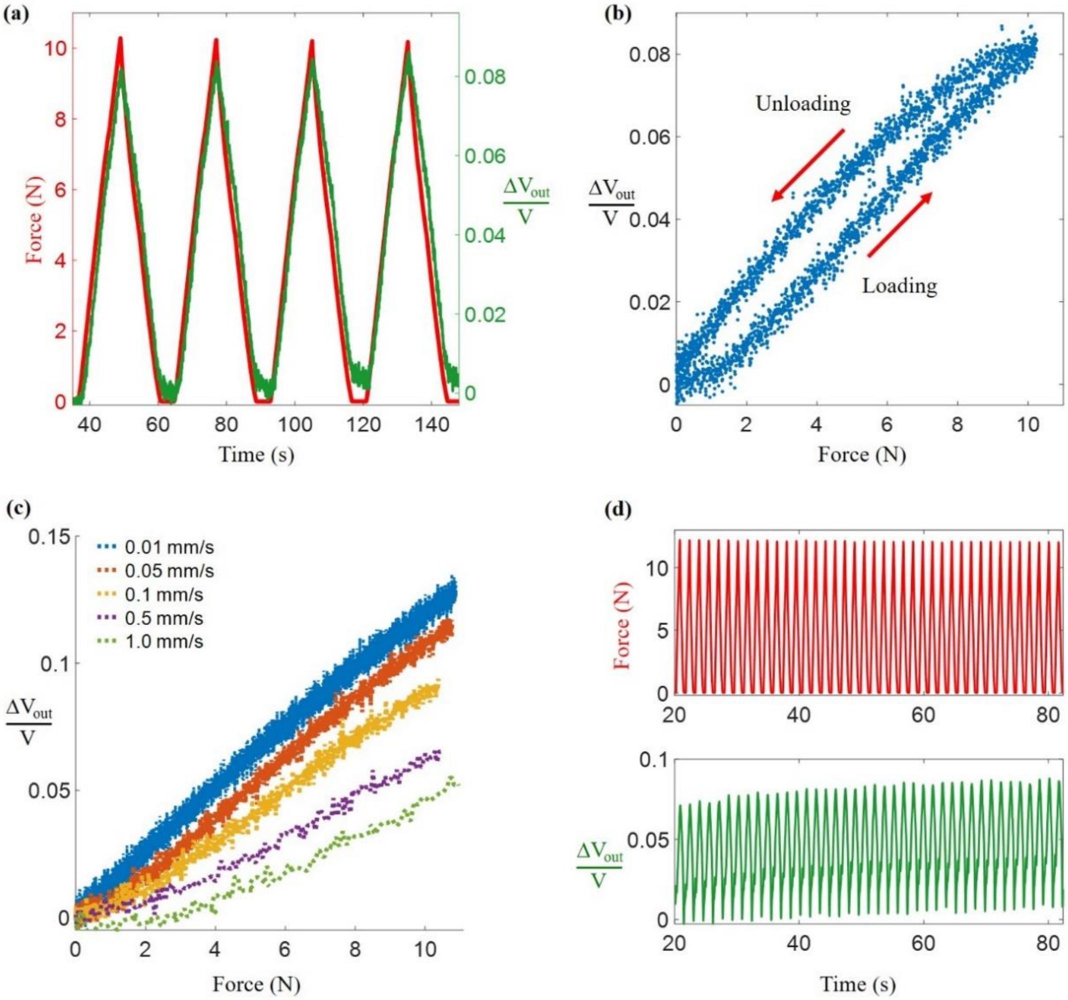

Figure 4.16. Conformally printed sensor evaluation: (a) applied force (in red) and sensor output (in green) at the same timestamp; (b) hysteresis curve of the sensor; (c) sensor output for different strain rate (probe speed); and (d) sensor out and applied force when it undergoes hundreds of cycles.

4.6 Comparison

Three sensors were fabricated through molding/screen printing, planar 3D printing, and conformal 3D printing. The geometry for all three sensors were maintained constant.

The IL/polymer layer height was set at 0.6 mm when the CNT-based electrode width was 0.8 mm. The IL ratio was maintained as 1 wt.% for all three sensors. However, the materials were modified for 3D printing. Pristine TangoPlus was used as a prepolymer for molding and screen printing process where fumed silica was used as a viscosifier with TangoPlus for 3D printing. The printing parameters for planar and conformal 3D printing were maintained fixed. A 335-µm nozzle was used for all the extruders with a layer height of 0.3 mm. The print-head travel speed was set as 15 mm/s. To investigate the sensor performance, all the sensors were subjected to a compressive normal force. The sensor system was connected to a potential divider when the sensor output was represented in terms of relative change in voltage output across the external resistor. Figure 4.17(a) shows the relative change in voltage with increasing force when force was applied at a probe speed of 0.5 mm/s. Figure 4.17(b) shows the relative change in voltage vs. force for a probe speed of 0.1 mm/s.

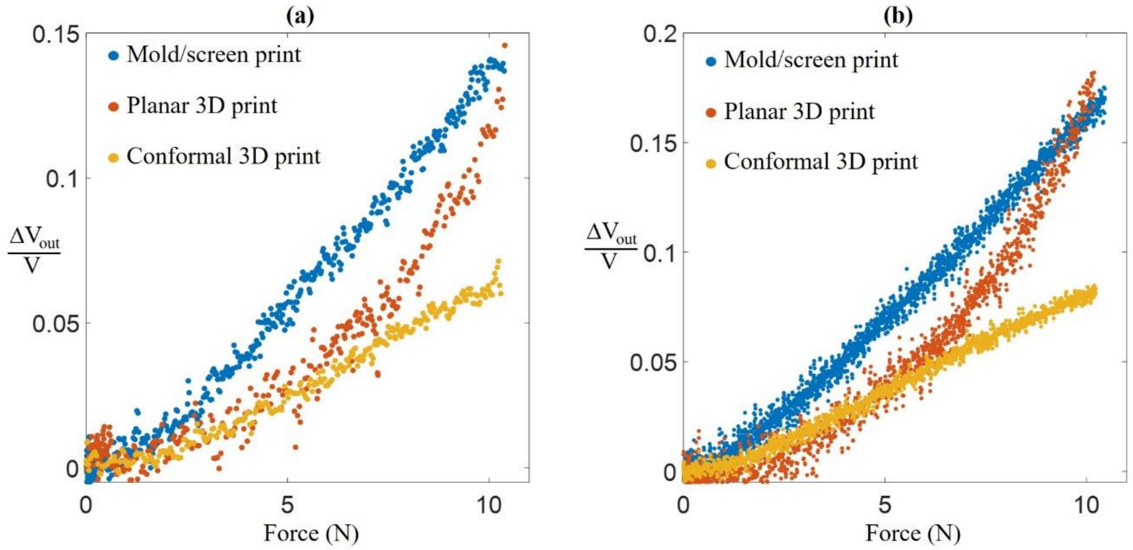

Figure 4.17. Comparing sensor fabricated through molding/screen printing, planar 3D printing, and conformal 3D printing: (a) sensor output when force applied at 0.5 mm/s; (b) sensor output when force applied at 0.1 mm/s.

Due to the modifications in materials, some differences in sensor responses were expected between molded and 3D printed sensors. As shown in Figure 4.17, up to around 10 N force, the molded sensor showed more relative change in voltage for the same applied force. This happened due to the difference in hardness between molded and 3D printed sensors. Because of the added fumed silica 3D printed sensors were harder with Shore A hardness of almost 50, where molded sensors had a Shore A hardness of around 27. The softer molded sensor generated more strain than the harder 3D printed sensor for the same applied force [138]. That resulted in a higher relative change in voltage for the softer sensor at the same force. Also, 3D printing does not create a smooth top surface like molding process. Rather, there was a wavy pattern in the top surface of a 3D printed sensor. This might induce some differences between 3D printed and molded sensors in how they response to external strain. However, after 10 N force, the planar 3D printed sensor showed more change in voltage. That could be the result of higher strain in the 3D printed sensor than molded one at a higher force range.

A difference between planar and conformal 3D printed sensor was observed. At the lower force range, up to around 6 N force, planar and conformal sensors showed a similar response. But, at higher force, the planar sensor showed higher relative change in voltage than the conformal one. This dissimilarity can be attributed to the difference in printing. Firstly, the raster angle (between x-axis and toolpath) was different for planar and conformal printing. For planar printing raster angle was 45°, where conformal printing had raster angles of 0° and 90° in IL/polymer layers. This might induce some differences in sensor response [139]. Secondly, conformal printing or curvilinear toolpath may have some effect on sensing performance. Thirdly, the applied force for a conformally printed sensor may not be fully normal. Although the fingertip was rotated to apply normal force on the taxel, 8° rotation brought only one point on the taxel at a horizontal plane. It was still a curved surface with small curvature. This small curvature could also play a role in the variation in sensor response. Finally, another dissimilarity between the planar and conformally 3D printed sensor is that the conformally 3D printed sensor did not have the bottom insulation layer which affected the strain distribution throughout the sensor cross-section. This also may contribute to the difference in sensor output.

4.7 Discussion

The printing parameters for three different materials in the sensor were investigated using the multi-material direct-print system developed in this work, and the system was successfully implemented in the fabrication of a soft stretchable sensor on flat and non-flat surfaces. While the soft sensor fabricated in this study showed consistent performance throughout the evaluation process, there are still opportunities for improvement of the proposed printing system. For example, a wiper brush and the corresponding motion instructions could be added to the system to enable cleaning of the extruder nozzle after the printing of each layer, as this would prevent contamination between materials. Currently, tips are manually wiped occasionally to prevent any contamination. Also, the modification of the IL/polymer and CNT/polymer composite with fumed silica could have some adverse effect on sensing performance and mechanical pliability. However, it is possible to calibrate the printed sensor according to its response. Besides, the sensor geometry and material composition can be easily varied to fine-tune the sensing performance.

The unloading behavior is different from the loading behavior for the stretchable sensor, as can be noticed from Figure 4.9(d) and Figure 4.16(b). The hysteresis was calculated to be in the range of 20% to 30%. This is a common phenomenon for viscoelastic elastomers due to their time-dependent elastic properties [140], [141]. However, there is consistency in the loading and unloading curves over multiple cycles. Figure 4.9(d) shows the results for 10 cycles where all the loading curves are similar and all unloading curves are similar but follow a different path. Thus, the sensor is able to provide a predictable response. Figure 4.9(b) shows stress relaxation under a constant strain, where part of the deformational energy is stored elastically and part of it is dissipated through viscous mechanisms [140]. This ability of the sensor to dissipate energy could be useful when there is a need for shock absorption, such as for smart insoles [63], [142] and smart helmets

[143]. The sensor also shows a deformation rate/strain rate–dependent response, as shown in Figure 4.9(c) and Figure 4.16(c). The viscoelastic materials cannot rearrange their molecules quickly enough during a short excitation to accommodate the strain. In contrast, during a long excitation, there is sufficient time for molecular rearrangement to occur [140], which is why the sensors show a deformation rate-dependent behavior. Overall, the sensor showed a reliable and consistent response over a few thousand pressing cycles.

The hysteresis shown in Figure 4.9(d) and Figure 4.16(b) are only for a few cycles. Dislocation of the hysteresis curves was noticed for a higher number of cycles. However, the sensor response to external force was beyond the hysteresis dislocation between cycles for a multi-cycle experiment. Future studies could be conducted on hysteresis dislocation, fatigue, and stress relaxation for thousands of force cycles. Also, Figure 4.9 and Figure 4.16 show other errors such as precision, linearity, and zero errors. Some errors can be attributed to the electrical noise, experimental inconsistencies, material impurities, etc. When the scope of this study is limited, further investigation on these errors can be conducted in the future works.

4.8 Sensor application in gloves

A visual grasp aid for neuropathy patients was developed by assembling a 3D printed sensor and a microcontroller board on a glove. Neuropathy is a nerve-damaging disease, which causes those affected to lose feeling in their otherwise functional limbs [144]. It can cause permanent numbing to the peripheral limbs of a patient such as hands or feet [145]. A real-time visualization aid for grasp analysis was developed that can be used by the patients experiencing numbing of the limb. This wearable electronic device, developed on an open-source platform, provides the patient with a visual light scale to allow them to understand the strength of the grasp they have on any object. A flat sensor was 3D printed utilizing the multi-material direct-print system. Next, the fabricated sensor was integrated with a microcontroller board and installed on a glove. The developed glove is referred to as *NeuroGlove*. This is a preliminary study where ongoing works include 3D printing of sensors directly on a robotic or a prosthetic hand.

Recently, the open-source microcontroller boards made it easier to implement tools in various applications. There are many microcontroller boards commercially available with integrated sensors, lights, and accelerometer. Microcontroller boards such as Arduino are not expensive ($20-$40) and easy to apply. These boards can be programmed for a specific task where the coding can be based on programming language C++. In this work, a microcontroller (Circuit Playground, Adafruit, New York City, NY) was integrated with a sensor, and it programmed to respond in a light scale according to the applied force on the sensor. Finally, the sensor-microcontroller system was mounted on a glove to develop a wearable visual aid for neuropathy patients. The developed *NeuroGlove* was calibrated for zero to the highest force on the sensor. It was examined for different grasping force conditions. Figure 4.18 shows the wiring diagram, *NeuroGlove* assembly, and grasping experiments.

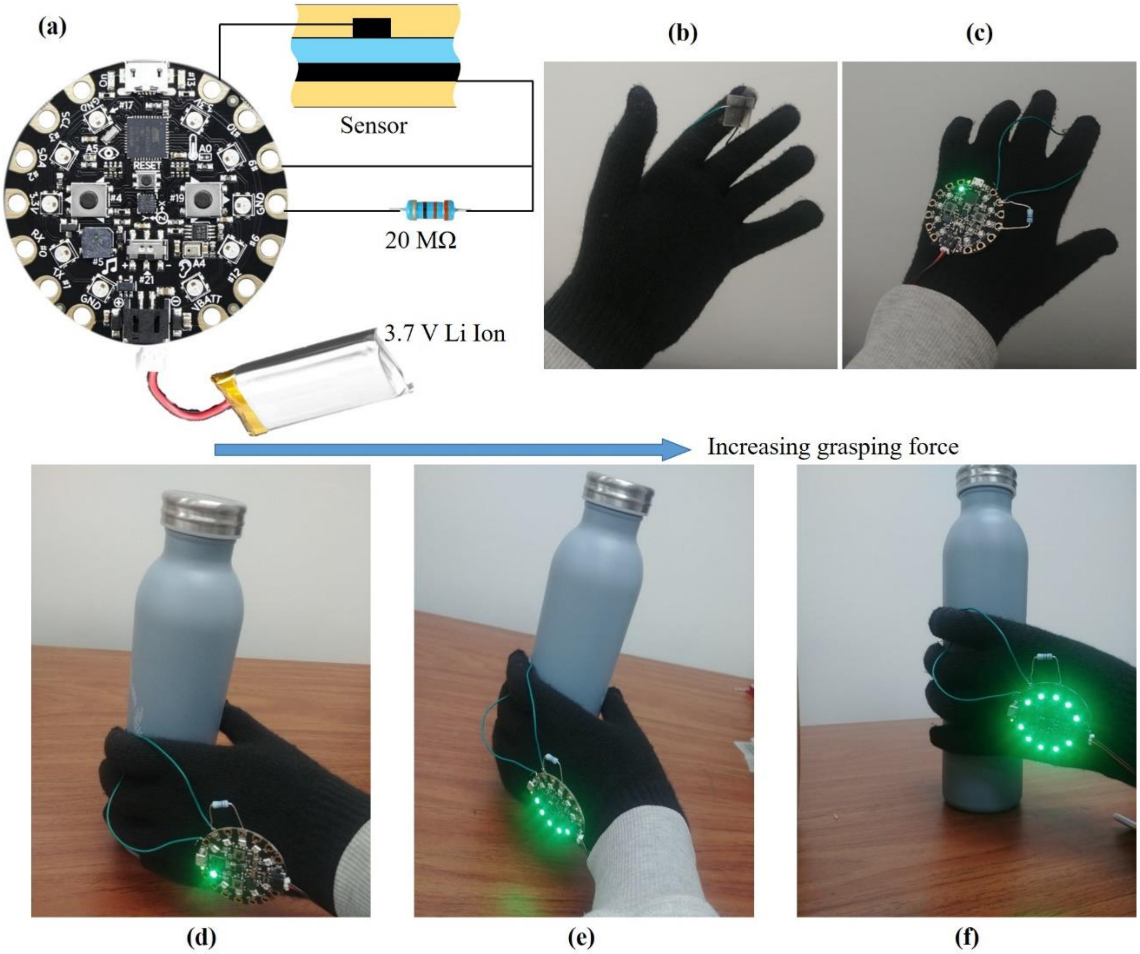

Figure 4.18. Visual grasp aid for neuropathy patients (*NeuroGlove*): (a) wiring diagram of the sensor and microcontroller; (b) attached 3D printed tactile sensor; (c) attached microcontroller board on the glove; (d) no grasping; (e) moderate grasping; and (f) highest grasping force applied.

CHAPTER V

CONCLUSIONS AND FUTURE WORKS

5.1 Conclusions

In this work, an ionic liquid (IL)-based stretchable sensor was proposed that responds to external force or strain. An IL/polymer blend for pressure-sensitive layer and a CNT/polymer composite for stretchable conductors were developed to fabricate the sensor. Initially, the sensor was fabricated via a combination of molding and screen printing processes, and it was characterized for different manufacturing variables. Next, the sensor was fabricated through the 3D printing process. A multi-material direct-print system was developed that is capable of printing functional materials. The extrusion-based system can handle three different materials in a single print. Materials for the sensor were modified for printing while maintaining their functionality. A planar 3D printing and a conformal 3D printing technique were employed to print a flat and a non-flat sensor, respectively. The 3D printed soft pressure sensors were evaluated for various loading conditions. Also, sensors fabricated through molding/screen-printing, planar 3D printing, and conformal 3D printing were compared for their responses.

Different applications of the sensor were explored such as *Smart tires*, *Smart insoles*, and *NeuroGloves*. For smart tire, a 12-taxel sensor was embedded in a 3D printed tire model. The tire was driven with a chassis and examined for different load conditions. A 3D printed insole with sensors was investigated for different landing conditions such as heel landing, midfoot landing, and forefoot landing. Finally, a 3D printed sensor was used to develop a visual aid for neuropathy patients. The sensor was integrated with a microcontroller board to respond on a light scale depending on the applied force on the sensor. The sensor-microcontroller system was installed on a glove and applied to various grasping experiments.

Introducing ILs in the fabrication of a soft pressure sensor gives more control over sensor performance, and this opens new possibilities for research and application. Multi-material 3D printing can provide unparalleled manufacturing and design flexibility, as it enables the use of a wide variety of materials. The flexibility and stretchability of the developed soft sensor make it suitable for applications where parts are moveable or are subjected to bending, flexing, and impact. The 3D printing process enables sensors to be fabricated on a freeform surface with a complex geometry. The work presented in this study is believed to enhance the research on 3D printed soft electronics and to open new avenues in the area of wearable devices, smart technologies, human-machine interfaces, and prosthetics.

5.2 Future works

There are still opportunities to work on and progress from the work done. The development and findings of this work can prompt newer applications. This work provides direction for novel future works. Ongoing research includes a shear force sensor and conformal 3D printing of smart tires. Also, the piezoelectric phenomenon of the IL/polymer blend is also being investigated. IL-based piezoelectric sensors and actuators are potential future research areas.

5.2.1 Shear force measurement

The sensor configuration can be modified to determine shear force or tangential force. Figure 5.1(a) shows a reconfigured sensor with IL/polymer. A comparative analysis of the relative change in the resistances R_1, R_2, and R_3 can provide information about the direction and type of the force applied. For example, a local shear applied to the top-left corner, as shown in Figure 5.1(c), will reduce the resistance R_1 while R_2 and R_3 will not change significantly. Different IL concentrations, mechanical properties of IL/polymer, geometries, and electrical circuitries could be investigated for developing a sensor that would be able to measure both shear and normal force. Research is ongoing for developing shear sensors. This sensor could play an important role to analyze the walking or running biomechanics if applied in an insole. Valuable information can be obtained from the sensor which is believed to be useful for biomedical applications such as gait analysis.

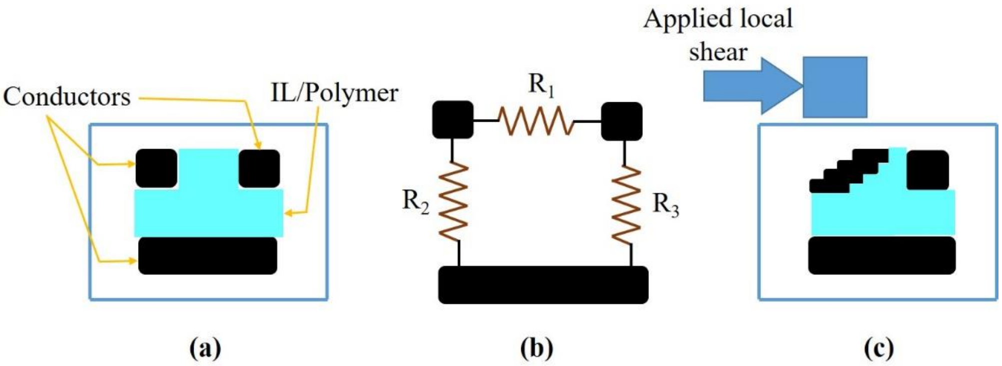

Figure 5.1. Shear force or tangential force measurement mechanism: (a) sectional view of sensor; (b) electrical resistances between different conductors; and (c) resistance change through applied shear.

5.2.2 Smart tires through conformal 3D printing

A conformal 3D printing to print sensor with tire tread on a free-form surface is envisioned. This will involve multi-material conformal additive manufacturing (MMCAM). The MMCAM will provide a unique opportunity for design customization depending on the feedback from the sensor. This solution could be used in the tire development phase for investigating different tread designs. The current mold based tire fabrication process is expensive and time-consuming. Also, the pressure pad-based tire footprint measurement technique lacks real tire-road interaction. A sensor embedded tire will provide real road-tire interaction data. Depending on the feedback received from the sensor, tread design customization can be easily realized via 3D printing. The planar printing of the tread-sensor has already been investigated. Figure 5.2(a) shows the exploded schematic of a 12-taxel tread-sensor where the yellow layer is IL/polymer. Figure 5.2(b) shows the 3D printed tread-sensor via the multi-material direct-print system. A smaller-scale wheel and tire were 3D printed using a commercial printer (Figure 5.2(c)). The tread-sensor printed with the DP system will be mounted on the wheel and will be investigated for different driving conditions.

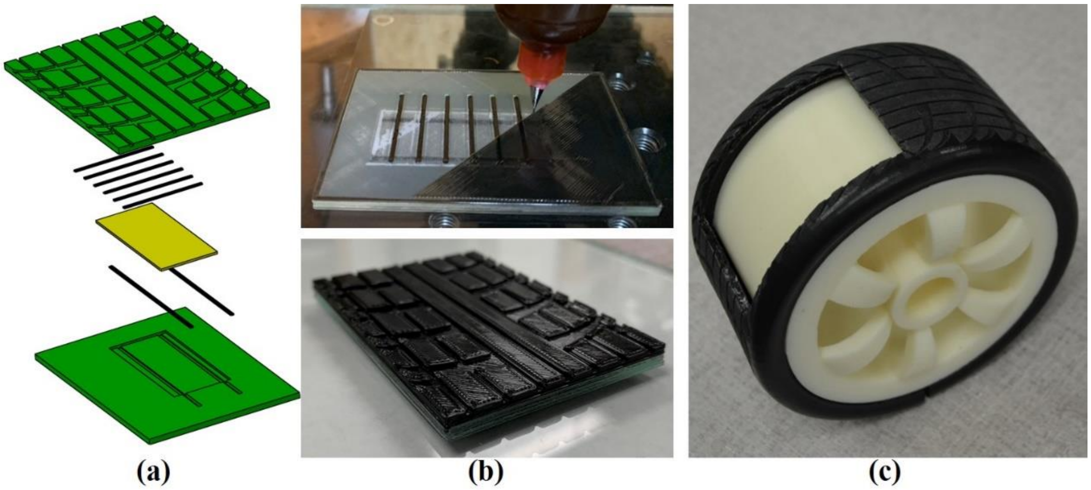

Figure 5.2. 3D printed tread with the sensor: (a) schematic of tread-sensor; (b) tread-senor being printed via multi-material DP system; and (c) tread sensor to be mounted on the wheel.

5.2.3 Piezoelectric pressure sensor

This work presented a piezoresistive sensor based on IL/polymer blend. However, it is observed that by increasing the IL ratio in the polymer, the piezoelectric phenomenon can also be obtained in the IL/polymer membrane. The ionic liquid used in this work is $EMIMBF_4$ that has a larger cation and a smaller anion, as shown in Figure 5.3. Because of the size difference in the ions, when the IL/polymer goes under strain, the ions reorient and creates a potential difference between the electrodes [146]. More than 20 wt.% IL with certain polymers shows the piezoelectric phenomenon that has the potential to be applied as a sensor or an actuator.

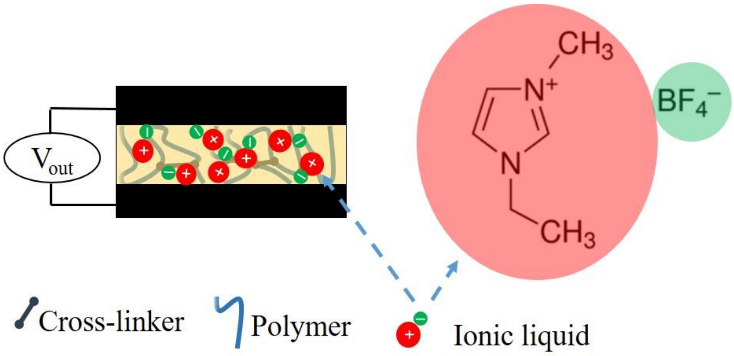

Figure 5.3. Different sizes of ions in the ionic liquid that induces potential difference under strain

REFERENCES

[1] N. Lu and D.-H. Kim, “Flexible and Stretchable Electronics Paving the Way for Soft Robotics,” *Soft Robot.*, vol. 1, no. 1, pp. 53–62, Jul. 2013, doi: 10.1089/soro.2013.0005.

[2] A. Chortos, J. Liu, and Z. Bao, “Pursuing prosthetic electronic skin,” *Nat. Mater.*, vol. 15, no. 9, pp. 937–950, Sep. 2016, doi: 10.1038/nmat4671.

[3] S. Kumbay Yildiz, R. Mutlu, and G. Alici, “Fabrication and characterisation of highly stretchable elastomeric strain sensors for prosthetic hand applications,” *Sens. Actuators Phys.*, vol. 247, pp. 514–521, Aug. 2016, doi: 10.1016/j.sna.2016.06.037.

[4] M. Amjadi, K.-U. Kyung, I. Park, and M. Sitti, “Stretchable, Skin-Mountable, and Wearable Strain Sensors and Their Potential Applications: A Review,” *Adv. Funct. Mater.*, vol. 26, no. 11, pp. 1678–1698, 2016, doi: 10.1002/adfm.201504755.

[5] X. Wang, Z. Liu, and T. Zhang, “Flexible Sensing Electronics for Wearable/Attachable Health Monitoring,” *Small*, vol. 13, no. 25, p. 1602790, 2017, doi: 10.1002/smll.201602790.

[6] C. Dagdeviren *et al.*, “Recent progress in flexible and stretchable piezoelectric devices for mechanical energy harvesting, sensing and actuation,” *Extreme Mech. Lett.*, vol. 9, pp. 269–281, Dec. 2016, doi: 10.1016/j.eml.2016.05.015.

[7] R. K. Kramer, C. Majidi, R. Sahai, and R. J. Wood, “Soft curvature sensors for joint angle proprioception,” in *2011 IEEE/RSJ International Conference on Intelligent Robots and Systems*, 2011, pp. 1919–1926, doi: 10.1109/IROS.2011.6094701.

[8] A. Fassler and C. Majidi, “Soft-matter capacitors and inductors for hyperelastic strain sensing and stretchable electronics,” *Smart Mater. Struct.*, vol. 22, no. 5, p. 055023, Apr. 2013, doi: 10.1088/0964-1726/22/5/055023.

[9] P. Polygerinos, K. C. Galloway, E. Savage, M. Herman, K. O. Donnell, and C. J. Walsh, “Soft robotic glove for hand rehabilitation and task specific training,” in *2015 IEEE International Conference on Robotics and Automation (ICRA)*, 2015, pp. 2913–2919, doi: 10.1109/ICRA.2015.7139597.

[10] M. O. F. E. Emon, J. Lee, U. H. Choi, D.-H. Kim, K. C. Lee, and J.-W. Choi, “Characterization of a Soft Pressure Sensor on the Basis of Ionic Liquid Concentration and Thickness of the Piezoresistive Layer,” *IEEE Sens. J.*, 2019.

[11] Y. Xu *et al.*, “The Boom in 3D-Printed Sensor Technology,” *Sensors*, vol. 17, no. 5, p. 1166, May 2017, doi: 10.3390/s17051166.

[12] J. T. Muth *et al.*, “Embedded 3D Printing of Strain Sensors within Highly Stretchable Elastomers,” *Adv. Mater.*, vol. 26, no. 36, pp. 6307–6312, 2014, doi: 10.1002/adma.201400334.

[13] M. Vatani, E. D. Engeberg, and J.-W. Choi, “Force and slip detection with direct-write compliant tactile sensors using multi-walled carbon nanotube/polymer composites,” *Sens. Actuators Phys.*, vol. 195, pp. 90–97, Jun. 2013, doi: 10.1016/j.sna.2013.03.019.

[14] D. K. Patel, A. H. Sakhaei, M. Layani, B. Zhang, Q. Ge, and S. Magdassi, “Highly Stretchable and UV Curable Elastomers for Digital Light Processing Based 3D Printing,” *Adv. Mater.*, vol. 29, no. 15, p. 1606000, 2017, doi: 10.1002/adma.201606000.

[15] T. Sekitani, Y. Noguchi, K. Hata, T. Fukushima, T. Aida, and T. Someya, “A Rubberlike Stretchable Active Matrix Using Elastic Conductors,” *Science*, vol. 321, no. 5895, pp. 1468–1472, Sep. 2008, doi: 10.1126/science.1160309.

[16] M. Amjadi, Y. J. Yoon, and I. Park, “Ultra-stretchable and skin-mountable strain sensors using carbon nanotubes–Ecoflex nanocomposites,” *Nanotechnology*, vol. 26, no. 37, p. 375501, Aug. 2015, doi: 10.1088/0957-4484/26/37/375501.

[17] Kenry, J. C. Yeo, and C. T. Lim, “Emerging flexible and wearable physical sensing platforms for healthcare and biomedical applications,” *Microsyst. Nanoeng.*, vol. 2, no. 1, pp. 1–19, Sep. 2016, doi: 10.1038/micronano.2016.43.

[18] H. Hocheng and C.-M. Chen, “Design, Fabrication and Failure Analysis of Stretchable Electrical Routings,” *Sensors*, vol. 14, no. 7, pp. 11855–11877, Jul. 2014, doi: 10.3390/s140711855.

[19] Alamusi, N. Hu, H. Fukunaga, S. Atobe, Y. Liu, and J. Li, “Piezoresistive Strain Sensors Made from Carbon Nanotubes Based Polymer Nanocomposites,” *Sensors*, vol. 11, no. 11, pp. 10691–10723, Nov. 2011, doi: 10.3390/s111110691.

[20] M. Vatani, M. Vatani, and J. W. Choi, “Multi-layer stretchable pressure sensors using ionic liquids and carbon nanotubes,” *Appl. Phys. Lett.*, vol. 108, no. 6, p. 061908, Feb. 2016, doi: 10.1063/1.4941812.

[21] D. Y. Choi *et al.*, “Highly Stretchable, Hysteresis-Free Ionic Liquid-Based Strain Sensor for Precise Human Motion Monitoring,” *ACS Appl. Mater. Interfaces*, vol. 9, no. 2, pp. 1770–1780, Jan. 2017, doi: 10.1021/acsami.6b12415.

[22] K. N. Marsh, J. A. Boxall, and R. Lichtenthaler, “Room temperature ionic liquids and their mixtures—a review,” *Fluid Phase Equilibria*, vol. 219, no. 1, pp. 93–98, May 2004, doi: 10.1016/j.fluid.2004.02.003.

[23] H. Ohno, “Design of Ion Conductive Polymers Based on Ionic Liquids,” *Macromol. Symp.*, vol. 249–250, no. 1, pp. 551–556, 2007, doi: 10.1002/masy.200750435.

[24] H. Ota *et al.*, “Highly deformable liquid-state heterojunction sensors,” *Nat. Commun.*, vol. 5, p. 5032, Sep. 2014, doi: 10.1038/ncomms6032.

[25] J.-B. Chossat, H.-S. Shin, Y.-L. Park, and V. Duchaine, “Soft Tactile Skin Using an Embedded Ionic Liquid and Tomographic Imaging,” *J. Mech. Robot.*, vol. 7, no. 2, pp. 021008-021008–9, May 2015, doi: 10.1115/1.4029474.

[26] J. Chossat, Y. Park, R. J. Wood, and V. Duchaine, “A Soft Strain Sensor Based on Ionic and Metal Liquids,” *IEEE Sens. J.*, vol. 13, no. 9, pp. 3405–3414, Sep. 2013, doi: 10.1109/JSEN.2013.2263797.

[27] D. M. Vogt, Y. Park, and R. J. Wood, “Design and Characterization of a Soft Multi-Axis Force Sensor Using Embedded Microfluidic Channels,” *IEEE Sens. J.*, vol. 13, no. 10, pp. 4056–4064, Oct. 2013, doi: 10.1109/JSEN.2013.2272320.

[28] W. Hu, X. Niu, R. Zhao, and Q. Pei, “Elastomeric transparent capacitive sensors based on an interpenetrating composite of silver nanowires and polyurethane,” *Appl. Phys. Lett.*, vol. 102, no. 8, p. 083303, Feb. 2013, doi: 10.1063/1.4794143.

[29] C. Majidi, R. Kramer, and R. J. Wood, “A non-differential elastomer curvature sensor for softer-than-skin electronics,” *Smart Mater. Struct.*, vol. 20, no. 10, p. 105017, Aug. 2011, doi: 10.1088/0964-1726/20/10/105017.

[30] C. Lee, L. Jug, and E. Meng, “High strain biocompatible polydimethylsiloxane-based conductive graphene and multiwalled carbon nanotube nanocomposite strain sensors,” *Appl. Phys. Lett.*, vol. 102, no. 18, p. 183511, May 2013, doi: 10.1063/1.4804580.

[31] T. D. Ngo, A. Kashani, G. Imbalzano, K. T. Q. Nguyen, and D. Hui, “Additive manufacturing (3D printing): A review of materials, methods, applications and challenges,” *Compos. Part B Eng.*, vol. 143, pp. 172–196, Jun. 2018, doi: 10.1016/j.compositesb.2018.02.012.

[32] L. E. Murr, “Frontiers of 3D Printing/Additive Manufacturing: from Human Organs to Aircraft Fabrication†,” *J. Mater. Sci. Technol.*, vol. 32, no. 10, pp. 987–995, Oct. 2016, doi: 10.1016/j.jmst.2016.08.011.

[33] S.-Z. Guo, K. Qiu, F. Meng, S. H. Park, and M. C. McAlpine, “3D Printed Stretchable Tactile Sensors,” *Adv. Mater.*, vol. 29, no. 27, p. 1701218, 2017, doi: 10.1002/adma.201701218.

[34] R. Matsuzaki and A. Todoroki, “Wireless Monitoring of Automobile Tires for Intelligent Tires,” *Sensors*, vol. 8, no. 12, pp. 8123–8138, Dec. 2008, doi: 10.3390/s8128123.

[35] J. Yi, “A Piezo-Sensor-Based ‘Smart Tire’ System for Mobile Robots and Vehicles,” *IEEEASME Trans. Mechatron.*, vol. 13, no. 1, pp. 95–103, Feb. 2008, doi: 10.1109/TMECH.2007.915064.

[36] R. Matsuzaki and A. Todoroki, “Wireless strain monitoring of tires using electrical capacitance changes with an oscillating circuit,” *Sens. Actuators Phys.*, vol. 119, no. 2, pp. 323–331, Apr. 2005, doi: 10.1016/j.sna.2004.10.014.

[37] Y. Zhang, J. Yi, and T. Liu, “Embedded Flexible Force Sensor for In-Situ Tire–Road Interaction Measurements,” *IEEE Sens. J.*, vol. 13, no. 5, pp. 1756–1765, May 2013, doi: 10.1109/JSEN.2013.2241051.

[38] J. J. Castillo Aguilar, J. A. Cabrera Carrillo, A. J. Guerra Fernández, and E. Carabias Acosta, “Robust Road Condition Detection System Using In-Vehicle Standard Sensors,” *Sensors*, vol. 15, no. 12, pp. 32056–32078, Dec. 2015, doi: 10.3390/s151229908.

[39] L. Ann Myers, R. Roque, B. E. Ruth, and C. Drakos, “Measurement of Contact Stresses for Different Truck Tire Types To Evaluate Their Influence on Near-Surface Cracking and Rutting,” *Transp. Res. Rec.*, vol. 1655, no. 1, pp. 175–184, Jan. 1999, doi: 10.3141/1655-23.

[40] C.-R. Lee, J.-W. Kim, J. O. Hallquist, Y. Zhang, and A. D. Farahani, “Validation of a FEA Tire Model for Vehicle Dynamic Analysis and Full Vehicle Real Time Proving Ground Simulations,” SAE International, Warrendale, PA, SAE Technical Paper 971100, Feb. 1997. doi: 10.4271/971100.

[41] S. Urry, “Plantar pressure-measurement sensors,” *Meas. Sci. Technol.*, vol. 10, no. 1, pp. R16–R32, Jan. 1999, doi: 10.1088/0957-0233/10/1/017.

[42] A. H. A. Razak, A. Zayegh, R. K. Begg, and Y. Wahab, “Foot Plantar Pressure Measurement System: A Review,” *Sensors*, vol. 12, no. 7, pp. 9884–9912, Jul. 2012, doi: 10.3390/s120709884.

[43] L. Shu, T. Hua, Y. Wang, Q. Li, D. D. Feng, and X. Tao, “In-Shoe Plantar Pressure Measurement and Analysis System Based on Fabric Pressure Sensing Array,” *IEEE Trans. Inf. Technol. Biomed.*, vol. 14, no. 3, pp. 767–775, May 2010, doi: 10.1109/TITB.2009.2038904.

[44] M. J. Mueller, “Application of Plantar Pressure Assessment in Footwear and Insert Design,” *J. Orthop. Sports Phys. Ther.*, vol. 29, no. 12, pp. 747–755, Dec. 1999, doi: 10.2519/jospt.1999.29.12.747.

[45] S. J. Morris and J. A. Paradiso, “Shoe-integrated sensor system for wireless gait analysis and real-time feedback,” in *Proceedings of the Second Joint 24th Annual Conference and the Annual Fall Meeting of the Biomedical Engineering Society] [Engineering in Medicine and Biology*, 2002, vol. 3, pp. 2468–2469 vol.3, doi: 10.1109/IEMBS.2002.1053379.

[46] Meng Chen, Bufu Huang, and Yangsheng Xu, "Intelligent shoes for abnormal gait detection," in *2008 IEEE International Conference on Robotics and Automation*, 2008, pp. 2019–2024, doi: 10.1109/ROBOT.2008.4543503.

[47] S. J. M. Bamberg, A. Y. Benbasat, D. M. Scarborough, D. E. Krebs, and J. A. Paradiso, "Gait Analysis Using a Shoe-Integrated Wireless Sensor System," *IEEE Trans. Inf. Technol. Biomed.*, vol. 12, no. 4, pp. 413–423, Jul. 2008, doi: 10.1109/TITB.2007.899493.

[48] World Health Organization, Ed., *Global report on diabetes*. Geneva, Switzerland: World Health Organization, 2016.

[49] C. N. Martyn and R. A. Hughes, "Epidemiology of peripheral neuropathy.," *J. Neurol. Neurosurg. Psychiatry*, vol. 62, no. 4, pp. 310–318, Apr. 1997.

[50] J. K. Anastasi, B. Capili, and M. Chang, "HIV Peripheral Neuropathy and Foot Care Management: A Review of Assessment and Relevant Guidelines," *AJN Am. J. Nurs.*, vol. 113, no. 12, p. 34, Dec. 2013, doi: 10.1097/01.NAJ.0000438867.67777.69.

[51] S. Quasthoff and H. P. Hartung, "Chemotherapy-induced peripheral neuropathy," *J. Neurol.*, vol. 249, no. 1, pp. 9–17, Jan. 2002, doi: 10.1007/PL00007853.

[52] A. Vinik, C. Casellini, and M.-L. Nevoret, "Diabetic Neuropathies," in *Endotext*, K. R. Feingold, B. Anawalt, A. Boyce, G. Chrousos, K. Dungan, A. Grossman, J. M. Hershman, G. Kaltsas, C. Koch, P. Kopp, M. Korbonits, R. McLachlan, J. E. Morley, M. New, L. Perreault, J. Purnell, R. Rebar, F. Singer, D. L. Trence, A. Vinik, and D. P. Wilson, Eds. South Dartmouth (MA): MDText.com, Inc., 2000.

[53] ASTM International, Committee F42, "F2792-10 Standard Terminology for Additive Manufacturing Technologies," ASTM International, West Conshohocken, PA, 2010. doi: 10.1520/F2792-10.

[54] Y. Huang, M. C. Leu, J. Mazumder, and A. Donmez, "Additive Manufacturing: Current State, Future Potential, Gaps and Needs, and Recommendations," *J. Manuf. Sci. Eng.*, vol. 137, no. 1, Feb. 2015, doi: 10.1115/1.4028725.

[55] Wohlers Associates Inc., "Wohlers Report 2013: Additive Manufacturing and 3D Printing State of the Industry," Wohlers Associates, Fort Collins, CO, 2013.

[56] K. V. Wong and A. Hernandez, "A Review of Additive Manufacturing," *ISRN Mech. Eng.*, pp. 1–10, Jan. 2012, doi: 10.5402/2012/208760.

[57] M. Vatani and J.-W. Choi, "Direct-print photopolymerization for 3D printing," *Rapid Prototyp. J.*, vol. 23, no. 2, pp. 337–343, Mar. 2017, doi: 10.1108/RPJ-11-2015-0172.

[58] Z. Bao and X. Chen, "Flexible and Stretchable Devices," *Adv. Mater.*, vol. 28, no. 22, pp. 4177–4179, 2016, doi: 10.1002/adma.201601422.

[59] D. P. Dubal, N. R. Chodankar, D.-H. Kim, and P. Gomez-Romero, “Towards flexible solid-state supercapacitors for smart and wearable electronics,” *Chem. Soc. Rev.*, vol. 47, no. 6, pp. 2065–2129, 2018, doi: 10.1039/C7CS00505A.

[60] S. Bauer, S. Bauer-Gogonea, I. Graz, M. Kaltenbrunner, C. Keplinger, and R. Schwödiauer, “25th Anniversary Article: A Soft Future: From Robots and Sensor Skin to Energy Harvesters,” *Adv. Mater.*, vol. 26, no. 1, pp. 149–162, 2014, doi: 10.1002/adma.201303349.

[61] X. Wang *et al.*, “Development of a flexible and stretchable tactile sensor array with two different structures for robotic hand application,” *RSC Adv.*, vol. 7, no. 76, pp. 48461–48465, 2017, doi: 10.1039/C7RA08605A.

[62] A. P. Gerratt, H. O. Michaud, and S. P. Lacour, “Elastomeric Electronic Skin for Prosthetic Tactile Sensation,” *Adv. Funct. Mater.*, vol. 25, no. 15, pp. 2287–2295, 2015, doi: 10.1002/adfm.201404365.

[63] M. O. F. Emon and J.-W. Choi, “A Preliminary Study on 3D Printed Smart Insoles With Stretchable Piezoresistive Sensors for Plantar Pressure Monitoring,” presented at the ASME 2017 International Mechanical Engineering Congress and Exposition, 2017, p. V002T02A028-V002T02A028, doi: 10.1115/IMECE2017-71817.

[64] T. Q. Trung and N.-E. Lee, “Flexible and Stretchable Physical Sensor Integrated Platforms for Wearable Human-Activity Monitoringand Personal Healthcare,” *Adv. Mater.*, vol. 28, no. 22, pp. 4338–4372, 2016, doi: 10.1002/adma.201504244.

[65] X. Chen *et al.*, “Evaluation of Helmet Comfort Based on Flexible Pressure Sensor Matrix,” in *Intelligent Human Systems Integration 2019*, 2019, pp. 833–839.

[66] Y. Li, S. Luo, M.-C. Yang, R. Liang, and C. Zeng, “Poisson Ratio and Piezoresistive Sensing: A New Route to High-Performance 3D Flexible and Stretchable Sensors of Multimodal Sensing Capability,” *Adv. Funct. Mater.*, vol. 26, no. 17, pp. 2900–2908, 2016, doi: 10.1002/adfm.201505070.

[67] F. Khatyr, C. Imberdis, P. Vescovo, D. Varchon, and J.-M. Lagarde, “Model of the viscoelastic behaviour of skin in vivo and study of anisotropy,” *Skin Res. Technol.*, vol. 10, no. 2, pp. 96–103, 2004, doi: 10.1111/j.1600-0846.2004.00057.x.

[68] M. O. F. Emon and J.-W. Choi, “Flexible Piezoresistive Sensors Embedded in 3D Printed Tires,” *Sensors*, vol. 17, no. 3, p. 656, Mar. 2017, doi: 10.3390/s17030656.

[69] Y.-S. Hong, “Smart Care Beds for Elderly Patients with Impaired Mobility,” *Wireless Communications and Mobile Computing*, 2018. https://www.hindawi.com/journals/wcmc/2018/1780904/abs/ (accessed Mar. 31, 2019).

[70] D. Hera, A. Berndt, T. Günther, S. Schmiel, C. Harendt, and A. Zimmermann, "Flexible Packaging by Film-Assisted Molding for Microintegration of Inertia Sensors," *Sensors*, vol. 17, no. 7, p. 1511, Jul. 2017, doi: 10.3390/s17071511.

[71] I. Teyeb, O. Jemai, M. Zaied, and C. B. Amar, "Towards a Smart Car Seat Design for Drowsiness Detection Based on Pressure Distribution of the Driver's Body," *ICSEA 2016*, p. 230, 2016.

[72] M. K. Yapici and T. E. Alkhidir, "Intelligent Medical Garments with Graphene-Functionalized Smart-Cloth ECG Sensors," *Sensors*, vol. 17, no. 4, p. 875, Apr. 2017, doi: 10.3390/s17040875.

[73] C.-L. Choong *et al.*, "Highly Stretchable Resistive Pressure Sensors Using a Conductive Elastomeric Composite on a Micropyramid Array," *Adv. Mater.*, vol. 26, no. 21, pp. 3451–3458, 2014, doi: 10.1002/adma.201305182.

[74] L. Pan *et al.*, "An ultra-sensitive resistive pressure sensor based on hollow-sphere microstructure induced elasticity in conducting polymer film," *Nat. Commun.*, vol. 5, no. 1, pp. 1–8, Jan. 2014, doi: 10.1038/ncomms4002.

[75] S.-J. Woo, J.-H. Kong, D.-G. Kim, and J.-M. Kim, "A thin all-elastomeric capacitive pressure sensor array based on micro-contact printed elastic conductors," *J. Mater. Chem. C*, vol. 2, no. 22, pp. 4415–4422, 2014, doi: 10.1039/C4TC00392F.

[76] W. Choi, J. Lee, Y. Kyoung Yoo, S. Kang, J. Kim, and J. Hoon Lee, "Enhanced sensitivity of piezoelectric pressure sensor with microstructured polydimethylsiloxane layer," *Appl. Phys. Lett.*, vol. 104, no. 12, p. 123701, Mar. 2014, doi: 10.1063/1.4869816.

[77] Zhenglong Sun, M. Balicki, Jin Kang, J. Handa, R. Taylor, and I. Iordachita, "Development and preliminary data of novel integrated optical micro-force sensing tools for retinal microsurgery," in *2009 IEEE International Conference on Robotics and Automation*, 2009, pp. 1897–1902, doi: 10.1109/ROBOT.2009.5152836.

[78] Y. Hasegawa, H. Sasaki, M. Shikida, K. Sato, and K. Itoigawa, "Magnetic actuation of a micro-diaphragm structure for an active tactile sensor," in *Micro-Nanomechatronics and Human Science, 2004 and The Fourth Symposium Micro-Nanomechatronics for Information-Based Society, 2004.*, 2004, pp. 99–104, doi: 10.1109/MHS.2004.1421284.

[79] L. Zou, C. Ge, Z. J. Wang, E. Cretu, and X. Li, "Novel Tactile Sensor Technology and Smart Tactile Sensing Systems: A Review," *Sensors*, vol. 17, no. 11, p. 2653, Nov. 2017, doi: 10.3390/s17112653.

[80] H. Ohno and K. Ito, "Room-Temperature Molten Salt Polymers as a Matrix for Fast Ion Conduction," *Chem. Lett.*, vol. 27, no. 8, pp. 751–752, Aug. 1998, doi: 10.1246/cl.1998.751.

[81] A. Noda and M. Watanabe, “Highly conductive polymer electrolytes prepared by in situ polymerization of vinyl monomers in room temperature molten salts,” *Electrochimica Acta*, vol. 45, no. 8, pp. 1265–1270, Jan. 2000, doi: 10.1016/S0013-4686(99)00330-8.

[82] J. Lu, F. Yan, and J. Texter, “Advanced applications of ionic liquids in polymer science,” *Prog. Polym. Sci.*, vol. 34, no. 5, pp. 431–448, May 2009, doi: 10.1016/j.progpolymsci.2008.12.001.

[83] J. Lee, M. J. Panzer, Y. He, T. P. Lodge, and C. D. Frisbie, “Ion Gel Gated Polymer Thin-Film Transistors,” *J. Am. Chem. Soc.*, vol. 129, no. 15, pp. 4532–4533, Apr. 2007, doi: 10.1021/ja070875e.

[84] S. Washiro, M. Yoshizawa, H. Nakajima, and H. Ohno, “Highly ion conductive flexible films composed of network polymers based on polymerizable ionic liquids,” *Polymer*, vol. 45, no. 5, pp. 1577–1582, Mar. 2004, doi: 10.1016/j.polymer.2004.01.003.

[85] C.-Y. Wu, W.-H. Liao, and Y.-C. Tung, “Integrated ionic liquid-based electrofluidic circuits for pressure sensing within polydimethylsiloxane microfluidic systems,” *Lab. Chip*, vol. 11, no. 10, pp. 1740–1746, May 2011, doi: 10.1039/C0LC00620C.

[86] S. H. Cho *et al.*, “Micropatterned Pyramidal Ionic Gels for Sensing Broad-Range Pressures with High Sensitivity,” *ACS Appl. Mater. Interfaces*, vol. 9, no. 11, pp. 10128–10135, Mar. 2017, doi: 10.1021/acsami.7b00398.

[87] O. Kim, S. Y. Kim, B. Park, W. Hwang, and M. J. Park, “Factors Affecting Electromechanical Properties of Ionic Polymer Actuators Based on Ionic Liquid-Containing Sulfonated Block Copolymers,” *Macromolecules*, vol. 47, no. 13, pp. 4357–4368, Jul. 2014, doi: 10.1021/ma500869h.

[88] C. Feng *et al.*, “Electroresponsive Ionic Liquid Crystal Elastomers,” *Macromol. Rapid Commun.*, vol. 40, no. 19, p. 1900299, 2019, doi: 10.1002/marc.201900299.

[89] R. Ramasubramaniam, J. Chen, and H. Liu, “Homogeneous carbon nanotube/polymer composites for electrical applications,” *Appl. Phys. Lett.*, vol. 83, no. 14, pp. 2928–2930, Sep. 2003, doi: 10.1063/1.1616976.

[90] H. Peng, “Aligned Carbon Nanotube/Polymer Composite Films with Robust Flexibility, High Transparency, and Excellent Conductivity,” *J. Am. Chem. Soc.*, vol. 130, no. 1, pp. 42–43, Jan. 2008, doi: 10.1021/ja078267m.

[91] J. Wang, J. Dai, and T. Yarlagadda, “Carbon Nanotube−Conducting-Polymer Composite Nanowires,” *Langmuir*, vol. 21, no. 1, pp. 9–12, Jan. 2005, doi: 10.1021/la0475977.

[92] Y. Zeng, P. Liu, J. Du, L. Zhao, P. M. Ajayan, and H.-M. Cheng, “Increasing the electrical conductivity of carbon nanotube/polymer composites by using weak nanotube–polymer interactions,” *Carbon*, vol. 48, no. 12, pp. 3551–3558, Oct. 2010, doi: 10.1016/j.carbon.2010.05.053.

[93] M. S. Han *et al.*, “Effect of multi-walled carbon nanotube dispersion on the electrical, morphological and rheological properties of polycarbonate/multi-walled carbon nanotube composites,” *Macromol. Res.*, vol. 17, no. 11, pp. 863–869, Nov. 2009, doi: 10.1007/BF03218627.

[94] X. Xu and Z. Wang, “Non-covalent dispersed carbon nanotube–benzocyclobutene composites as a bonding interface material for three-dimensional integration,” *Microelectron. Eng.*, vol. 91, pp. 33–38, Mar. 2012, doi: 10.1016/j.mee.2011.10.010.

[95] F. Xin and L. Li, “Effect of Triton X-100 on MWCNT/PP composites,” *J. Thermoplast. Compos. Mater.*, vol. 26, no. 2, pp. 227–242, Mar. 2013, doi: 10.1177/0892705711429982.

[96] Y. Geng, M. Y. Liu, J. Li, X. M. Shi, and J. K. Kim, “Effects of surfactant treatment on mechanical and electrical properties of CNT/epoxy nanocomposites,” *Compos. Part Appl. Sci. Manuf.*, vol. 39, no. 12, pp. 1876–1883, Dec. 2008, doi: 10.1016/j.compositesa.2008.09.009.

[97] T. Akasaka, F. Wudl, and S. Nagase, *Chemistry of Nanocarbons*. John Wiley & Sons, 2010.

[98] H. T. Ham, Y. S. Choi, and I. J. Chung, “An explanation of dispersion states of single-walled carbon nanotubes in solvents and aqueous surfactant solutions using solubility parameters,” *J. Colloid Interface Sci.*, vol. 286, no. 1, pp. 216–223, Jun. 2005, doi: 10.1016/j.jcis.2005.01.002.

[99] V. Mittal, *Polymer Nanotubes Nanocomposites: Synthesis, Properties and Applications*. John Wiley & Sons, 2014.

[100] P.-C. Ma, N. A. Siddiqui, G. Marom, and J.-K. Kim, “Dispersion and functionalization of carbon nanotubes for polymer-based nanocomposites: A review,” *Compos. Part Appl. Sci. Manuf.*, vol. 41, no. 10, pp. 1345–1367, Oct. 2010, doi: 10.1016/j.compositesa.2010.07.003.

[101] N. Grossiord *et al.*, “High-Conductivity Polymer Nanocomposites Obtained by Tailoring the Characteristics of Carbon Nanotube Fillers,” *Adv. Funct. Mater.*, vol. 18, no. 20, pp. 3226–3234, 2008, doi: 10.1002/adfm.200800528.

[102] N. Grossiord, J. Loos, O. Regev, and C. E. Koning, “Toolbox for Dispersing Carbon Nanotubes into Polymers To Get Conductive Nanocomposites,” *Chem. Mater.*, vol. 18, no. 5, pp. 1089–1099, Mar. 2006, doi: 10.1021/cm051881h.

[103] I. E. Pacios, M. J. Molina, M. R. Gómez-Antón, and I. F. Piérola, “Correlation of swelling and crosslinking density with the composition of the reacting mixture employed in radical crosslinking copolymerization,” *J. Appl. Polym. Sci.*, vol. 103, no. 1, pp. 263–269, 2007, doi: 10.1002/app.25269.

[104] Ch. Hirschl *et al.*, “Determining the degree of crosslinking of ethylene vinyl acetate photovoltaic module encapsulants—A comparative study,” *Sol. Energy Mater. Sol. Cells*, vol. 116, pp. 203–218, Sep. 2013, doi: 10.1016/j.solmat.2013.04.022.

[105] H. Inomata, N. Wada, Y. Yagi, S. Goto, and S. Saito, “Swelling behaviours of N-alkylacrylamide gels in water: effects of copolymerization and crosslinking density,” *Polymer*, vol. 36, no. 4, pp. 875–877, Jan. 1995, doi: 10.1016/0032-3861(95)93120-B.

[106] J. Lee, M. O. F. Emon, M. Vatani, and J.-W. Choi, “Effect of degree of crosslinking and polymerization of 3D printable polymer/ionic liquid composites on performance of stretchable piezoresistive sensors,” *Smart Mater. Struct.*, vol. 26, no. 3, p. 035043, Feb. 2017, doi: 10.1088/1361-665X/aa5c70.

[107] T. a. C. Flipsen, R. Derks, H. van der Vegt, R. Stenekes, A. J. Pennings, and G. Hadziioannou, “Densely crosslinked polycarbosiloxanes. II: Thermal and mechanical properties,” *J. Polym. Sci. Part B Polym. Phys.*, vol. 35, no. 9, pp. 1311–1331, 1997, doi: 10.1002/(SICI)1099-0488(19970715)35:9<1311::AID-POLB2>3.0.CO;2-P.

[108] C. Mattmann, F. Clemens, and G. Tröster, “Sensor for Measuring Strain in Textile,” *Sensors*, vol. 8, no. 6, pp. 3719–3732, Jun. 2008, doi: 10.3390/s8063719.

[109] X. Xiao *et al.*, “High-Strain Sensors Based on ZnO Nanowire/Polystyrene Hybridized Flexible Films,” *Adv. Mater.*, vol. 23, no. 45, pp. 5440–5444, 2011, doi: 10.1002/adma.201103406.

[110] R. H. Colby, L. J. Fetters, and W. W. Graessley, “The melt viscosity-molecular weight relationship for linear polymers,” *Macromolecules*, vol. 20, no. 9, pp. 2226–2237, Sep. 1987, doi: 10.1021/ma00175a030.

[111] H. E. H. Meijer and L. E. Govaert, “Mechanical performance of polymer systems: The relation between structure and properties,” *Prog. Polym. Sci.*, vol. 30, no. 8, pp. 915–938, Aug. 2005, doi: 10.1016/j.progpolymsci.2005.06.009.

[112] L.-P. Blanchard, J. Hesse, and S. L. Malhotra, “Effect of Molecular Weight on Glass Transition by Differential Scanning Calorimetry,” *Can. J. Chem.*, vol. 52, no. 18, pp. 3170–3175, Sep. 1974, doi: 10.1139/v74-465.

[113] R. W. Nunes, J. R. Martin, and J. F. Johnson, “Influence of molecular weight and molecular weight distribution on mechanical properties of polymers,” *Polym. Eng. Sci.*, vol. 22, no. 4, pp. 205–228, 1982, doi: 10.1002/pen.760220402.

[114] J. T. Seitz, “The estimation of mechanical properties of polymers from molecular structure,” *J. Appl. Polym. Sci.*, vol. 49, no. 8, pp. 1331–1351, 1993, doi: 10.1002/app.1993.070490802.

[115] A. Maffezzoli, A. Trivisano, M. Opalicki, J. Mijovic, and J. M. Kenny, “Correlation between dielectric and chemorheological properties during cure of epoxy-based composites,” *J. Mater. Sci.*, vol. 29, no. 3, pp. 800–808, Feb. 1994, doi: 10.1007/BF00445996.

[116] H. Song *et al.*, “Superfast and high-sensitivity printable strain sensors with bioinspired micron-scale cracks,” *Nanoscale*, vol. 9, no. 3, pp. 1166–1173, Jan. 2017, doi: 10.1039/C6NR07333F.

[117] Y. Song *et al.*, “Highly Compressible Integrated Supercapacitor–Piezoresistance-Sensor System with CNT–PDMS Sponge for Health Monitoring,” *Small*, vol. 13, no. 39, p. 1702091, 2017, doi: 10.1002/smll.201702091.

[118] K. Lee *et al.*, “Nickel Nanofoam/Different Phases of Ordered Mesoporous Carbon Composite Electrodes for Superior Capacitive Energy Storage,” *ACS Appl. Mater. Interfaces*, vol. 8, no. 34, pp. 22516–22525, Aug. 2016, doi: 10.1021/acsami.6b06611.

[119] D. Mecerreyes, “Polymeric ionic liquids: Broadening the properties and applications of polyelectrolytes,” *Prog. Polym. Sci.*, vol. 36, no. 12, pp. 1629–1648, Dec. 2011, doi: 10.1016/j.progpolymsci.2011.05.007.

[120] T. Ueki and M. Watanabe, “Macromolecules in Ionic Liquids: Progress, Challenges, and Opportunities,” *Macromolecules*, vol. 41, no. 11, pp. 3739–3749, Jun. 2008, doi: 10.1021/ma800171k.

[121] Md. A. B. H. Susan, T. Kaneko, A. Noda, and M. Watanabe, “Ion Gels Prepared by in Situ Radical Polymerization of Vinyl Monomers in an Ionic Liquid and Their Characterization as Polymer Electrolytes,” *J. Am. Chem. Soc.*, vol. 127, no. 13, pp. 4976–4983, Apr. 2005, doi: 10.1021/ja045155b.

[122] J. Vila, L. M. Varela, and O. Cabeza, “Cation and anion sizes influence in the temperature dependence of the electrical conductivity in nine imidazolium based ionic liquids,” *Electrochimica Acta*, vol. 52, no. 26, pp. 7413–7417, Sep. 2007, doi: 10.1016/j.electacta.2007.06.044.

[123] R. J. D. Tilley, *Understanding Solids: The Science of Materials*. John Wiley & Sons, 2004.

[124] M. Vaezi, S. Chianrabutra, B. Mellor, and S. Yang, “Multiple material additive manufacturing – Part 1: a review,” *Virtual Phys. Prototyp.*, vol. 8, no. 1, pp. 19–50, Mar. 2013, doi: 10.1080/17452759.2013.778175.

[125] Z. Weng, J. Wang, T. Senthil, and L. Wu, “Mechanical and thermal properties of ABS/montmorillonite nanocomposites for fused deposition modeling 3D printing,” *Mater. Des.*, vol. 102, pp. 276–283, Jul. 2016, doi: 10.1016/j.matdes.2016.04.045.

[126] J. Lee, Y. Lu, S. Kashyap, A. Alarmdari, Md. O. F. Emon, and J.-W. Choi, “Liquid bridge microstereolithography,” *Addit. Manuf.*, vol. 21, pp. 76–83, May 2018, doi: 10.1016/j.addma.2018.02.012.

[127] S. Meteyer, X. Xu, N. Perry, and Y. F. Zhao, “Energy and Material Flow Analysis of Binder-jetting Additive Manufacturing Processes,” *Procedia CIRP*, vol. 15, pp. 19–25, Jan. 2014, doi: 10.1016/j.procir.2014.06.030.

[128] S. F. S. Shirazi *et al.*, “A review on powder-based additive manufacturing for tissue engineering: selective laser sintering and inkjet 3D printing,” *Sci. Technol. Adv. Mater.*, vol. 16, no. 3, p. 033502, Jun. 2015, doi: 10.1088/1468-6996/16/3/033502.

[129] T. A. Campbell and O. S. Ivanova, “3D printing of multifunctional nanocomposites,” *Nano Today*, vol. 8, no. 2, pp. 119–120, Apr. 2013, doi: 10.1016/j.nantod.2012.12.002.

[130] M. Vatani, E. D. Engeberg, and J.-W. Choi, “Conformal direct-print of piezoresistive polymer/nanocomposites for compliant multi-layer tactile sensors,” *Addit. Manuf.*, vol. 7, pp. 73–82, Jul. 2015, doi: 10.1016/j.addma.2014.12.009.

[131] X. Wang, M. Jiang, Z. Zhou, J. Gou, and D. Hui, “3D printing of polymer matrix composites: A review and prospective,” *Compos. Part B Eng.*, vol. 110, pp. 442–458, Feb. 2017, doi: 10.1016/j.compositesb.2016.11.034.

[132] M. O. F. Emon, F. Alkadi, D. G. Philip, D.-H. Kim, K.-C. Lee, and J.-W. Choi, “Multi-material 3D printing of a soft pressure sensor,” *Addit. Manuf.*, vol. 28, pp. 629–638, Aug. 2019, doi: 10.1016/j.addma.2019.06.001.

[133] V. Slesarenko and S. Rudykh, “Towards mechanical characterization of soft digital materials for multimaterial 3D-printing,” *Int. J. Eng. Sci.*, vol. 123, pp. 62–72, Feb. 2018, doi: 10.1016/j.ijengsci.2017.11.011.

[134] J. J. Adams *et al.*, “Conformal Printing of Electrically Small Antennas on Three-Dimensional Surfaces,” *Adv. Mater.*, vol. 23, no. 11, pp. 1335–1340, 2011, doi: 10.1002/adma.201003734.

[135] K. Sim *et al.*, “Three-dimensional curvy electronics created using conformal additive stamp printing,” *Nat. Electron.*, vol. 2, no. 10, pp. 471–479, Oct. 2019, doi: 10.1038/s41928-019-0304-4.

[136] Y. Jin, J. Du, Y. He, and G. Fu, “Modeling and process planning for curved layer fused deposition,” *Int. J. Adv. Manuf. Technol.*, vol. 91, no. 1, pp. 273–285, Jul. 2017, doi: 10.1007/s00170-016-9743-5.

[137] F. Alkadi, K.-C. Lee, A. H. Bashiri, and J.-W. Choi, “Conformal additive manufacturing using a direct-print process,” *Addit. Manuf.*, vol. 32, p. 100975, Mar. 2020, doi: 10.1016/j.addma.2019.100975.

[138] J. D. Ferry, *Viscoelastic Properties of Polymers*. John Wiley & Sons, 1980.

[139] W. Wu, P. Geng, G. Li, D. Zhao, H. Zhang, and J. Zhao, “Influence of Layer Thickness and Raster Angle on the Mechanical Properties of 3D-Printed PEEK and a Comparative Mechanical Study between PEEK and ABS,” *Materials*, vol. 8, no. 9, pp. 5834–5846, Sep. 2015, doi: 10.3390/ma8095271.

[140] N. W. Tschoegl, “Time Dependence in Material Properties: An Overview,” *Mech. Time-Depend. Mater.*, vol. 1, no. 1, pp. 3–31, Mar. 1997, doi: 10.1023/A:1009748023394.

[141] L. Qiu *et al.*, “Ultrafast Dynamic Piezoresistive Response of Graphene-Based Cellular Elastomers,” *Adv. Mater.*, vol. 28, no. 1, pp. 194–200, 2016, doi: 10.1002/adma.201503957.

[142] J. H. Low, P. S. Chee, E. H. Lim, and V. Ganesan, “Design of a Wireless Smart Insole using Stretchable Microfluidic Sensor for Gait Monitoring,” *Smart Mater. Struct.*, 2020, doi: 10.1088/1361-665X/ab802c.

[143] W. V. Rosenberg, T. Chanwimalueang, V. Goverdovsky, D. Looney, D. Sharp, and D. P. Mandic, “Smart Helmet: Wearable Multichannel ECG and EEG,” *IEEE J. Transl. Eng. Health Med.*, vol. 4, pp. 1–11, 2016, doi: 10.1109/JTEHM.2016.2609927.

[144] G. Said, “Diabetic neuropathy—a review,” *Nat. Clin. Pract. Neurol.*, vol. 3, no. 6, pp. 331–340, Jun. 2007, doi: 10.1038/ncpneuro0504.

[145] P. K. Thomas, “Classification, Differential Diagnosis, and Staging of Diabetic Peripheral Neuropathy,” *Diabetes*, vol. 46, no. Supplement 2, pp. S54–S57, Sep. 1997, doi: 10.2337/diab.46.2.S54.

[146] J. Cao, C. Piedrahita, and T. Kyu, “Mechanoelectrical Conversion in Highly Ionic Conductive Solid-State Polymer Electrolyte Membranes,” *Macromol. Mater. Eng.*, vol. 304, no. 5, p. 1800777, 2019, doi: 10.1002/mame.201800777.